

PREPARATION AND PROPERTIES OF MIXED METAL SULFIDE THIN FILMS FOR PHOTODIODE APPLICATIONS

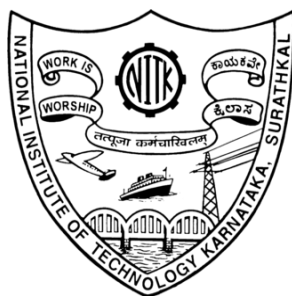
Thesis

Submitted in partial fulfilment of the requirements for the degree of

DOCTOR OF PHILOSOPHY

by

BISWAJIT BARMAN



DEPARTMENT OF PHYSICS

NATIONAL INSTITUTE OF TECHNOLOGY KARNATAKA,

SURATHKAL, MANGALORE – 575025

MARCH, 2019

DECLARATION

I hereby *declare* that the Research Thesis entitled "**Preparation and properties of mixed metal sulfide thin films for photosensor applications**" Which is being submitted to the National Institute of Technology Karnataka, Surathkal in partial fulfilment of the requirements for the award of the Degree of Doctor of Philosophy in **Physics** is a *bonafide report of the research work carried out by me*. The material contained in this Research Thesis has not been submitted to any University or Institution for the award of any degree.

Biswajit Barman

Reg. No.: 165056PH16F02

Department of Physics

Place: NITK-Surathkal

Date: 16/03/2020

C E R T I F I C A T E

This is to *certify* that the Research Thesis **Preparation and properties of mixed metal sulfide thin films for photosensor applications** submitted by **Mr. Biswajit Barman** (Register Number: **165056PH16F02**) as the record of the research work carried out by him, is *accepted as the Research Thesis submission* in partial fulfilment of the requirements for the award of degree of Doctor of Philosophy.

Research Guide(s)

Prof. Kasturi V. Bangera

Chairman - DRPC

ACKNOWLEDGMENT

While a Ph.D. is meant to represent that an individual has made a unique contribution to science, it would be disingenuous to suggest that it is something that can be done by an individual alone. Over the course of three and a half years, I have faced many challenges, both scientific and personal, and would not have been able to reach this point without the help and guidance of many others.

First and foremost, I would like to express my sincere gratitude to my supervisor Prof. (Mrs.) Kasturi V. Bangera for considering me as her research student. Her constant guidance, cooperation, and moral support have always kept me going ahead. The research work presented here would have been impossible without the support and guidance of my supervisor.

I would like to express my heartfelt gratitude to Prof. G. K. Shivakumar for his valuable suggestions and advice towards my research work.

Besides my supervisor, I would also like to thank the RPAC members – Prof. M.N. Satyanarayan and Prof. Vidya Shetty. K, for their insightful comments and encouragement.

I have been extremely fortunate to work with some exceptionally talented people during my time as a doctoral student, without whom this thesis would not be possible. First, thank you Dr. Santhosh T.C.M. for sharing your knowledge about the thermal evaporation system and the valuable suggestions on ternary alloys.

Thank you Mr. Bharath S.P. for all of your help in characterizing the materials and it has been a privilege to work with you.

I would also like to thank my TFL colleagues, Miss Subhasmita, Dr. Sowjanya V., and Dr. Veena E. for all the valuable suggestions and discussions. Miss Subhasmita – thank you for handling the workload assigned to me. I'm quite sure I wouldn't be writing this without your help.

A big thank you to my large, loving family, who have all played a part in my education. A few special thanks to Mom, Dad, and Brother for your unending support and always believing in me.

Thank you, friends: Dr. Rajesh K., Mr. Hemanth K., Mr. Mahendra K., Mr. Pramod K., Dr. Alok K., Mr. Pandu N., and Ms. Riya M. for always supporting me in various circumstances.

There are many persons to whom I would like to express my gratitude. Although I might have failed to mention their names here, their help will never be forgotten.

Funding sources: This research work is funded by the “Ministry of Human Resource Development (MHRD), India”. I am thankful to NITK for providing Institute Fellowship. I am also obliged to “DST-PURSE, Mangalore University, and Central Instrumentation Facility, Manipal Institute of Technology” for providing SEM-EDAX and UV-Vis-NIR Spectrophotometer facility, respectively.

Biswajit Barman

ABSTRACT

The present work reported in this thesis involves studies on binary metal sulfides namely ZnS, CdS, and SnS along with the investigations on the ternary compounds: $\text{Cu}_x(\text{ZnS})_{1-x}$, $\text{Zn}_x\text{Cd}_{1-x}\text{S}$, and $\text{Zn}_x\text{Sn}_{1-x}\text{S}$ thin films deposited using a vacuum thermal evaporation method on glass substrates. The above compounds were selected due to their optimal direct band gap energy values. Substrate temperature plays an essential role in controlling the crystallite size, structural phase, surface morphology, and optoelectrical properties of the films. By varying the substrate temperature, the binary films were optimized to form a stoichiometric film and the various properties of the films were analyzed as a function of substrate temperature. All the films were found to be free from any pinholes and cracks. The band gap energy for the stoichiometric ZnS, CdS, and SnS thin films was found to be 3.49 eV, 2.42 eV, and 1.54 eV, respectively. Both CdS and SnS films displayed exceptional photodetector properties and the photosensitivity was found to be highest at 10.93 for the stoichiometric SnS films. The $\text{Cu}_x(\text{ZnS})_{1-x}$ films exhibited outstanding p-type conductivity with very high transparency and thereby, suggesting that the films can be used as a p-type transparent conducting layer. The various properties of the $\text{Zn}_x\text{Cd}_{1-x}\text{S}$ and $\text{Zn}_x\text{Sn}_{1-x}\text{S}$ thin films were tuned by altering the composition of the films. A successful band gap engineering was achieved for the ternary compound thin films. The $\text{Zn}_x\text{Cd}_{1-x}\text{S}$ and $\text{Zn}_x\text{Sn}_{1-x}\text{S}$ films were analyzed for photodetector application and the various parameters such as photoconductivity (σ_L), photosensitivity (S), photoresponsivity (R), recovery time (τ_d), and response time (τ_r) of the films were calculated. The present study reveals a maximum photosensitivity of 43.38 for the $\text{Zn}_{0.10}\text{Sn}_{0.90}\text{S}$ thin films.

Keywords: Vacuum thermal evaporation; metal sulfides; ternary compounds; band gap engineering; photodetector.

Table of Content

Chapter 1	Introduction	Page No.
1.1	Thin film technology.....	1
1.2	Compound semiconductors.....	2
1.3	Photodetector.....	4
1.4	Literature survey.....	5
1.5	Scope of the work.....	12
1.6	Objectives.....	13
1.7	Thesis outline.....	13
Chapter 2	Thin Film: deposition and characterizations	
2.1	Cleaning of the substrates.....	15
2.2	Thermal evaporation method.....	15
2.3	Characterization techniques.....	16
2.3.1	Thickness measurement method.....	16
2.3.2	X-ray diffraction (XRD).....	17
2.3.3	Scanning electron microscope (SEM).....	18
2.3.4	Energy dispersive analysis of X-rays (EDAX).....	20
2.3.5	UV-Vis-NIR spectroscopy.....	20
2.3.6	Raman spectroscopy.....	21
2.3.7	Opto-electrical analysis.....	21
Chapter 3	Studies on binary sulfide thin films	
3.1	Zinc sulfide (ZnS) thin films.....	25
3.1.1	Experimental details.....	25
3.1.2	XRD analysis.....	25
3.1.3	Morphological and compositional analysis.....	26
3.1.4	Optical studies.....	29
3.2	Cadmium sulfide (CdS) thin films.....	29
3.2.1	Experimental details.....	30
3.2.2	Structural studies.....	30

	3.2.3	Morphological studies.....	31
	3.2.4	Optical studies.....	34
	3.2.5	Opto-electrical properties.....	35
3.3		Tin sulfide (SnS) thin films.....	36
	3.3.1	Experimental details.....	37
	3.3.2	Structural studies.....	37
	3.3.3	Raman studies.....	39
	3.3.4	Morphological and compositional analysis.....	40
	3.3.5	Optical studies.....	41
	3.3.6	Opto-electrical properties.....	42
Chapter 4		Investigations on ternary sulfide thin films	
4.1		$\text{Cu}_x(\text{ZnS})_{1-x}$ thin films.....	47
	4.1.1	Experimental details.....	47
	4.1.2	Structural studies.....	48
	4.1.3	Morphological studies.....	49
	4.1.4	Optical properties.....	51
	4.1.5	Electrical properties.....	52
4.2		$\text{Zn}_x\text{Cd}_{1-x}\text{S}$ thin films.....	54
	4.2.1	Experimental details.....	54
	4.2.2	Structural studies.....	54
	4.2.3	Surface morphological & compositional studies...	57
	4.2.4	Opto-electrical studies.....	58
4.3		$\text{Zn}_x\text{Sn}_{1-x}\text{S}$ thin films.....	65
	4.3.1	Experimental details.....	65
	4.3.2	Structural analysis.....	66
	4.3.3	Morphological analysis.....	67
	4.3.4	Opto-electrical studies.....	69
Chapter 5		Summary and conclusions	
5.1		Summary of the present work.....	75
5.2		Conclusions.....	75
	5.2.1	Binary metal sulfides.....	75

5.2.2	Ternary metal sulfides.....	76
5.3	Scope for future work.....	77

References

Publications

Curriculum Vitae

List of Figures

Figure No.	Details	Page No.
1.1	Classification of semiconductors.....	2
1.2	Internal photoelectric effect (i) intrinsic photoconductivity, (ii) n-type extrinsic photoconductivity, and (iii) p-type extrinsic photoconductivity.....	5
2.1	Schematic of thermal evaporation technique.....	16
2.2	A typical sketch of a Scanning Electron Microscope.....	19
3.1	XRD image of ZnS thin films deposited at a) 297K, b) 373K, and c) 423K.....	26
3.2	XRD image of annealed ZnS thin films deposited at a) 297K, b) 373K, and c) 423K.....	26
3.3	SEM images of as-deposited ZnS thin film at a substrate temperature of a) 297K, b) 373K, c) 423K and post- annealed ZnS film deposited at d) 297K, e) 373K, f) 423K.....	27
3.4	EDAX spectra of stoichiometric ZnS thin film.....	28
3.5	Elemental mapping of stoichiometric ZnS thin n film (a) Zn and (b) S elements.....	28
3.6	Transmission spectra of stoichiometric ZnS thin film.....	29
3.7	Tauc's Plot of stoichiometric ZnS thin film.....	29
3.8	XRD images of CdS thin films deposited at a) 297K, b) 323K, c) 373K, and d) 423K.....	31
3.9	Variation of crystallite size and intensity of (002) peak with substrate temperature.....	33
3.10	FE-SEM pictures of CdS thin films deposited at a) 297K, b) 323K, c) 373K, and d) 423K.....	33
3.11	EDAX plots of CdS thin films deposited at a) 297K, b) 323K, c) 373K, and d) 423K.....	34

3.12	Transmittance plot of CdS thin films deposited at a) 297K, b) 323K, c) 373K, and d) 423K.....	34
3.13	Tauc's plot of CdS thin films deposited at a) 297K, b) 323K, c) 373K, and d) 423K.....	34
3.14	IV plots of CdS thin films deposited at a) 297K, b) 323K, c) 373K, and d) 423K.....	35
3.15	Photocurrent vs Intensity plot of CdS thin films a) 297K, b) 323K, c) 373K, and d) 423K.....	36
3.16	XRD diffractograms of SnS thin films deposited at a substrate temperature of a) 297 K, b) 323 K, c) 373 K, and d) 423 K.....	38
3.17	Raman spectra of SnS thin films deposited at a substrate temperature of a) 297 K, b) 323 K, c) 373 K, and d) 423 K.....	39
3.18	EDAX spectra of SnS thin films deposited at a substrate temperature of a) 297 K, b) 323 K, c) 373 K, and d) 423 K.....	39
3.19	FE-SEM images of SnS thin films deposited at a substrate temperature of a) 297 K, b) 323 K, c) 373 K, and d) 423 K.....	41
3.20	Transmittance spectra of SnS thin films deposited at a) 297 K, b) 323 K, c) 373 K, and d) 423 K.....	41
3.21	Plot of α Vs $h\nu$ of SnS thin films deposited at a) 297 K, b) 323 K, c) 373 K, and d) 423 K.....	41
3.22	Tauc's plot of SnS thin films deposited at a) 297 K, b) 323 K, c) 373 K, and d) 423 K.....	43
3.23	Current Vs Voltage plot of SnS thin films deposited at a) 297 K, b) 323 K, c) 373 K, and d) 323 K.....	43
3.24	Variation of $\ln R$ with $1000/T$ of SnS thin films deposited at a) 297 K, b) 323 K, c) 373 K, and d) 423 K.....	44

3.25	Response and recovery time of SnS thin films deposited at a substrate temperature of 323 K.....	45
3.26	Photoconductivity Vs Time response of SnS thin films deposited at a substrate temperature of a) 297 K, b) 323 K, and c) 373 K.....	45
4.1	XRD patterns of $\text{Cu}_x(\text{ZnS})_{1-x}$ thin films: a) $x = 0.01$, b) $x = 0.02$, c) $x = 0.03$, d) $x = 0.05$, e) $x = 0.10$ and f) $x = 0.25$	48
4.2	FE-SEM images of $\text{Cu}_x(\text{ZnS})_{1-x}$ thin films of various Cu concentration: a) $x = 0.01$, b) $x = 0.02$, c) $x = 0.03$, d) $x = 0.05$, e) $x = 0.10$ and f) $x = 0.25$	50
4.3	EDAX analysis of $\text{Cu}_{0.03}(\text{ZnS})_{0.70}$ thin films (a) EDAX Spectra; Elemental mapping of (b) Cu, (c) Zn and (d) S...	51
4.4	Transmittance vs wavelength plot of $\text{Cu}_x(\text{ZnS})_{1-x}$ thin films: a) $x = 0$, b) $x = 0.01$, c) $x = 0.02$, and d) $x = 0.03$	52
4.5	Tauc's plot of $\text{Cu}_x(\text{ZnS})_{1-x}$ thin films : $x =$ a) 0, b) 0.01, c) 0.02, d) 0.03, e) 0.05, f) 0.10, and g) 0.25.....	52
4.6	IV characteristics of $\text{Cu}_x(\text{ZnS})_{1-x}$ thin films : $x =$ a) 0, b) 0.01, c) 0.02, d) 0.03, e) 0.05, f) 0.10, and g) 0.25.....	53
4.7	Conductivity vs $1000/T$ plot of $\text{Cu}_x(\text{ZnS})_{1-x}$ thin films: $x =$ a) 0, b) 0.01, c) 0.02, d) 0.03, e) 0.05, f) 0.10, and g) 0.25.	53
4.8	XRD spectra of $\text{Zn}_{0.45}\text{Cd}_{0.55}\text{S}$ thin film without annealing treatment.....	55
4.9	XRD diffractograms of $\text{Zn}_x\text{Cd}_{1-x}\text{S}$ thin films with $x =$ a) 0, b) 0.15, c) 0.30, d) 0.45, e) 0.70, f) 0.85, and g) 1.....	56
4.10	Shift in the (002) and (111) peak position of $\text{Zn}_x\text{Cd}_{1-x}\text{S}$ thin films with $x =$ a) 0, b) 0.15, c) 0.30, d) 0.45, e) 0.70, f) 0.85, and g) 1.....	56

4.11	FE-SEM images of $Zn_xCd_{1-x}S$ thin films a) CdS, b) $Zn_{0.15}Cd_{0.85}S$, c) $Zn_{0.30}Cd_{0.70}S$, d) $Zn_{0.45}Cd_{0.55}S$, e) $Zn_{0.70}Cd_{0.30}S$, f) $Zn_{0.85}Cd_{0.15}S$, g) ZnS, and h) cross-sectional view of $Zn_{0.15}Cd_{0.85}S$ films.....	58
4.12	(a) EDAX Spectra of $Zn_{0.15}Cd_{0.85}S$ films; Elemental mapping of (b) Cd, (c) Zn, and (d) S.....	58
4.13	Transmittance spectra of $Zn_xCd_{1-x}S$ thin films with x = a) 0, b) 0.15, c) 0.30, d) 0.45, e) 0.70, f) 0.85, and g) 1.....	59
4.14	Tauc's plot of $Zn_xCd_{1-x}S$ thin films with x = a) 0, b) 0.15, c) 0.30, d) 0.45, e) 0.70, f) 0.85, and g) 1.....	59
4.15	Absorption coefficient spectra of the $Zn_xCd_{1-x}S$ films x = a) 0, b) 0.15, c) 0.30, and d) 0.45.....	60
4.16	Energy band gap (E_g) vs Composition (x) of $Zn_xCd_{1-x}S$ thin films.....	60
4.17	Schematic representation of the $Zn_xCd_{1-x}S$ photodetector device.....	61
4.18	Current Vs Voltage plots of the $Zn_xCd_{1-x}S$ films x = a) 0, b) 0.15, c) 0.30, and d) 0.45.....	61
4.19	$\ln R$ Vs $1000/T$ plot of $Zn_xCd_{1-x}S$ thin films x = a) 0, b) 0.15, c) 0.30, and d) 0.45.....	61
4.20	Photocurrent Vs Intensity plot of the $Zn_xCd_{1-x}S$ films x = a) 0, b) 0.15, c) 0.30, and d) 0.45.....	62
4.21	Photoconductivity response of the $Zn_xCd_{1-x}S$ thin films under light ON/OFF cycles a) x = 1, b) x = 0.15, c) x = 0.30, and d) x = 0.45.....	63
4.22	Photocurrent Vs time plot of $Zn_xCd_{1-x}S$ thin films x = a) 0, b) 0.15, c) 0.30, and d) 0.45.....	64
4.23	XRD diffractograms of $Zn_xSn_{1-x}S$ thin films where x = a) 0, b) 0.10, c) 0.20, d) 0.40, e) 0.70, f) 0.90, and g) 1.....	66

4.24	FE-SEM images of $Zn_xSn_{1-x}S$ thin films: x = a) 0, b) 0.10, c) 0.20, d) 0.40, e) 0.70, f) 0.90, g) 1, and h) EDAX spectra of $Zn_{0.10}Sn_{0.90}S$ thin film.....	67
4.25	Elemental mapping of $Zn_{0.10}Sn_{0.90}S$ thin film (a) Zn, (b) Sn, and (c) S.....	68
4.26	Transmittance spectra of $Zn_xSn_{1-x}S$ thin films a) x = 0, b) x = 0.10, c) x = 0.20, d) x = 0.40, e) x = 0.70, f) x = 0.90, and g) x = 1.....	69
4.27	Tauc's plot of $Zn_xSn_{1-x}S$ thin films a) x = 0, b) x = 0.10, c) x = 0.20, d) x = 0.40, e) x = 0.70, f) x = 0.90, g) x = 1, and h) Variation of band gap with composition 'x'.....	70
4.28	Plot of α Vs $h\nu$ of $Zn_xSn_{1-x}S$ thin films a) x = 0, b) x = 0.10, c) x = 0.20, and d) x = 0.40.....	71
4.29	Schematic representation of Ag/ $Zn_xSn_{1-x}S$ /glass photodetector.....	71
4.30	IV plot of $Zn_xSn_{1-x}S$ films a) x = 0, b) x = 0.10, c) x = 0.20, and d) x = 0.40.....	72
4.31	Ln R Vs $1000/T$ plot of $Zn_xSn_{1-x}S$ thin films a) x = 0, b) x = 0.10, c) x = 0.20, and d) x = 0.40.....	72
4.32	Photoconductivity Vs Time response of $Zn_xSn_{1-x}S$ thin films a) x = 0, b) x = 0.10, c) x = 0.20, and d) x = 0.40.....	72
4.33	Response time and recovery time of $Zn_xSn_{1-x}S$ thin films a) x = 0, b) x = 0.10, c) x = 0.20, and d) x = 0.40.....	73

List of Tables

Table No.	Details	Page No.
1.1	A few crucial parameters of ZnS, CdS and SnS materials.....	3
3.1	Structural parameters of ZnS thin films.....	28
3.2	Elemental composition of ZnS thin films.....	28
3.3	XRD diffraction data of CdS thin films deposited at various conditions.....	32
3.4	Compositional study of CdS thin films.....	32
3.5	Summary of opto-electrical properties of CdS thin films.....	36
3.6	Structural parameters of thermally deposited SnS thin films...	38
3.7	Composition, energy bandgap and activation energies of SnS thin films deposited at various substrate temperatures.....	40
3.8	Photo-response parameters of SnS thin films deposited at a substrate temperature of a) 297 K, b) 323 K, and c) 373 K.....	44
4.1	X-ray diffraction data of $\text{Cu}_x(\text{ZnS})_{1-x}$ thin films.....	49
4.2	Compositional analysis of $\text{Cu}_x(\text{ZnS})_{1-x}$ ($x = 0, 0.01, 0.02, 0.03, 0.05, 0.10$ and 0.25) thin films.....	50
4.3	Summary of electrical and optical properties of $\text{Cu}_x(\text{ZnS})_{1-x}$ thin films.....	53
4.4	XRD diffraction parameters of $\text{Zn}_x\text{Cd}_{1-x}\text{S}$ thin films with $x =$ a) 0, b) 0.15, c) 0.30, d) 0.45, e) 0.70, f) 0.85, and g) 1.....	56
4.5	EDAX analysis & optical band gap of $\text{Zn}_x\text{Cd}_{1-x}\text{S}$ thin films a) CdS, b) $\text{Zn}_{0.15}\text{Cd}_{0.85}\text{S}$, c) $\text{Zn}_{0.30}\text{Cd}_{0.70}\text{S}$, d) $\text{Zn}_{0.45}\text{Cd}_{0.55}\text{S}$, e) $\text{Zn}_{0.70}\text{Cd}_{0.30}\text{S}$, f) $\text{Zn}_{0.85}\text{Cd}_{0.15}\text{S}$ and g) ZnS.....	57
4.6	Opto-electrical parameters of $\text{Zn}_x\text{Cd}_{1-x}\text{S}$ films $x =$ a) 0, b) 0.15, c) 0.30, and d) 0.45.....	65
4.7	Structural constraints of $\text{Zn}_x\text{Sn}_{1-x}\text{S}$ thin films.....	67
4.8	Compositional, optical, and electrical parameters of $\text{Zn}_x\text{Sn}_{1-x}\text{S}$ thin films.....	68

4.9 Photo-response parameters of $Zn_xSn_{1-x}S$ thin films a) $x = 0$,
b) $x = 0.10$, c) $x = 0.20$, and d) $x = 0.40$ 73

NOMENCLATURE

Abbreviations

Ag	Silver
Si	Silicon
GaN	Gallium nitride
Zn	Zinc
Cd	Cadmium
Sn	Tin
S	Sulfur
ZnS	Zinc sulfide
CdS	Cadmium sulfide
SnS	Tin sulfide
Cu	Copper
UV-Vis	Ultra-violet Visible
NIR	Near-infrared
Se	Selenium
CdSe	Cadmium selenide
ZnTe	Zinc telluride
ZnO	Zinc oxide
ZnSe	Zinc selenide
CIGS	Copper indium gallium selenide
CBD	Chemical bath deposition
PVD	Physical vapor deposition
MBE	Molecular beam epitaxy
CZTS	Copper zinc tin sulfide
HAZO	Hydrogen doped aluminum zinc oxide
CdTe	Cadmium telluride
FF	Fill factor
CTO	Cadmium stannate
ZTO	Zinc stannate

TCM	Transparent conducting material
SnO ₂	Tin oxide
Pt	Platinum
Au	Gold
Mo	Molybdenum
HWVD	Hot wall vacuum deposition
RF	Radio frequency
DC	Direct current
ITO	Indium tin oxide
TFT	Thin film transistor
LED	Light emitting diode
OLED	Organic light emitting diode
XRD	X-ray diffraction
FE-SEM	Field emission scanning electron microscope
EDAX	Elemental diffraction of X-rays
IV	Current voltage
n-	n-type
p-	p-type

Symbols & Units

eV	Electron volt
μm	Micrometer
nm	Nanometer
hr	Hour
D	Crystallite size
d	Interplanar distance
a, c	Lattice parameter
2θ	Bragg angle
ρ	Resistivity
σ	Conductivity
σ _L	Conductivity under illumination

σ_D	Conductivity without illumination
S	Photosensitivity
R	Responsivity
T	Temperature
t	Thickness
E_a	Activation energy
E_g	Band gap
at.%	Atomic percentage
h ν	Photon energy
h	Plank's constant
K	Kelvin
K_b	Boltzmann constant
Å	Angstrom
α	Alpha
A	Ampere
cm	Centimeter
μ	Micro
min	Minute
λ	Lambda
V	Voltage
Ω	Ohm
S	Siemen
sec	Second
θ	theta

CHAPTER – 1

CHAPTER 1

INTRODUCTION

Overview:

This chapter describes brief introductory information about thin film technology, compound semiconductors, and photodetectors. Further, the literature survey about the selected crucial materials is discussed in brief. The possible research gaps are identified from the literature review which is mentioned in the scope. Finally, the objectives of the present investigations are drawn from the scope. Lastly, the outline of the thesis is presented at the end of this chapter.

1.1 Thin film technology

The field of material science and engineering community's ability to conceive the novel materials with an extraordinary combination of chemical, physical and mechanical, properties have changed the modern society. The modern era in which we live in, is in quest of materials that would satisfy the thirst of the ever-blooming technology. The technology and understanding of materials with less than 1-micron thickness have made remarkable advances in the last decade, primarily because of the industrial demand for reliable thin-film microelectronic devices to fulfill the urgent needs of the modern era. This progress has brought maturity and much scientific confidence in using thin films for basic and applied research in addition to major contributions to a variety of new and scientifically based technologies. Thin film science and technology is playing an important role in the development of devices ranging from energy-efficient display devices to energy harvesting and energy storage devices such as solar cells, sensors, memory, battery, super-capacitors, etc. A thin film is a layer of material ranging from fractions of a nanometer to several micrometers in thickness. The physical properties of solid bulk materials are almost independent of their thickness. However, a drastic reduction in the thickness may change the properties of the solid materials. When the thickness is much smaller than a micrometer, the properties of the material may depend

on its thickness. Such materials whose properties change as a function of their thickness are called thin films. Unique phenomena related to thin films are the consequence of their small thickness, large surface to volume ratio, and distinctive physical structure, planar geometry, and size. The properties of a thin film not only rely on the thickness of the film but also on the nature of the substrate upon which the films are grown and the deposition parameters used in the fabrication of the thin films. Thin film fabrications are carried out by depositing the required material in the atomistic deposition over the required substrate, which may result in either single crystalline, polycrystalline or amorphous structure depending on the deposition conditions. Thin film technology has the potential to engineer various properties such as surface morphology, surface roughness, porosity, and crystallite size. These advantages in the growth process of thin film assist in the development of new products and minimize the wastage as in conventional manufacturing techniques.

1.2 Compound semiconductors

Semiconductors play an essential role in the modern era because of its sustainable applications in almost all branches of industry. The vast usage of semiconductors in numerous applications is due to the low mobile carrier concentration that leads to the easier interpretation of electronic processes when compared to metals and crystals. Based on the constituent atoms in it, semiconductors can mainly be classified into two major types viz., elemental and compound semiconductors. In elemental semiconductors, all the constituent atoms are of the same kind, whereas a compound semiconductor comprises atoms of two or more different elements. The hierarchy of the compound semiconductors is shown below:

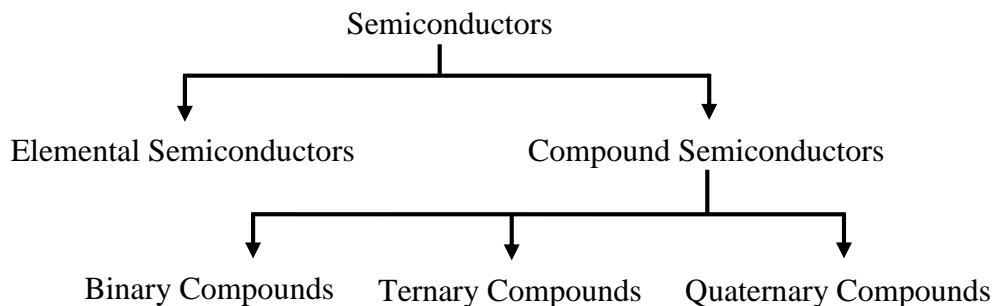


Figure 1.1 Classification of semiconductors.

The scope of materials that can be classified as compound semiconductors is vast and covers the entire periodic table. It includes IV-IV, II-IV, I-V, II-V, III-V, I-VI, II-VI, III-VI, IV-VI, I-VII, I-III-VI, I-IV-VI, and II-III-V compounds. Among the semiconducting materials, silicon (Si) and III-V compounds such as gallium nitride (GaN) are the most used materials in device applications. This is due to the understanding and ability to control their properties gained from the extensive studies carried out. On the other hand, a large amount of effort has been focused on the II-VI and IV-VI compounds but less success was achieved because of the peculiar nature of defects with these groups of materials. Thus, to achieve a successful device application, one needs to understand and surmount the difficulties in these materials. This thesis explores the various properties of few of the II-VI and IV-VI binary group elements namely zinc sulfide (ZnS), cadmium sulfide (CdS), and tin sulfide (SnS) and a few ternary semiconductors viz. $\text{Cu}_x(\text{ZnS})_{1-x}$, $\text{Zn}_x\text{Cd}_{1-x}\text{S}$, and $\text{Zn}_x\text{Sn}_{1-x}\text{S}$ thin films. Some of the important parameters of ZnS, CdS, and SnS are charted below:

Table 1.1 A few crucial parameters of ZnS, CdS and SnS materials.

Property	Zinc Sulfide	Cadmium Sulfide	Tin Sulfide
Linear Formula	ZnS	CdS	SnS
Molecular Weight (g/mol)	97.47	144.46	150.77
Density (g/cm ³)	4.09	4.82	5.22
Melting Point (K)	2,123	2,023	1,155
Conductivity type	n-type	n-type	p-type
Band gap (eV)	3.4 – 3.9	2.42 - 2.45	1.2 – 1.6
Cell Parameters (Å)	Cubic: a = 5.41 Hexagonal: a = 3.811, c = 6.234	Cubic: a = 5.832 Hexagonal: a = 4.16, c = 6.756	Orthorhombic: a = 11.18, b = 3.98, c = 4.32

1.3 Photodetector

Light sensing in the range of the ultraviolet-visible (UV-vis) to near-infrared (NIR) region is of considerable importance for all kinds of scientific and industrial applications such as environmental monitoring, image sensing, communication, day and night surveillance, remote control, chemical/ biological sensing and wide spectral switches (Hu et al. 2014; Jie et al. 2006; Tao et al. 2015). Based on the wavelength range of operation, photodetectors are generally classified into two kinds of sub-systems: narrow-band response detectors (UV, vis and infrared) and broadband response detectors (Mahdi et al. 2016). A photodetector is a device that measures the photons or optical power by converting the energy of the absorbed photons into a measurable form. The photodetectors have commonly two principle classes, thermal detectors and photoelectric detectors (Kruse 1995). Thermal detectors work on the principle of the photothermal effect, which converts optical energy into heat energy. The thermal detectors are comparatively slow and not much more efficient, as time is required to show the effect of temperature change. The principle of the photoelectric detector is based on the photoelectric effect, which refers to the emission or ejection of electrons or electron-hole pairs from the surface of the material in response to the incident light. The response of the photoelectric detector is based on the wavelength of the optical signal incident on it whereas thermal detectors are wavelength-independent. The photoelectric detectors have much more spectral sensitivity than the thermal detector. Thermal detectors are mostly used in the infrared region. The photoelectric detectors are often used for the detection of optical signals in optoelectronic devices. The modern photodetectors are based on the internal photoelectric effect in which photogenerated charge carriers remain in the material, help to increase its conductivity. The photon of energy equal to the band gap energy of the material is incident on the material producing electron-hole pairs which are separated by an applied electrical field (Razeghi and Rogalski 1996). Depending on the photogeneration process of charge carriers, there are two principal types of photoconductivity, (a) intrinsic photoconductivity and (b) extrinsic photoconductivity (Jia-ming Liu 2005). The intrinsic photoconductivity is because of the excess electrons and holes that are generated by the absorption of incident photons in the intrinsic semiconductors and band-to-band transition occurs in the semiconductor, as shown in Fig. 1.2 (i). The

extrinsic photoconductivity is lent by the charge carriers that are generated by transitions occurred within impurity levels present in the band gap of an extrinsic semiconductor. In an n-type extrinsic semiconductor, the impurity levels are called donor levels with energy E_d present below the conduction band, electrons are excited from these donor levels to the conduction band, as shown in Fig. 1.2 (ii). In a p-type extrinsic semiconductor, the impurity levels called as acceptor levels with energy E_a are present above the valence band; electrons are excited from the valence band to these acceptor levels, as shown in Fig. 1.2 (iii). Photoconductive detectors cover a broad spectral range of the electromagnetic light spectrum from the ultraviolet to the far-infrared. Both direct and indirect semiconductors are used for the photoconductive detectors. Many intrinsic semiconductors like group IV semiconductors, III–V, II–VI and IV–VI compounds are being used as intrinsic photodetectors. These intrinsic photodetectors mainly show spectral responsivity in the visible and near-infrared regions.

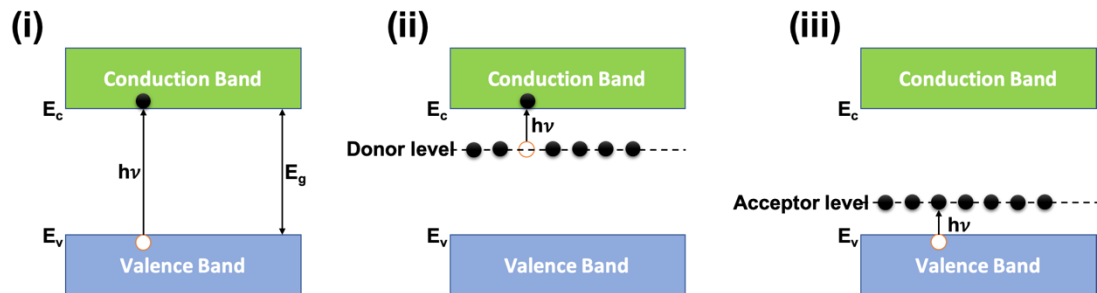


Figure 1.2 Internal photoelectric effect (i) intrinsic photoconductivity, (ii) n-type extrinsic photoconductivity, and (iii) p-type extrinsic photoconductivity.

1.4 Literature survey

Investigation on growth and characterization of inorganic semiconducting thin films has attained remarkable development in the last two decades for the use in optoelectronic devices (Broser et al. 1992; Popescu 1999; Sasikala et al. 2000; Takokoro et al. 1993). Specifically, the II-VI group compounds such as ZnS, CdS, CdSe, ZnTe, ZnO, and ZnSe are well-recognized and have been intensively studied due to their attractive magnetic, luminescence, and opto-electrical properties (Barman et al. 2018; Garcia et al. 2003; Das and Jayaraman 2014; Kaneko et al. 2016; Karunagaran et al. 2007; Nazzal et al. 2003; Späth et al. 2005). Among these II-VI semiconductors, zinc

and cadmium compounds are extensively studied due to their suitability for photovoltaic applications since they are direct band gap semiconductors and have high absorption coefficients (Patidar et al. 2008).

ZnS is a non-toxic element, has n-type conductivity and a wide direct band gap of 3.52 eV (Hennayaka and Lee 2013). It can crystallize in either cubic (Benyahia et al. 2015b) or hexagonal structure (Huang et al. 2009). In each form, the coordination geometry at Zn and S is tetrahedral. The more stable cubic form is known also as zinc blende or sphalerite. The hexagonal form is known as the mineral wurtzite, although it also can be produced synthetically. The transition from the sphalerite form to the wurtzite form occurs at around 1293K. ZnS can be doped as either an n-type semiconductor or a p-type semiconductor. Due to its wide band gap and excellent transparency, chemical, and mechanical stability (Bacha et al. 2016), it can be utilized in opto-electrical devices such as a window layer in thin film photovoltaics (Nakada et al. 2001), cathode ray tubes (Davies et al. 2001), light emitting diodes (Kim et al. 2011), and electroluminescent displays (Larson et al. 2016). Numerous techniques are available to deposit ZnS thin films such as thermal evaporation (Benyahia et al. 2015b), pulsed laser deposition (Ming et al. 2013), chemical bath deposition (Iwashita and Ando 2012), spray pyrolysis (Zeng et al. 2013b), dip coating (Farid et al. 2014), R.F. sputtering (Kedawat et al. 2011), etc. In 2001, Nakada et al. fabricated Cu(In,Ga)Se₂ (CIGS) thin film solar cells using ZnS thin film as a buffer layer and studied the effect of annealing after the deposition to optimize the performance. They obtained an efficiency of 16.9 % with $V_{oc} = 0.647$ V, $J_{sc} = 35.2$ mA/cm², Fill Factor (FF) = 74.3% over an active area of 0.2 cm² under the illumination of AM 1.5, 100 mW/cm². Later, the same group Nakada and Mizutani 2002, fabricated CIGS solar cell with a 130 nm thick, chemical bath deposited (CBD)-ZnS buffer layer and obtained an efficiency of 18.1% with $V_{oc} = 0.671$ V, $J_{sc} = 34.9$ mA/cm², FF = 77.6 % for an active area of 0.155 cm². The cell performance, however, deteriorated in devices with a 200 nm thick CBD-ZnS layer since the series resistance of the solar cell increased due to the high resistance of the CBD-ZnS layer. In 2004, Bhattacharya and Ramanathan demonstrated that the interfacial reaction that occurs in the chemical bath deposition of ZnS buffer layers could produce high-efficiency solar cells on CIGS - based absorbers. Devices with efficiencies as high as 17.4 % were obtained by using two-layer CBD ZnS(O, OH) on

the CIGS absorber. The solar cell parameters for this device were: $V_{oc} = 0.678$ V, $J_{sc} = 35.74$ mA/cm², and fill factor = 72 %. In 2009, Islam et al. investigated CIGS solar cell performance with the Molecular Beam Epitaxial (MBE) grown ZnS buffer layer. It was possible to obtain photo-response from the shorter wavelength region using the ZnS buffer layer although overall cell performance was weak compared to the standard Cadmium Sulfide (CdS) based cell. Using the double buffer layer composed of ZnS/CdS, a solar cell with an efficiency of 16.87 %, $J_{sc} = 33.2$ mA/cm², $V_{oc} = 0.685$ V and FF = 74 % were obtained for an active area of 6.2×10^{-6} m². In 2014, Kim et al. have fabricated ZnS buffer layers on (Copper Zinc Tin Sulfide) CZTS absorber layers by using a conventional RF magnetron sputtering technique and studied the effect of ZnS buffer layer film thicknesses along with a CZTS absorber layer. The solar cell conversion efficiency (η) of 2.11 % for the active area of 0.44 cm² was obtained with ZnS buffer layer having a thickness of ~ 30 nm. Recently in 2017, Qiu et al. have investigated the optical and electrical properties of thermally evaporated ZnS thin films and ZnS/p-Si heterojunction solar cells. The power conversion efficiency (PCE) of the hydrogen doped aluminum zinc oxide (HAZO)/ZnS/textured p-Si heterojunction solar cells was found to be 8.83 % with $V_{oc} = 0.517$ V, $J_{sc} = 31.047$ mA/cm² and FF = 55 %. Long-term stability of the solar cell was also studied.

Cadmium sulfide is a vital n-type compound (II-VI) semiconductor material and can occur in either cubic or hexagonal phase or also as a combination of both the phases. In both of these forms, the cadmium and sulfur atoms are four coordinates. It is having a direct optical energy band gap of ~2.42 eV and is a potential candidate for optoelectronic devices (Broser et al. 1992; Popescu 1999; Sasikala et al. 2000; Takokoro et al. 1993) due to its attractive opto-electrical properties. In particular, cadmium sulfide thin films are extensively used as a window layer in CIGS, CdTe and CZTS based photovoltaic cells (Ramanathan et al. 2003; Romeo et al. 1999; Yin et al. 2015). Hence, an enormous amount of findings has been carried out on the growth and optimization of CdS thin films with noble opto-electronic characteristics for solar cell applications. Numerous methods such as sputtering (Moon et al. 2006), vacuum thermal evaporation (Sahay et al. 2007), chemical bath deposition (Hariskos et al. 2001), spray pyrolysis (Yadav and Masumdar 2011), etc. are widely used to grow CdS thin films. CdS is extensively used as window material in non-linear optical devices and

photovoltaic cells. But the absorption loss of CdS thin films in the blue region limits the efficiency of the photovoltaic cells (Aguilar-Hernández et al. 2006) which can be overcome by using a relatively wider band gap material than CdS. Back in 1965, A. Kunioka and Y. Sakai first reported the optical and electrical properties of selenium/cadmium sulfide photovoltaic cells prepared by vacuum evaporation of CdS on Se layer. The spectral sensitivity was compared with human eye sensitivity and it was observed that the spectral sensitivity was very close to the visual sensitivity. In 1976, Kazmerski et al. fabricated p-CuInSe₂/n-CdS heterojunction thin film solar cells. The solar cells exhibited efficiencies in the range of 4 – 5 % over an active area of 1.2 cm² under 100 mW/cm² tungsten-halogen illumination. In 1982, YS and Perez-Alburne reported very efficient thin film CdS/CdTe solar cells prepared using a close-spaced-sublimation technique. Under simulated AM2 illumination, at 75 mW/cm², the cells had a typical output of V_{oc} about 750 mV, J_{sc} about 17 mA/cm², F.F. (fill factor) of about 62 %, and efficiency ~10.5 % at room temperature. Later in 1997, a CdTe/CdS based solar cell with 16 % efficiency was reported by Aramoto et al. The device consisted of an ultra-thin layer of 50 nm thick CdS and a 3.5 μm thick CdTe. A high current density of 26.08 mA, high open circuit voltage of 840 mV/cm² and a fill factor of 73 % was achieved for an active area of 1 cm². In 2001, Wu et al. reported CdS based CdTe solar cell with an efficiency of 16.5 % over an active area of 1.032 cm². The device had a structure of (cadmium stannate) CTO/(zinc stannate)ZTO/CdS/CdTe and V_{oc} = 845.0 mV, J_{sc} = 25.88 mA/cm², and FF = 75.51 %. In 2005, Ramanathan et al. reported CIGS/CdS based solar cell. A very thin 50 – 60 nm layer of CdS was used as a buffer layer to CIGS absorber. The device showed the following parameters: V_{oc} = 701 mV, J_{sc} = 34.60 mA/cm², FF = 79.65 %, and efficiency = 19.3 %. Analysis of the current-voltage curves showed that the high efficiency is related to low ideality factors and low reverse saturation current densities. In 2011, Cu₂ZnSnS₄ solar cells with CdS buffer layer having an efficiency of 8.4% was reported by Byungha Shin et al. The device had an structure of Mo/MoS_x/CZTS/CdS/i-ZnO/Al:ZnO/MgF₂ and V_{oc} = 661 mV, J_{sc} = 19.5 mA/cm² and FF = 65.8%. Recently in 2017, Lu et al. fabricated CdS buffer layer on CIGS absorber layer using cadmium acetate as a precursor. The device with CdS buffer layer deposited at 0.052M cadmium acetate showed the best efficiency

of 11.42%. Further, the device efficiency was found to be increased to 12.57% after annealing the CdS layer in air at 453K.

$\text{Cd}_x\text{Zn}_{1-x}\text{S}$ thin films can be formed by diffusion of Zn in CdS. The semiconducting properties of the $\text{Cd}_x\text{Zn}_{1-x}\text{S}$ compound can be tuned between the values corresponding to its pure binaries depending on the device requirements. This makes $\text{Cd}_x\text{Zn}_{1-x}\text{S}$ thin films more attractive for the fabrication of solar cells (Zhou et al. 2004). The vacuum thermal evaporation process is a well-known technique that can be used to deposit uniform thin films with very good crystallinity. $\text{Cd}_x\text{Zn}_{1-x}\text{S}$ thin films have been prepared by different methods such as closed spaced sublimation (Mahmood and Shah 2014), vacuum evaporation (Lee et al. 2003a; b; Patidar et al. 2008), chemical bath deposition (Asogwa 2010; Carreón-Moncada et al. 2013; Gaewdang and Gaewdang 2005; Kumar et al. 2011; Mahdi and Al-Ani 2012; Rajathi et al. 2012) and spray pyrolysis (Kumar et al. 2016; Li et al. 2010; Raviprakash et al. 2011).

In recent years, transparent conducting materials (TCMs) are becoming important in opto-electronic applications such as light emitting diodes, photovoltaics, organic electronics, etc. There are many n-type wide band gap materials such as ZnS, ZnO, SnO_2 , etc. which are widely used for transparent electronics. There are relatively fewer reports on the successful fabrication of p-type transparent conducting films. In the area of photovoltaics, p-type TCMs can be used for the cost-effective synthesis of heterostructured thin film devices with intrinsically n-type materials. Also, the performance of multi-junction solar cells could be enhanced by using p-type TCMs which would facilitate the collection of photogenerated charges independently from each absorber layer and thus improving the overall efficiency. In practical applications, the crucial challenge in using p-type TCMs is the performance, particularly the combination of transparency and hole conductivity. Considerable efforts have been made to fabricate p-type ZnO (Lander 1960; Minegishi et al. 1997), ZnS (Iida et al. 1990) and ZnSe (Park et al. 1990), but the reliability of p-type doping still remains controversial (Look et al. 2002). In addition to the above binary compounds, p-type transparent ternary and quaternary compounds have begun to attract attention. In 1997, the first p-type ternary TCM CuAlO_2 was reported which had a hole conductivity of $\sim 1 \text{ S cm}^{-1}$ and an average optical transparency of 70% (Kawazoe et al. 1997). Since then, significant efforts have been made to improve the performance of p-type TCMs

(Banerjee and Chattopadhyay 2005; Saritha et al. 2016). In spite of these efforts, properties of these materials are quite inadequate for the device application, and the fabrication of transparent p-type materials still remains a major challenge. Recently, chemical bath deposition and pulsed laser deposition of p-type $\text{Cu}_x\text{Zn}_y\text{S}$ thin films were reported (Diamond et al. 2012; Ortíz-Ramos et al. 2014; Xu et al. 2016), respectively. The band gap of $\text{Cu}_x\text{Zn}_y\text{S}$ thin films varies from 2.1 to 3.5 eV depending upon x and y ratio which makes $\text{Cu}_x\text{Zn}_y\text{S}$ another interesting candidate for p-type TCMs as well as buffer/window layer in solar cells.

The semiconductors from IV-VI group have been drawing much attention in optoelectronic devices and solar cells due to their potential application. In recent years, among the IV-VI group members, tin monosulfide (SnS) is attracting great interest as an absorber layer in the fabrication of photovoltaic devices due to its favorable optical bandgap energy, great optical absorption coefficient and high optical transmittance (Gunasekaran and Ichimura 2007). SnS compound was first reported by a German mineralogist Robert Herzenberg in the year 1932. Since then, many studies on the structural, optical and electronic properties as well as its peculiarities with synthesis parameters and fabrication techniques were performed. SnS is a p-type semiconductor which is comprised of cheap and non-toxic elements. It can crystallize in cubic (Chalapathi et al. 2016; Garcia-Angelmo et al. 2015) as well as orthorhombic (Nair et al. 2016) structures. It has been reported having bandgap in a wide range varying from 0.9 eV to 1.8 eV (Sns et al. 2013) and has an absorption coefficient of above 10^4 cm^{-1} (Wangperawong et al. 2014). These excellent properties make it a potential alternative than more studied absorbers like CIGS and CdTe (Major et al. 2014; Niki et al. 2010; Ramanujam and Singh 2017; Wu 2004). The highest reported efficiency for SnS based heterojunction was 4.4% (Sinsermsuksakul et al. 2014) which is drastically lower the theoretical estimation of 24% as predicted by Lofersky's bandgap analysis (Loferski 1956). This low efficiency is mainly due to the low quality of material, poor microstructure and existence of supplementary phases like SnS_2 and Sn_2S_3 during the formation of SnS thin films (Banai et al. 2016). Back in 1988, Sharon and Basavaswaran reported a photoconversion efficiency of 0.63 % for a photoelectrochemical cell (PEC) with the structure: n-SnS/ $\text{Ce}^{4+}/\text{Ce}^{3+}/\text{Pt}$. SnS thin films were synthesized by passing H_2S through a solution of SnCl_2 . Hall measurements

revealed donor concentration and mobility of major carrier as $2.28 \times 10^{16} \text{ cm}^{-3}$ and $11.4 \text{ cm}^2\text{V}^{-1}\text{s}^{-1}$ respectively. By the year of 1994, Noguchi et al. successfully deposited SnS thin films by vacuum evaporation technique and fabricated an ITO/n-CdS/p-SnS/Ag structure solar cell. It exhibited a short circuit current density (J_{sc}) of 7 mA/cm^2 , an open-circuit voltage (V_{oc}) of 0.12 V , a fill factor (FF) of 35% and a conversion efficiency of 0.29% . The as-grown SnS films showed p-type conduction with a resistivity of $13 \sim 20 \text{ }\Omega\text{cm}$, a carrier density of $6.3 \times 10^{14} \sim 1.2 \times 10^{15} \text{ cm}^{-3}$, and a Hall mobility of $400 \sim 500 \text{ cm}^2/\text{Vs}$. A SnS/CdS photovoltaic study was done by Ramakrishna Reddy et al. in the year 2006 where the SnS films were synthesized by spray pyrolysis technique and exhibited an efficiency and quantum efficiency (QE) of 1.3 and 70% , respectively. The efficiency was found to be low because the thickness of SnS used in this work was very thin ($0.6\mu\text{m}$). They reported that by increasing the thickness to $>1.5\mu\text{m}$, a substantial increase in V_{oc} can be expected. The methodology on the preparation as well as chemical, structural and physical characterization results of the Mo/p-SnS/n-CdS/ZnO heterojunctions were reported by Bashkirov et al. in 2012. The SnS thin films were grown by hot wall vacuum deposition (HWVD) method on the Mo-coated glass substrates at $543\text{--}623\text{K}$. The CdS buffer layers were deposited onto the SnS films by chemical bath deposition. The ZnO window layers were deposited by a two-step RF magnetron sputtering method, resulting in a ZnO bilayer structure: the first layer consists of undoped i-ZnO and the second of Al-doped n-ZnO. The best junction exhibited the following parameters: $V_{oc} = 132 \text{ mV}$, $J_{sc} = 3.6 \text{ mA/cm}^2$, $\text{FF} = 29 \%$ and $\eta = 0.5 \%$. An efficiency of 2.46% was achieved for SnS-based thin film solar cells having a device structure of Mo/SnS/Zn(O,S)/ZnO/ITO by varying the oxygen-to-sulfur ratio in Zn(O,S) layer by Sinsersuksakul et al. in 2013. Studies showed that increasing the sulfur content in Zn(O,S) raises the conduction band offset between Zn(O,S) and SnS to an optimum slightly positive value. The SnS/Zn(O,S) solar cell with a S/Zn ratio of 0.37 exhibited a short-circuit current density (J_{sc}), open circuit voltage (V_{oc}), and fill factor (FF) of 19.4 mA/cm^2 , 0.244 V , and 42.97% , respectively. In 2014, Sinsersuksakul et al. reported an efficiency of 4.36% by adding a SnO_2 layer of few nanometers at SnS/Zn(O,S) interface of Mo/SnS/Zn(O,S)/ZnO/ITO solar cell. The conduction band minimum of Zn(O,S) was lowered by reducing the sulfur content to form an optimum spike with the annealed SnS and the carrier concentration of the

oxygen-rich Zn(O,S) was decreased by nitrogen doping to restore the diode quality. A variety of techniques are available to deposit SnS thin films like electrochemical deposition (Gunasekaran and Ichimura 2007), radio frequency sputtering (Arepalli et al. 2019; Jiang et al. 2014; Minnam Reddy et al. 2015; Zhao et al. 2016), spray pyrolysis (Alam and Dutta 2015; Arulanantham et al. 2018; Ramakrishna Reddy et al. 2006; Sall et al. 2017), chemical bath deposition (Chaki et al. 2016; Chalapathi et al. 2016; Gedi et al. 2015, 2016; Nair et al. 2016), vacuum thermal evaporation (Basak et al. 2018; Kawano et al. 2015; Robles et al. 2015a; b), electron beam evaporation (Caballero et al. 2016), and chemical vapor deposition (Sánchez-Juárez et al. 2005).

One can tune the distinct properties of ZnS and SnS thin films by alloying them to form $Zn_xSn_{1-x}S$ thin films. Due to the large difference in their optical band gap values, the band gap of the $Zn_xSn_{1-x}S$ thin films can be altered from 1.5 eV to 3.5 eV by varying the composition 'x'. This makes $Zn_xSn_{1-x}S$ thin films an interesting candidate for various opto-electrical devices. The opto-electrical properties of the $Zn_xSn_{1-x}S$ films can be tuned to a value according to the requirement of the device.

1.5 Scope of the Work

Literature survey reveals the importance of materials such as ZnS, SnS and CdS in the field of opto-electronic devices. Majority of the studies on these materials and their compounds are mainly focused on the implementation of the materials in the field of solar cells. Various techniques are available to grow thin films of these materials. Among these techniques, the thermal evaporation method is a well-established method that can be used to deposit uniform thin films with very noble crystallinity and purity. A very few studies have been carried out on the investigation of these materials as a photodetector using a thermal evaporation method. One approach to enhance the properties of a material is through surface modification by the proper choice of dopants or by alloying. Hence, the present work focuses on the preparation of binary sulfides viz., ZnS, CdS, SnS and ternary sulfides viz., $Cu_x(ZnS)_{1-x}$, $Zn_xCd_{1-x}S$ and $Zn_xSn_{1-x}S$ thin films using thermal evaporation method and their characterization towards bandgap engineering and photo sensing properties.

1.6 Objectives

- i. To optimize the growth conditions of metal sulfides like ZnS, CdS, and SnS thin film using thermal evaporation technique.
- ii. To study the structural, morphological, compositional, optical and electrical properties of the grown metal sulfides thin film.
- iii. To optimize the growth conditions of doped/mixed metal sulfides thin film using thermal evaporation technique.
- iv. To study the structural, morphological, compositional, optical and electrical properties of the doped/mixed metal sulfides thin film.
- v. To study the suitability of these materials as a photodetector.

1.7 Thesis outline

This dissertation is focused on the application of metal sulfide thin films for photodetector applications as well as towards band gap engineering of the materials. The thesis comprises of 5 chapters as mentioned below:

Chapter–1 gives a brief introduction to thin films, compound semiconductors, photodetector, few important materials used for opto-electronic devices along with their literature survey, the scope of the present work and the objectives.

Chapter–2 is devoted to the experimental technique involved to deposit the thin films and the several characterization methods followed to analyze the various properties of the films.

Chapter–3 discusses the preparation of binary sulfides i.e., ZnS, CdS and SnS thin films using thermal evaporation method. The role of substrate temperature on the different properties of the films is reported. In addition, the photodetector properties of the CdS and SnS films are investigated.

In chapter–4, the synthesis of ternary alloys namely $\text{Cu}_x(\text{ZnS})_{1-x}$, $\text{Zn}_x\text{Cd}_{1-x}\text{S}$, and $\text{Zn}_x\text{Sn}_{1-x}\text{S}$ thin films using a thermal evaporation method are described. The various properties of the ternary alloyed films are then analyzed using different characterization

techniques. The excellent transparent conducting behavior of the $\text{Cu}_x(\text{ZnS})_{1-x}$ is reported. Lastly, the outstanding photosensitivity studies of $\text{Zn}_x\text{Cd}_{1-x}\text{S}$ and $\text{Zn}_x\text{Cd}_{1-x}\text{S}$ thin films along with the band gap engineering of the films are described in this chapter.

Chapter-5 reports the conclusion drawn from all the investigations carried out on both the binary and ternary compound semiconductors.

CHAPTER – 2

CHAPTER 2

THIN FILM: DEPOSITION AND CHARACTERIZATIONS

Overview:

This chapter explains the methods which were used for cleaning the substrates, technique used for depositing the films, characterization techniques and working formulae used to estimate the thickness, structural, and opto-electrical properties of the films. In addition, the basic principles of the various methods are described here.

2.1 Cleaning of the substrates

The glass substrates used for this study were cleaned by dipping the borosilicate glass in a chromic acid solution for 12 hours. Then the substrates were washed with running de-ionized (DI) water followed by ultra-sonicating with acetone and DI water for 15 mins each, respectively. Lastly, the films were dried inside a hot air oven at 473K for a duration of 6 hrs.

2.2 Thermal evaporation method

Thin films can be deposited via various physical and chemical routes. The thermal evaporation method shows some advantages such as the impurity amount associated with the growing layer is minimum, the tendency of forming oxides is considerably low, high reproducibility and high deposition rate. Therefore, the thermal evaporation technique has been the most suitable method to grow thin films owing to the very high deposition rate, low material consumption and low cost of operation.

In the thermal evaporation process, the material to be evaporated is kept on an evaporation source (can be either a filament or boat or crucible) and a substrate is located at an appropriate distance facing the evaporation source as shown in figure 2.1. The material used to fabricate the evaporation source should be having a higher melting temperature than the material to be evaporated. Generally, the evaporation sources are made up of tungsten or molybdenum. Both the source and the substrate are located inside a high vacuum chamber. The substrate can also be heated or electrically biased

or rotated during deposition. The desired vapor pressure of source material can be generated by simply heating the source to elevated temperatures, and the concentration of the growth species in the gas phase can be easily controlled by varying the source temperature and the flux of the carrier gas.

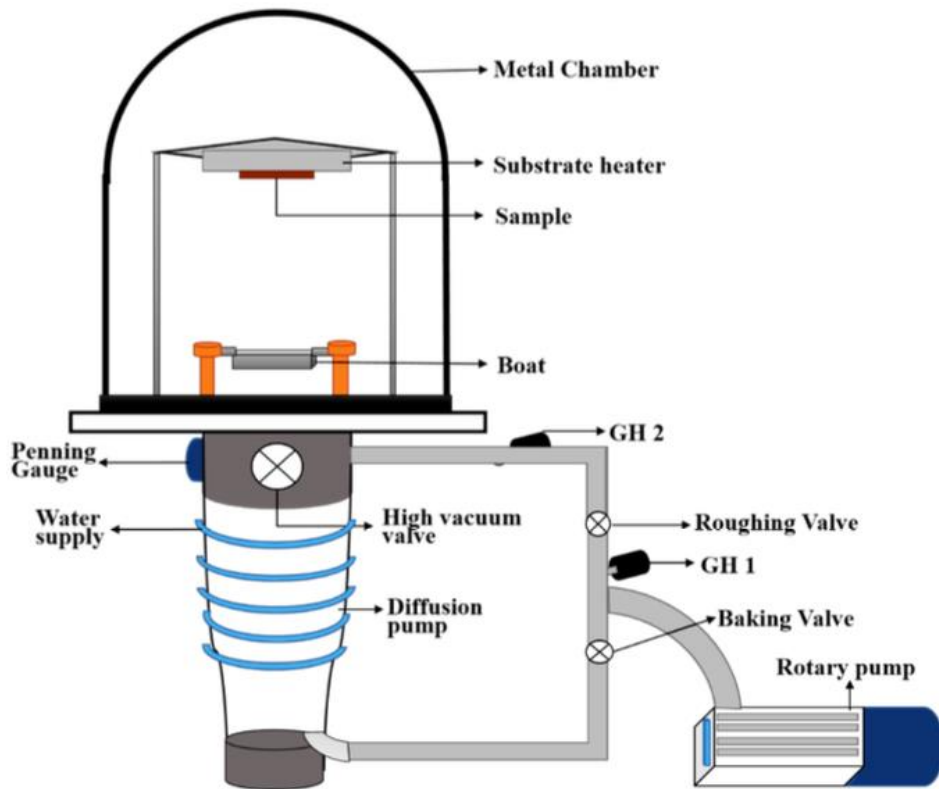


Figure 2.1 Schematic of thermal evaporation technique

2.3 Characterization techniques

2.3.1 Thickness measurement method

The thickness of a film is an essential factor that determines various properties of a thin film. There are many methods to measure the thickness of the films namely quartz crystal microbalance, surface profilers, interferometry, gravimetric method and through a cross-sectional image of the scanning electron microscope (SEM). In the present study, the thickness of the film was calculated using a simple weight difference process known as a gravimetric method employing a sensitive electronic microbalance (Sartorius BT 124 S). Here, the thickness of the film (t) was determined using the following formula.

$$t = \frac{m_2 - m_1}{\rho A} \quad (2.1)$$

where ' m_2 ' is the weight of the substrate after deposition, ' m_1 ' is the weight of the substrate before deposition, ' A ' is the deposited film area (in cm^2), and ' ρ ' is the film material density (in g/cm^2).

2.3.2 X-ray diffraction (XRD)

X-ray diffraction is a rapid analytical technique primarily used for phase identification of a crystalline material and can provide information on unit cell dimensions. There are different types of X-ray diffractometers available for crystal structure analysis. The most commonly used diffractometer is known as Powder Diffractometer or Debye-Scherrer Diffractometer named after its inventors. X-ray diffraction is based on the constructive interference of monochromatic X-rays and a crystalline sample. These X-rays are generated by a cathode ray tube, filtered to produce monochromatic radiation, collimated to concentrate, and directed toward the sample. The interaction of the incident rays with the sample produces constructive interference (and a diffracted beam) when conditions satisfy Bragg's Law. This law relates the wavelength of electromagnetic radiation to the diffraction angle and the lattice spacing in a crystalline sample. These diffracted X-rays are then detected, processed and counted. By scanning the sample through a range of 2θ angles, all possible diffraction directions of the lattice should be attained due to the random orientation of the powdered material. Conversion of the diffraction peaks to d-spacings allows identification of the mineral because each mineral has a set of unique d-spacings. Typically, this is achieved by comparison of d-spacings with standard reference patterns. All diffraction methods are based on the generation of X-rays in an X-ray tube. These X-rays are directed at the sample, and the diffracted rays are collected. A key component of all diffraction is the angle between the incident and diffracted rays.

In the current study, the structural characterization of the films was carried out by an X-ray diffractometer (Rigaku MiniFlex 600) using $\text{Cu K}\alpha$ radiation with a wavelength of 1.5418 \AA . The interplanar distance ' d ' for the various diffraction peaks were calculated using Bragg's relation:

$$n\lambda = 2d_{hkl} \sin \theta \quad (2.2)$$

The crystallite size 'D' (nm) of the investigated films was calculated by using the Scherrer's formula:

$$D = \frac{0.94\lambda}{\beta \cos \theta} \quad (2.3)$$

where ' λ ' is the wavelength of the X-ray used and ' β ' is the full width at half maximum of the diffraction peak at 2θ , where θ is the Bragg diffraction angle.

The lattice constant 'a' for cubic phase was determined by the following relation:

$$a = \frac{d}{\sqrt{(h^2 + k^2 + l^2)}} \quad (2.4)$$

The lattice parameters (a, c) for the hexagonal crystal system was calculated using the below relation.

$$\frac{1}{d^2} = \frac{4}{3} \frac{(h^2 + hk + k^2)}{a^2} + \frac{l^2}{c^2} \quad (2.5)$$

2.3.3 Scanning electron microscope (SEM)

A Scanning Electron Microscope (SEM) is a type of electron microscope that produces images of a sample by scanning it with a focused beam of electrons. The electrons interact with atoms in the sample, producing various signals that contain information about the sample's surface topography and composition.

In Figure 2.2, essential parts of a Scanning Electron Microscope are shown. In an electron microscope, electrons emitted from a hot filament are usually used. However, sometimes cold cathode (a cathode that emits electrons without heating it) is also used. A cold cathode emits electrons under the application of a very high electric field. It is also known as a Field Emitter Scanning Electron Microscope (FE-SEM). In a Scanning Electron Microscope, backscattered electrons or secondary electrons are detected. In an electron microscope, the electron beam can be focused to a tiny spot size using electrostatic or magnetic lenses. Usually, the electrostatic lenses are used for SEM. The fine beam is scanned or rastered on the sample surface using a scan generator and backscattered electrons are collected by an appropriate detector. The signal from the scan generator along with the amplified signal from the electron collector generates the image of the sample surface. In order to avoid the oxidation and contamination of

filament as well as reduce the collisions between air molecules and electrons, filament and sample are housed in a vacuum chamber. Usually, vacuum $\sim 10^{-2} - 10^{-3}$ Pa or better is necessary for the normal operation of Scanning Electron Microscope.

One disadvantage of electron microscopes is that insulating samples cannot be analyzed directly as they get charged due to incident electrons and images become blurred/faulty. Therefore, insulating solids are coated with a very thin metal film like gold or platinum (<10 nm) making them conducting without altering any essential details of the sample. The metal film is usually sputter coated on the sample to be investigated prior to the introduction into the electron microscope. Electron microscopes can also be used to obtain the composition of a sample using a technique known as Energy Dispersive Analysis of X-rays (EDAX or EDX). In the present study, surface morphology was captured using the Zeiss-Sigma FE-SEM model. The FE-SEM is capable of capturing an image with a resolution of 1nm at an accelerating voltage of 20kV. Accelerating voltage of 5kV with a working distance of 5-8mm was used during the present study. Since the samples were deposited on a non-conducting soda-lime glass substrate, all the samples were sputtered with a thin layer of gold and conductivity between the surface of thin film to sample holder was established using carbon tape.

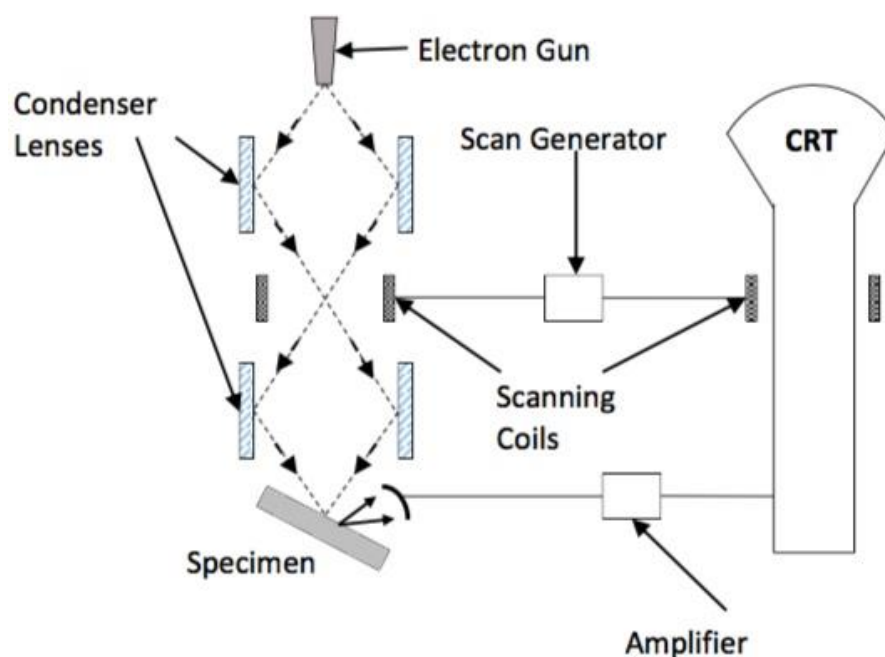


Figure 2.2 A typical sketch of a Scanning Electron Microscope

2.3.4 Energy dispersive analysis of X-rays (EDAX)

Interaction of the primary beam with atoms in the sample causes shell transitions which result in the emission of an X-ray. The emitted X-ray has an energy characteristic of the parent element. Detection and measurement of the energy permit elemental analysis (Energy Dispersive X-ray Spectroscopy or EDS). EDS can provide rapid qualitative, or with adequate standards, quantitative analysis of elemental composition with a sampling depth of 1-2 microns. X-rays may also be used to form maps or line profiles, showing the elemental distribution in a sample surface.

2.3.5 UV-Vis-NIR spectroscopy

Optical absorption spectroscopy is a handy technique to study metals, semiconductors, and insulators in bulk, colloidal, thin film and nanostructure forms. Semiconducting as well as some insulating materials have an optical energy gap. When the energy of photons is insufficient to excite electrons from valence band to conduction band, no absorption takes place. At some critical photon energy, a sudden rise in absorption occurs as the energy of photons is just sufficient to excite the electron to conduction band minimum. At still shorter wavelengths or higher energy photons continue to get absorbed. The absorbed (or reflected) intensity as a function of wavelength from ultraviolet (200 nm) to near infra-red (3,000 nm or many times only up to 1,000 nm) is useful to understand electronic structure and transitions between valence and conduction band of materials.

In order to calculate the energy bandgap (E_g) of the films, Tauc's relation was used (Tauc and Menth 1972):

$$\alpha h\nu = B(h\nu - E_g)^n \quad (2.6)$$

where 'B' is "a parameter that depends on the transition probability" and the exponent 'n' is a value which depends on the transition type "(n = 1/2, 2, 3/2 or 3 for allowed direct, allowed in-direct, forbidden direct or forbidden in-direct transitions, respectively)".

The absorption coefficient (α) of the films was determined from the absorption spectra utilizing the below relation:

$$\alpha = \frac{2.303 * A}{t} \quad (2.7)$$

where 't' is "the thickness of the film" and 'A' is "the absorbance of the film".

2.3.6 Raman spectroscopy

Raman spectroscopy is a spectroscopic technique typically used to determine vibrational modes of molecules, although rotational and other low-frequency modes of systems may also be observed. Raman spectroscopy is commonly used in chemistry to provide a structural fingerprint by which molecules can be identified. Raman spectroscopy relies upon the inelastic scattering of photons, known as Raman scattering. A source of monochromatic light, usually from a laser in the visible, near-infrared, or near ultraviolet range is used, although X-rays can also be used. The laser light interacts with molecular vibrations, phonons or other excitations in the system, resulting in the energy of the laser photons being shifted up or down. The shift in energy gives information about the vibrational modes in the system. Infrared spectroscopy typically yields similar, complementary, information.

Typically, a sample is illuminated with a laser beam. Electromagnetic radiation from the illuminated spot is collected with a lens and sent through a monochromator. Elastic scattered radiation at the wavelength corresponding to the laser line (Rayleigh scattering) is filtered out by either a notch filter, edge pass filter, or a band pass filter, while the rest of the collected light is dispersed onto a detector.

2.3.7 Opto-electrical analysis

The electrical properties of materials may depend on several factors such as deposition technique, optimization condition, thickness, crystallinity, defects, etc. Analyzing the electrical property of material gives insight into many properties of the material, which can be helpful for device fabrication. Thin films prepared using a thermal evaporation technique will be polycrystalline in nature, in which electrical property is dominated by grain boundaries and defects. The current-voltage (I-V) characteristic curves are generally used as a tool to determine and understand the basic parameters of a component or device and which can also be used to mathematically model its behavior within an electronic circuit. In the present study, the electrical parameters were determined using a Keithley 2400 sourcemeter and a Keysight B2985A multimeter. A typical Xenon arc lamp (Oriel Instruments U.S.A., Newport, Model: 66902) was used

as a light source and an optical power meter (Nova P/N 7Z01500, Ophir) was employed to measure the light intensity.

The type of electrical conductivity of deposited thin films was analyzed using a hot probe method. This method is based on the Seebeck effect, in which the sign of thermos-emf generated between hot and cold is used to determine the type of conductivity. A soldering gun was used to heat one terminal and another terminal was maintained at room temperature. Then, the hot end and cold end terminal of the thin film were connected to positive and negative terminals of voltmeter respectively. Because of a thermal gradient, thermally generated charge carriers diffuse from hot end to cold end leading to the development of a potential, which can be measured using a voltmeter. A positive and negative potential develops across the terminals for n-type and p-type materials respectively.

Temperature-dependent resistance measurement was carried out to estimate the activation energy (E_a). The activation energy ' E_a ' associated with the films was calculated using the below equation.

$$E_a = \frac{2.303 * k * slope}{e} \quad (2.8)$$

where ' e ' is "the charge of an electron", ' k ' is "Boltzmann's constant", and the slope was determined from the linear portion of the logarithmic resistance vs inverse temperature ($1/T$) plot.

The photoconductivity of the films was calculated using:

$$\sigma = \frac{It}{VA} \quad (2.9)$$

where ' A ' is "the device area", ' t ' is "the thickness of the film", and ' I ' is "the measured current".

The photosensitivity ' S ' of the films was calculated using the below equation:

$$S = \frac{\sigma_L - \sigma_D}{\sigma_D} \quad (2.10)$$

where ' σ_D ' and ' σ_L ' are "the electrical conductivities of the films without light and with light, respectively".

The photoresponsivity (R) i.e. "the amount of photocurrent generated per unit area per unit illumination intensity" is determined using the below equation:

$$R = \frac{I_{light} - I_{dark}}{L_{\lambda} A} \quad (2.11)$$

where ' I_{dark} ' and ' I_{light} ' are "current following through the sample under dark and illumination", ' A ' is "the effective illumination area", and ' L_{λ} ' is the "incident illumination intensity of the light source".

CHAPTER – 3

CHAPTER 3

STUDIES ON BINARY SULFIDE THIN FILMS

Overview:

This chapter describes the process followed to obtain stoichiometric thin films. In the thermal evaporation technique, the substrate temperature plays a vital role in determining the various properties of a thin film. Herein, the influence of substrate temperature on the structural, morphological, compositional, optical and electrical properties of films is investigated. Finally, the photosensitivity studies on the CdS and SnS thin films were conducted.

3.1 Zinc sulfide (ZnS) thin films

3.1.1 Experimental details

ZnS (purity 99.999%, Sigma Aldrich) powder was taken as the evaporation source material and was deposited on pre-cleaned glass substrates using a thermal evaporation technique. The deposition chamber was evacuated below 2×10^{-6} Torr using a diffusion pump coupled with a rotary pump. The films were deposited at various substrate temperatures viz., 297K, 373K, and 423K. The thickness of the deposited films was determined by the gravimetric technique and was maintained at ~500 nm. The structural properties of the deposited films were examined by X-ray diffractometer. The surface morphological and elemental composition of the prepared ZnS films were studied by a scanning electron microscope coupled with an EDX detector. The optical properties of the thin films were calculated in the spectral range of 300 - 1600 nm at room temperature using a UV-Vis spectroscopy.

3.1.2 XRD analysis

To study the various structural features of the thermally deposited ZnS thin films, X-ray diffraction (XRD) studies were carried out. Figure 3.1 shows the XRD spectra of the ZnS thin films deposited at various substrate temperatures. It can be seen that all the as-deposited films are crystalline in nature and having a cubic structure with (111)

as preferred oriented peak (*JCPDS card no. 01-077-2100*). Also, it can be noticed that the intensity of the (111) peak increases with increasing substrate temperature. The obtained films were then subjected to annealing at 373K for a duration of 1 hr in order to study the effect of annealing on its structural, morphological and compositional properties. The XRD plots of the annealed ZnS thin films are depicted in figure 3.2. The various structural parameters of the ZnS thin films are tabulated in table 3.1. It can be observed that the crystallite size increases with increasing substrate temperature and also with annealing.

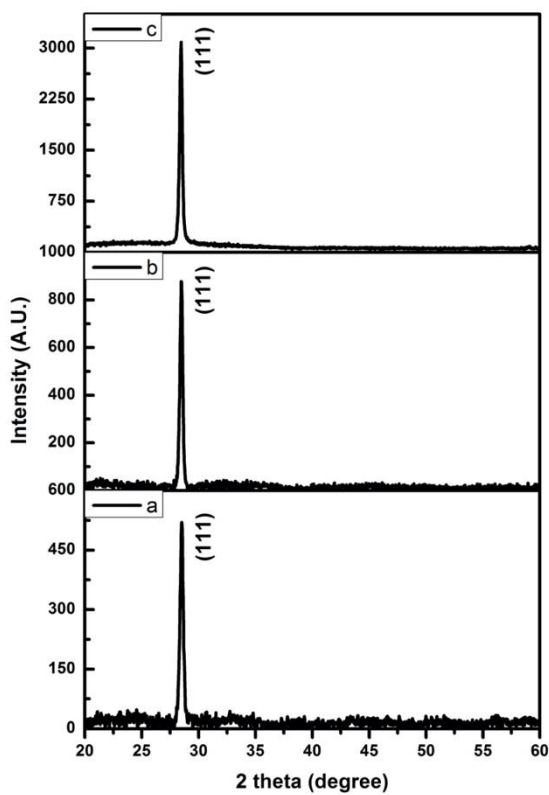


Figure 3.1 XRD image of ZnS thin films deposited at a) 297K, b) 373K, and c) 423K.

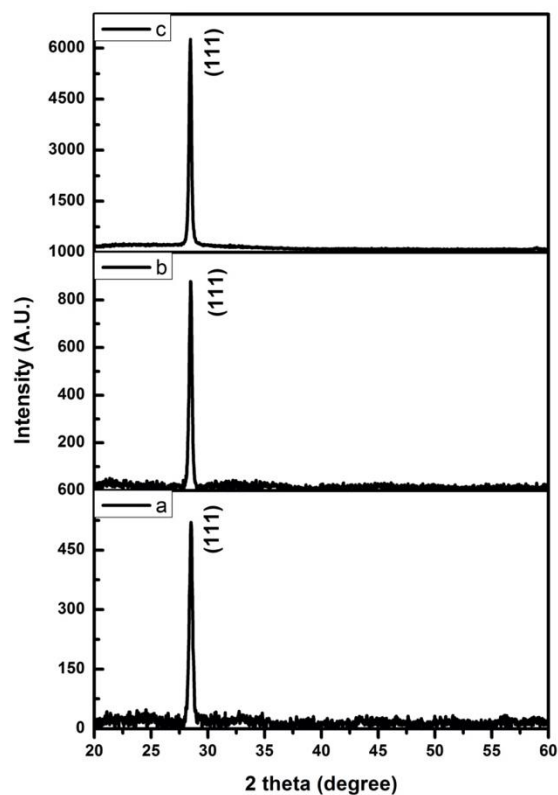


Figure 3.2 XRD image of annealed ZnS thin films deposited at a) 297K, b) 373K, and c) 423K.

3.1.3 Morphological and compositional analysis

The FE-SEM micrographs of the ZnS thin films deposited at different substrate temperature is shown in figure 3.3. It can be observed that the films grown at room temperature and 373K do not contain any features whereas the films deposited at 423K is having granular morphology. All the films are free from any pinholes and cracks.

The EDAX spectra of the film grown at a substrate temperature of 373K is shown in figure 3.4 and the corresponding mapping images of Zn and S are shown in figure 3.5a and figure 3.5b, respectively. From figure 3.5, it can be seen that both the elements i.e., Zn and S are homogeneously distributed across the deposited area. The elemental atomic % of ZnS films is charted in table 3.2. The films grown at room temperature is found to be Zn rich. This can be attributed to the fact that the vapor pressure of Zn is higher than that of S. Therefore, Zn evaporates at a faster rate than S. As the substrate temperature increases, the Zn % decreases from the films. This might be due to the re-evaporation of Zn atoms from the films at a higher substrate temperature. A stoichiometric condition was achieved for the films deposited at a substrate temperature of 373K and annealed at 373K for a duration of 1hr.

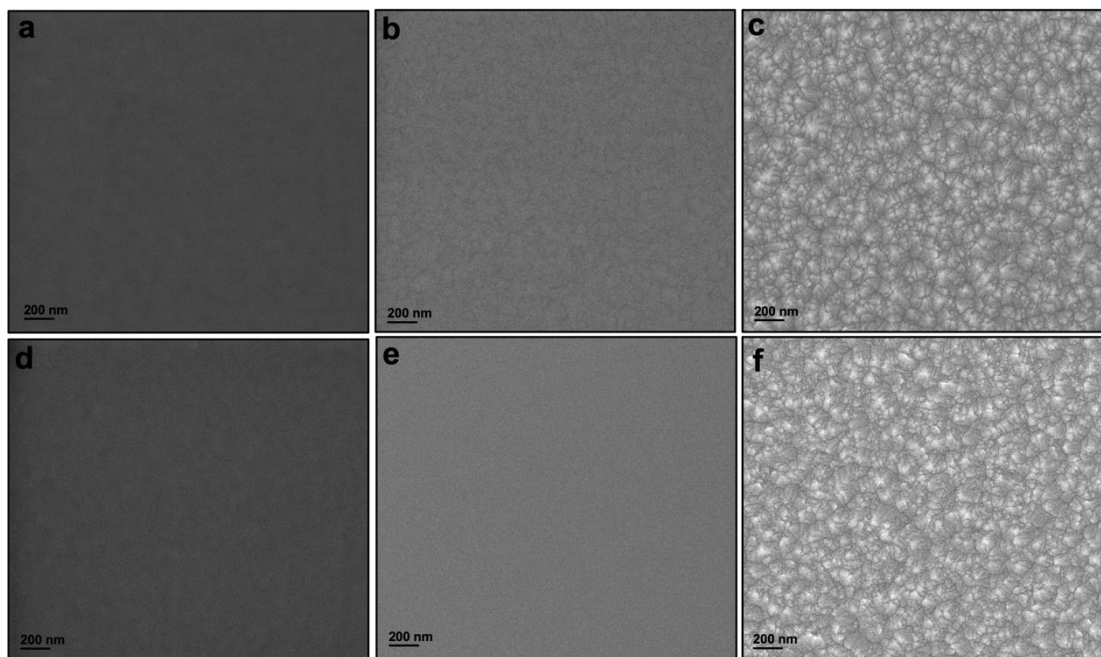


Figure 3.3 SEM images of as-deposited ZnS thin film at substrate temperature of a) 297K, b) 373K, c) 423K and post-annealed ZnS film deposited at d) 297K, e) 373K, f) 423K.

Table 3.1 Structural parameters of ZnS thin films.

Substrate Temperature	2θ (degree)	Crystallite size, D (nm)	d _{hkl} (Å)	Lattice parameter, a (Å)
297K	28.54	24.18	3.125	5.413
Post-Annealed	28.51	24.95	3.128	5.418
373K	28.47	26.42	3.132	5.425
Post-Annealed	28.46	26.50	3.133	5.427
423K	28.45	28.06	3.135	5.429
Post-Annealed	28.44	32.30	3.136	5.431

Table 3.2 Elemental composition of ZnS thin films.

Substrate Temp.	Atomic %			
	As-deposited		Annealed	
	Zn	S	Zn	S
297K	52.17	47.83	52.48	47.52
373K	50.72	49.28	50.37	49.63
423K	48.12	51.88	48.33	51.67

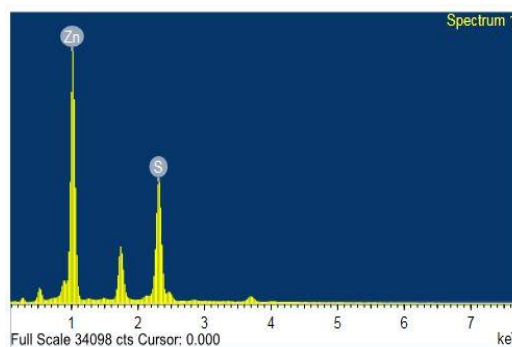


Figure 3.4 EDAX spectra of stoichiometric ZnS thin film.

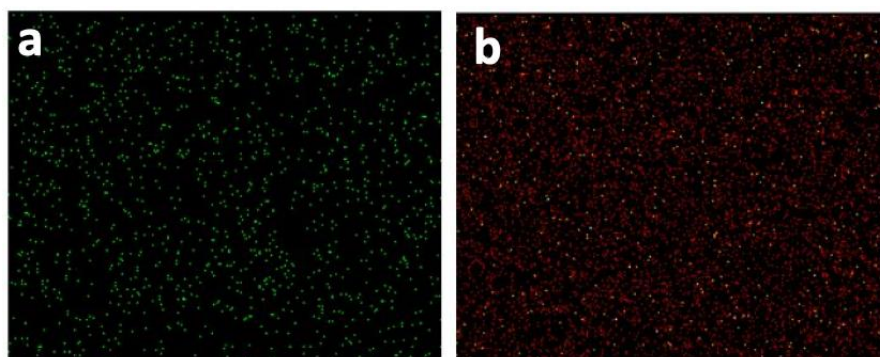


Figure 3.5 Elemental mapping of stoichiometric ZnS thin film (a) Zn and (b) S elements.

3.1.4 Optical studies

The optical absorbance and transmission spectra of the ZnS thin films were obtained from the UV-Vis-NIR spectroscopy in the range 300 - 1600 nm. It can be seen from figure 3.6 that the average transparency of the ZnS thin film deposited at a substrate temperature of 373K is ~85%. The presence of fringes in the transmittance spectra suggests that the film is having a uniform thickness (Benyahia et al. 2015a).

The optical band gaps of the thin films were calculated from the plot of $(\alpha h\nu)^2$ vs photon energy 'hv' by assuming the transition type is allowed direct. The extrapolation of the straight line portion of the curve to the energy axis at $(\alpha h\nu)^2 = 0$ gives the band gap of the material, as shown in figure 3.7. The band gap of the ZnS thin film was found to be 3.51 eV which closely matches the previously reported values (Benyahia et al. 2015a).

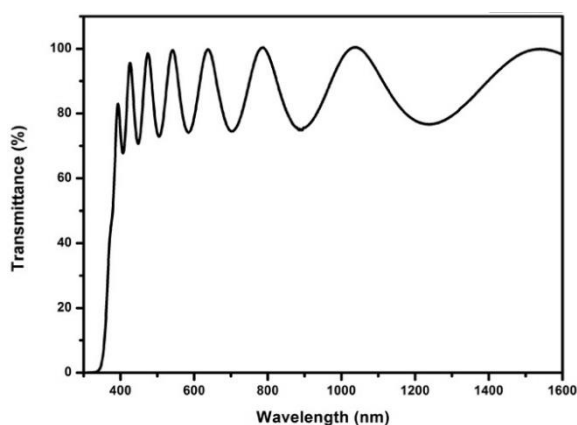


Figure 3.6 Transmission spectra of stoichiometric ZnS thin film.

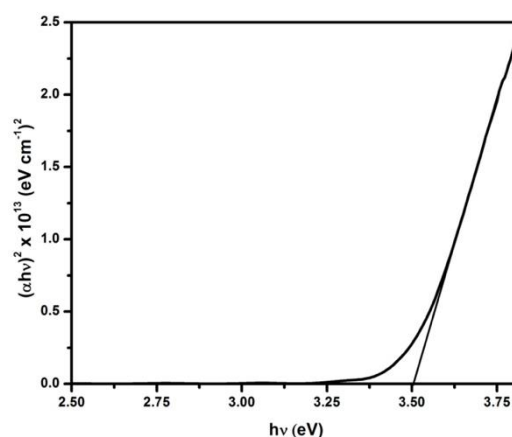


Figure 3.7 Tauc's Plot of stoichiometric ZnS thin film.

3.2 Cadmium sulfide (CdS) thin films

The properties of a thermally grown thin film depend on several parameters such as deposition rate, substrate temperature, film thickness, etc. The thickness of a film plays a crucial role in determining the properties of a thin film (Enríquez 2003). Generally, in the thermal evaporation method, increasing substrate temperature decreases the film thickness due to the re-evaporation of the precursor atoms from the substrate as observed by other groups (Jaber et al. 2012; Tomakin et al. 2011). Therefore, in the present study, CdS thin films of thickness ~450 nm were deposited using a vacuum

thermal evaporation process and the impact of the substrate temperatures upon the structural, morphological, opto-electrical properties of the grown films were examined.

3.2.1 Experimental details

Thermal evaporation method was used to deposit CdS thin films on pre-cleaned glass substrates. CdS (purity 99.999%, Alfa Aesar) powder was used as the evaporation source material. The deposition chamber was evacuated below 2×10^{-6} Torr using a diffusion pump coupled with a rotary pump. The films were deposited at various substrate temperatures viz., 297K, 323K, 373K, and 423K. The thickness of the deposited films was determined by the gravimetric technique and was maintained at ~450 nm for different conditions. The structural properties of the deposited films were examined by X-ray diffractometer. The surface morphological and elemental composition of the prepared CdS films were studied by a scanning electron microscope coupled with an EDX detector. The optical properties of the thin films were calculated in the spectral range of 450 – 750 nm at room temperature using a UV-Vis spectroscopy. For electrical studies, all the films were pre-annealed at 373K for a duration of 1hr in order to obtain a stable photo-electrical response. Silver (Ag) electrodes (1 cm x 1 cm) were deposited on the CdS films using the thermal evaporation method. A Keithley sourcemeter was used for calculating the electrical parameters. Xenon arc lamp was used as a light source for optical studies and a power meter (Nova P/N 7Z01500, Ophir) was used for measuring the light intensity.

3.2.2 Structural studies

X-ray diffraction (XRD) studies were performed on the CdS thin films to gather information about the various structural features present. Figure 3.8 displays the XRD pattern of CdS thin films grown at 297K, 323K, 373K, and 423K substrate temperature, respectively. It can be observed that all films are polycrystalline, matches well with the hexagonal structure of CdS (*JCPDS card no. 00-041-1049*) and are having a predominant peak at $2\theta = 26.4^\circ$ corresponding to (002) plane.

Table 3.3 shows the different parameters calculated for the thermally deposited thin films at different substrate temperatures. The lattice constants ‘a’ and ‘c’ estimated from the diffraction data matches well with the standard values of the hexagonal structure of CdS films. As seen in figure 3.9, both crystallite size and the strength of the (002) predominant peak reduces with increasing substrate temperature and then

increases for a substrate temperature of 423K. Similar observations have been already reported earlier for thermally evaporated CdS thin films having different thicknesses (Jaber et al. 2012).

3.2.3 Morphological studies

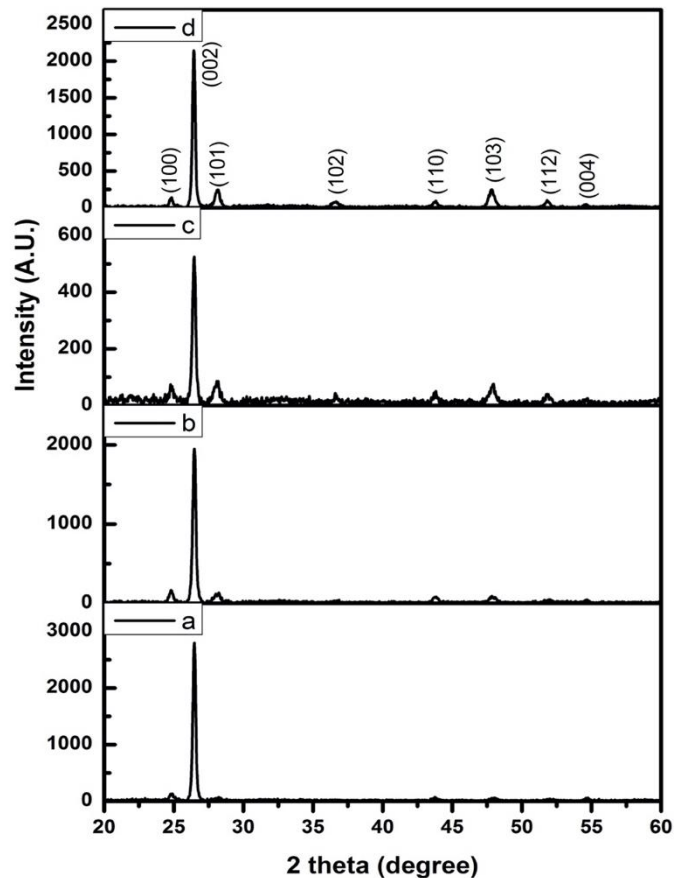


Figure 3.8 XRD images of CdS thin films deposited at a) 297K, b) 323K, c) 373K, and d) 423K.

The microstructural and elemental analysis was carried out using a Scanning Electron Microscope (FE-SEM) accompanying an Energy Dispersive Analysis X-Ray unit (EDAX). The FE-SEM micrographs of thermally deposited films at various substrate temperatures are displayed in figure 3.10. FE-SEM images revealed that the deposited films are pin-hole free and uniform throughout the deposited area with fine grains. It can be observed that the grains re-crystallizes with increasing substrate temperature (figure 3.10b and 3.10c). However, at a substrate temperature of 423K, larger grains

can be observed in figure 3.10d, as suggested by XRD. EDAX spectra confirm the existence of cadmium (Cd) and sulfur (S), as shown in figure 3.11.

The variation in the atomic composition of Cd and S with respect to substrate temperature is charted in table 3.4. A stoichiometric condition of the thermally grown CdS thin film was achieved at a substrate temperature of 373K. It can be seen that the Cd atomic percentage reduces with rising substrate temperature. This is due to the fact that the vapor pressure of Cd is greater than that of S, therefore, at a higher substrate temperature, Cd re-evaporates faster than S from the surface of the film.

Table 3.3 XRD diffraction data of CdS thin films deposited at various conditions.

Substrate Temperature	2 θ (degree)	Plane	Crystallite Size, D (nm)	Interplanar Spacing, d_{hkl} (Å)	Lattice Constant, a (Å)	Lattice Constant, c (Å)
297K	24.84	100	22.96	3.594	4.150	-
	26.44	002	33.04	3.365	-	6.730
323K	24.81	100	24.99	3.586	4.140	-
	26.46	002	29.49	3.366	-	6.732
373K	24.71	100	19.75	3.594	4.150	-
	26.45	002	27.67	3.368	-	6.737
423K	24.81	100	22.96	3.586	4.140	-
	26.43	002	34.23	3.369	-	6.739

Table 3.4 Compositional study of CdS thin films.

Sample	Substrate Temperature	Avg. Grain Size (nm)	Cd (at %)	S (at %)	Cd/S ratio
a	297K	178	52.08	47.92	1.086
b	323K	123	51.21	48.79	1.049
c	373K	105	50.05	49.95	1.002
d	423K	224	47.46	52.54	0.903

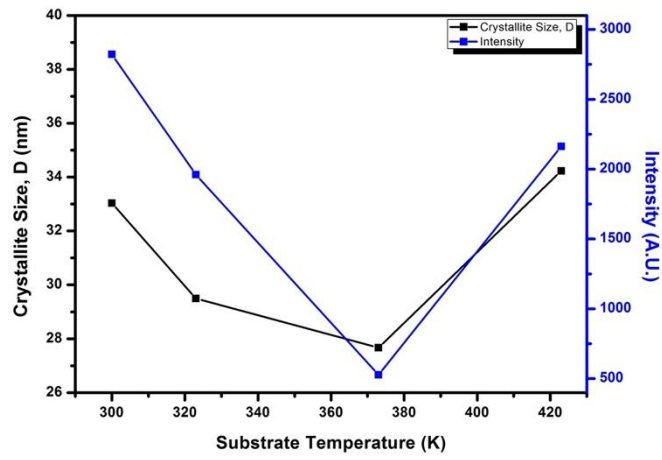


Figure 3.9 Variation of crystallite size and intensity of (002) peak with substrate temperature.

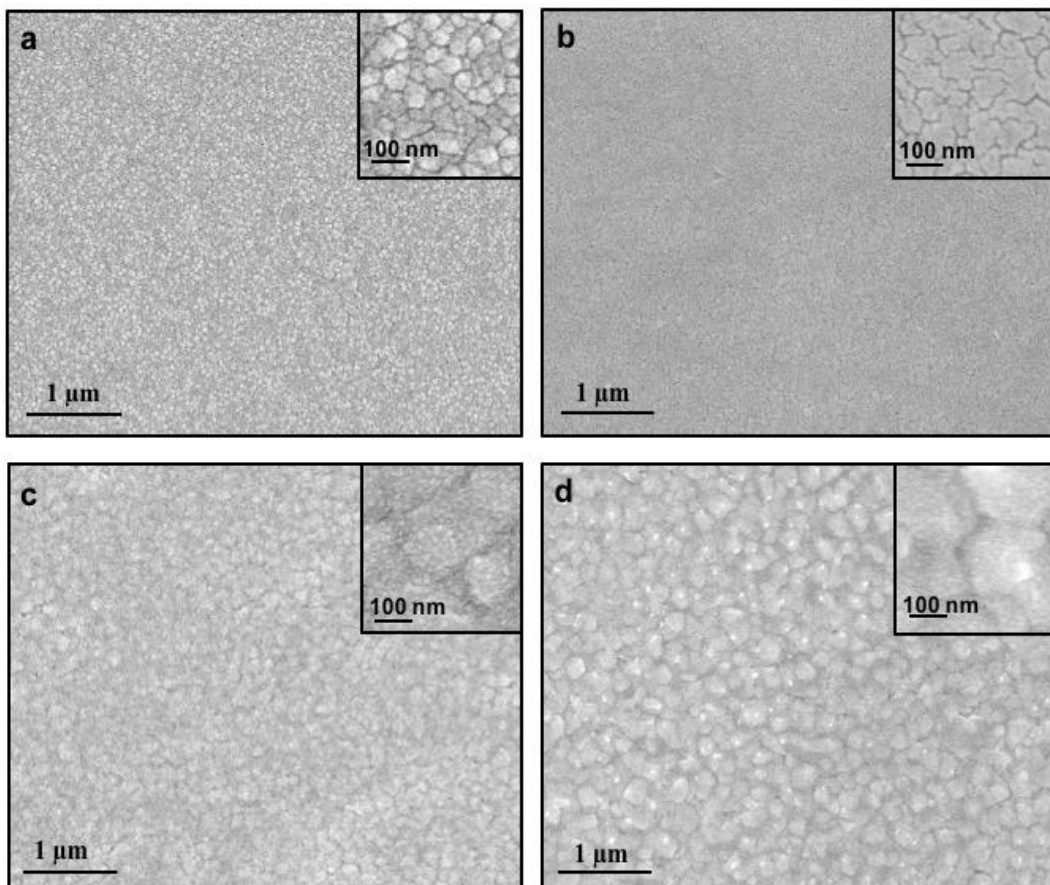


Figure 3.10 FE-SEM pictures of CdS thin films deposited at a) 297K, b) 323K, c) 373K, and d) 423K.

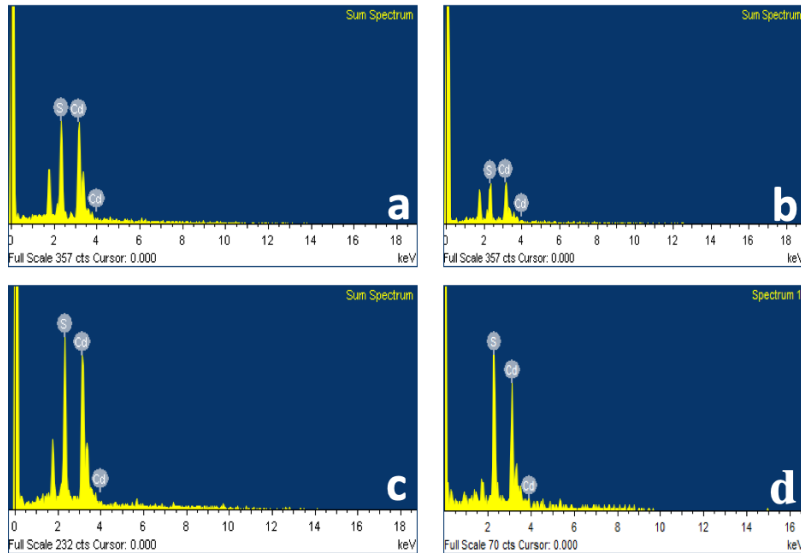


Figure 3.11 EDAX plots of CdS thin films deposited at a) 297K, b) 323K, c) 373K, and d) 423K.

3.2.4 Optical studies

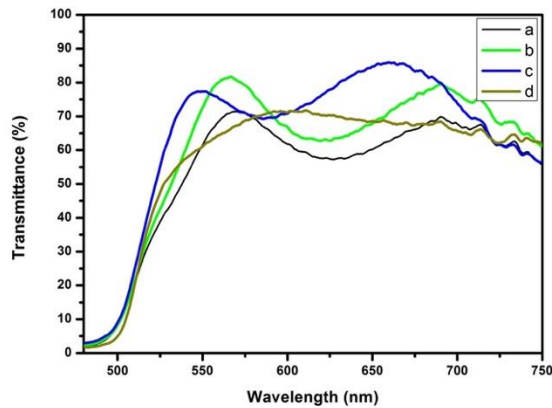


Figure 3.12 Transmittance plot of CdS thin films deposited at a) 297K, b) 323K, c) 373K, and d) 423K.

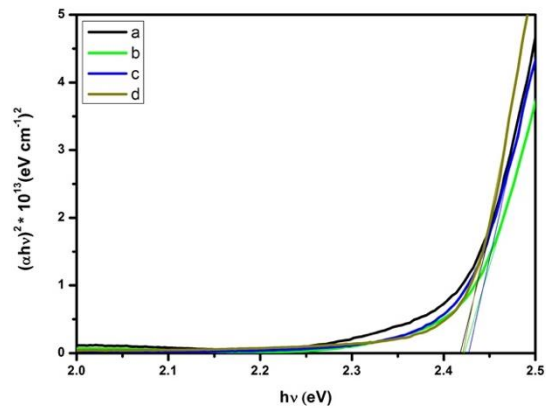


Figure 3.13 Tauc's plot of CdS thin films deposited at a) 297K, b) 323K, c) 373K, and d) 423K.

Optical absorbance and transmittance spectra were carried out on the CdS thin films in the 450 – 750 nm spectral range. The transparency of the grown films was found to be increasing with rising substrate temperature and was found highest for the films grown at a substrate temperature of 373K, as shown in figure 3.12. The optical energy band gaps of the thin films were estimated from Tauc's plot as shown in figure 3.13. The energy band gap of CdS thin films grown at room temperature is calculated to be 2.42 eV which closely matches with previously reported values (Liu et al. 2010).

3.2.5 Opto-electrical properties

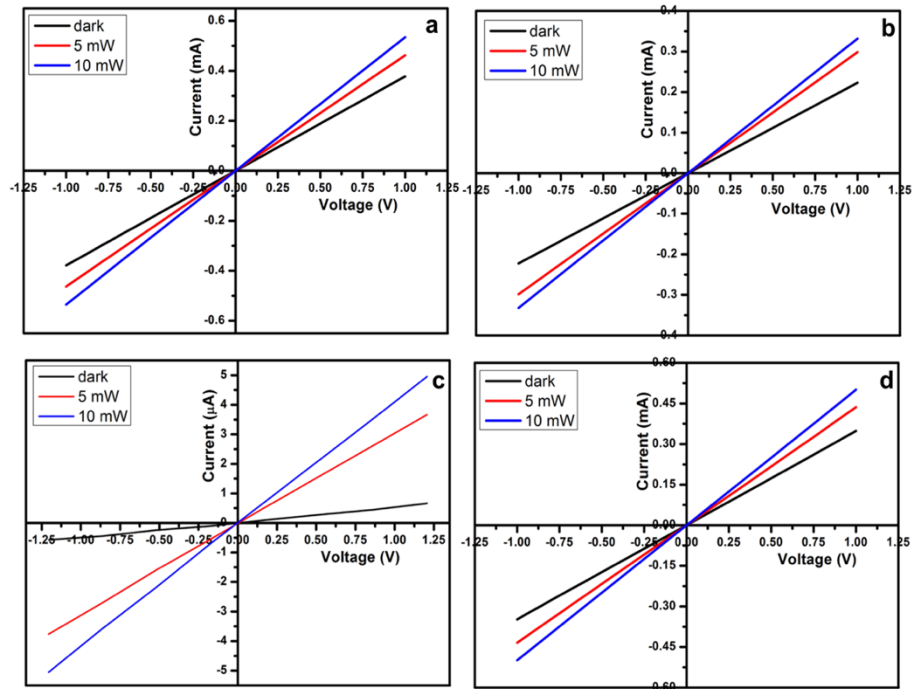


Figure 3.14 IV plots of CdS thin films deposited at a) 297K, b) 323K, c) 373K, and d) 423K.

To analyze the electrical response of CdS thin films, silver (Ag, 99.999 %, Alfa Aesar) metal contact was deposited on the films using a thermal evaporation method. The IV curves shown in figure 3.14 reveal that Ag behaves as an ohmic contact for CdS thin films and also the films are photosensitive. In order to find the majority charge carrier type, the hot probe method was carried out at room temperature and it was seen that all the films are having n-type conductivity (Liu et al. 2010). The variation of photocurrent with response to the light intensity is displayed in figure 3.15. It can be observed that the photocurrent increases as the light intensity increases.

Table 3.5 shows the various optical and electrical parameters calculated for the grown thin films. The photosensitivity was highest for stoichiometric CdS thin films deposited at a substrate temperature of 373K. The existence of a direct optical band gap of ~2.4 eV along with good transparency, crystallinity, and photoconductivity, thereby, makes the deposited CdS thin films a good window layer material for p-type CdTe or CIGS based photovoltaic cells (Lu et al. 2017; Romeo et al. 2004).

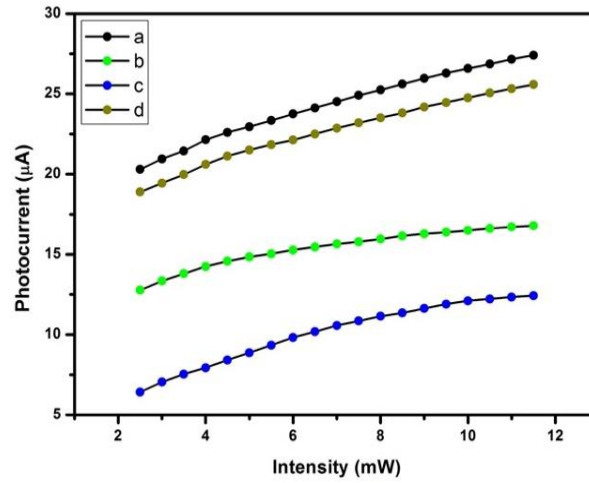


Figure 3.15 Photocurrent vs Intensity plot of CdS thin films a) 297K, b) 323K, c) 373K, and d) 423K.

Table 3.5 Summary of opto-electrical properties of CdS thin films.

Sample	Substrate Temperature	Avg. Transparency (%)	Energy band gap, E_g (eV)	Photo Sensitivity, S
a	297K	64	2.42	0.22
b	323K	72	2.42	0.34
c	373K	79	2.43	1.27
d	423K	69	2.42	0.25

3.3 Tin sulfide (SnS) thin films

The properties of a thermally grown thin film depend on several parameters such as deposition rate, substrate temperature, film thickness, etc. The thickness of a film plays a crucial role in determining the properties of a thin film (Enríquez 2003). Generally, in the thermal evaporation method, increasing substrate temperature decreases the film thickness due to the re-evaporation of the precursor atoms from the substrate as observed by other groups (Jaber et al. 2012; Tomakin et al. 2011). Therefore, in the present report, the thermal evaporation technique was utilized to deposit SnS thin films of thickness ~500 nm on glass substrates and the influence of substrate temperature on the visible light photodetector properties of the SnS thin films have been reported.

3.3.1 Experimental details

Tin sulfide (SnS) thin films were grown on pre-cleaned glass substrates at various substrate temperatures using the thermal evaporation method. SnS pellets (purity 99.5%, Alfa Aesar) were used as a source element and the source to substrate distance was fixed at 13 cm. The deposition chamber was evacuated below 2×10^{-6} Torr using a diffusion pump connected to a rotary pump. Upon deposition, the films were annealed for a duration of 1 hr at 373 K. The thickness of the SnS thin films was calculated by the Gravimetric method and was kept constant at ~500 nm for various substrate temperatures. The Raman spectra of the deposited SnS films were obtained using a LabRAM HR system. The optical properties were measured using a double beam UV–Vis–NIR Spectrophotometer (Shimadzu UV-3600) over the spectral range of 350 – 1350 nm at room temperature. Silver (Ag) (Ag wire, 99.999%, Alfa Aesar) electrodes (1 cm x 1 cm) were thermally evaporated on the surface of the films. The current-voltage properties of the SnS films were calculated using a sourcemeter (Keithley sourcemeter 2400). For the light source, standard Xenon arc lamp was used and in order to measure the light intensity, a power meter (Nova P/N 7Z01500, Ophir) was utilized.

3.3.2 Structural studies

The X-ray diffractograms of the SnS films prepared at various substrate temperatures (297 K, 323 K, 373 K, and 423 K) are shown in figure 3.16. It can be seen that the deposited films are polycrystalline and have a predominant peak at $\sim 2\theta = 31.54^\circ$. This peak can be allocated to (111) plane of the orthorhombic SnS crystal system. The other diffraction peaks observed at 2θ values of 25.99° , 30.53° , 38.96° , and 45.19° can be assigned to (201), (011), (401) and (020) planes respectively.

Table 3.6 displays various structural parameters estimated for the predominant peak corresponding to (111) plane of SnS thin films for various conditions. It can be seen that crystallite size reduces initially as the substrate temperature increases and then later increases for 423 K substrate temperature. This increase in the crystallite size at 423 K can be related to the development of a secondary phase of SnS. Since the peak positions for Sn_2S_3 and SnS in XRD spectra are located at almost the same position i.e., at about 31.25° for (050) oriented Sn_2S_3 (JCPDS no. 30-1377), 31.53° for (111) oriented SnS (JCPDS no. 01-075-2115) and other peaks. In addition, the diffraction peaks corresponding to the Sn_2S_3 phase at 2θ values of 50.16° and 42.96° were also not

detected in this study. Therefore, it is challenging to recognize between the peaks of Sn_2S_3 and SnS by using XRD measurement. Thus, Raman spectroscopic studies were carried out at room temperature to identify the phases of SnS in the resulting thin films.

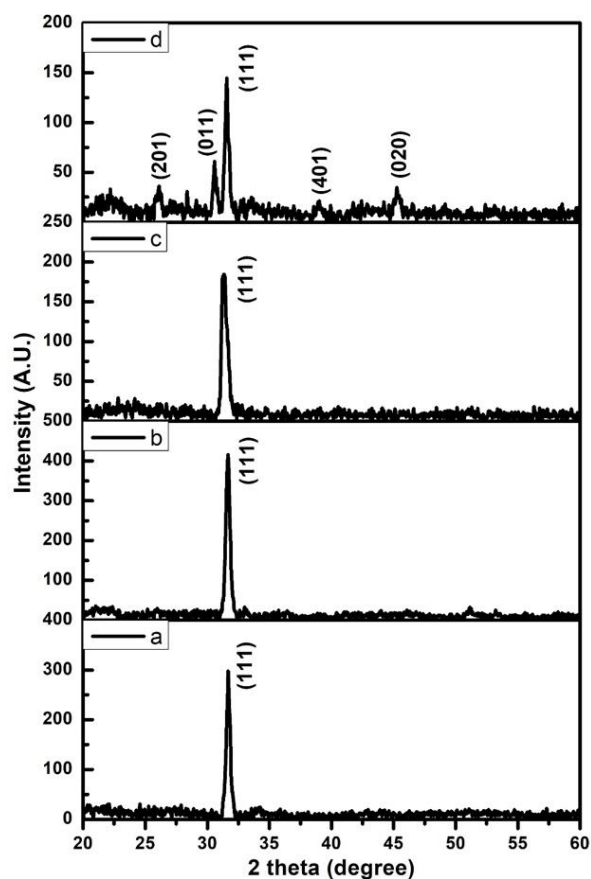


Figure 3.16 XRD diffractograms of SnS thin films deposited at a substrate temperature of a) 297 K, b) 323 K, c) 373 K, and d) 423 K.

Table 3.6 Structural parameters of thermally deposited SnS thin films.

Sample	Substrate Temperature (K)	2θ (degree)	Crystallite size, D (nm)	Interplanar Spacing, d_{hkl} (nm)
a	297	31.66	20.95	0.282
b	323	31.63	19.79	0.283
c	373	31.26	15.99	0.285
d	423	31.53	21.57	0.283

3.3.3 Raman studies

Figure 3.17 depicts the Raman scattering spectra of the films deposited at various substrate temperatures. All Raman spectra were gathered using a low power laser. The peaks at 93.08 and 225 cm^{-1} correspond to the SnS phase whereas the peak at 308 cm^{-1} corresponds to the Sn_2S_3 phase. It can be observed that the films grown at 323 K does not contain any peaks of Sn_2S_3 phase, thereby, demonstrating the formation of a single-phase SnS films. However, for the film deposited at 423 K, the peaks from both SnS and Sn_2S_3 phases were observed.

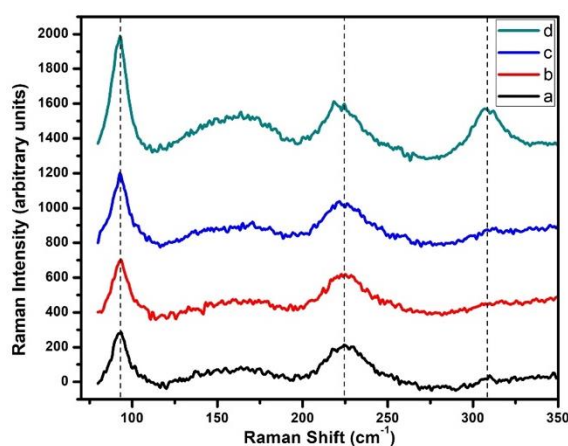


Figure 3.17 Raman spectra of SnS thin films deposited at a substrate temperature of a) 297 K, b) 323 K, c) 373 K, and d) 423 K.

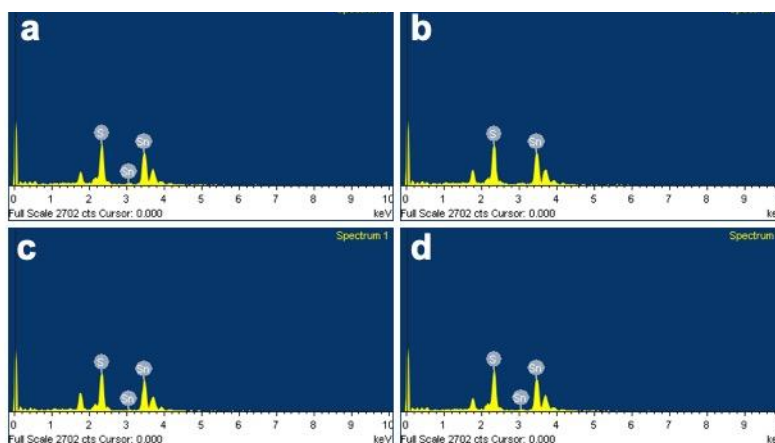


Figure 3.18 EDAX spectra of SnS thin films deposited at a substrate temperature of a) 297 K, b) 323 K, c) 373 K, and d) 423 K.

3.3.4 Morphological and compositional analysis

In order to provide additional confirmation of the phase identities of SnS films, EDAX analysis was performed. EDAX spectra verify the presence of tin (Sn) and sulfur (S) elements, as indicated in figure 3.18. The change in the atomic % of the films along with the Sn : S ratio as a function of substrate temperature is charted in table 3.6. The obtained data is in good agreement with XRD and Raman studies. A nearly-stoichiometric SnS film was attained at 323 K substrate temperature. From table 3.6, it can also be observed that with increasing substrate temperature, Sn atomic percentage decreases. This might be due to dissimilarity in vapor pressure of S and Sn since the vapor pressure of Sn is higher than that of S. As a result, Sn re-evaporates faster from the substrate as the substrate temperature increases.

Table 3.7 Composition, energy bandgap and activation energies of SnS thin films deposited at various substrate temperatures.

Substrate Temperature (K)	Sn (at%)	S (at%)	Sn : S ratio	Energy band gap, E_g (eV)	Activation Energy, E_a (eV)
297	50.93	49.07	1 : 0.96	1.576	0.806
323	49.72	50.28	1 : 1.01	1.539	0.727
373	47.98	52.02	1 : 1.08	1.463	0.642
423	46.11	53.89	1 : 1.17	1.429	0.397

The FE-SEM pictures of thermally grown SnS thin films at different substrate temperatures are shown in figure 3.19. It can be observed from the FE-SEM pictures that all the films do not contain any pin-holes or cracks and the films are uniform throughout the deposited area. The films grown at room temperature consists of granular structure. As the substrate temperature increases, the morphology of the film changes to a flake-type structure. Therefore, it can also be noted that substrate temperature has a considerable amount of effect on the morphology of the films. This might be due to different sulfur content and density of various tin sulfides such as SnS and Sn₂S₃ as revealed from Raman and EDAX studies for the deposited SnS thin films.

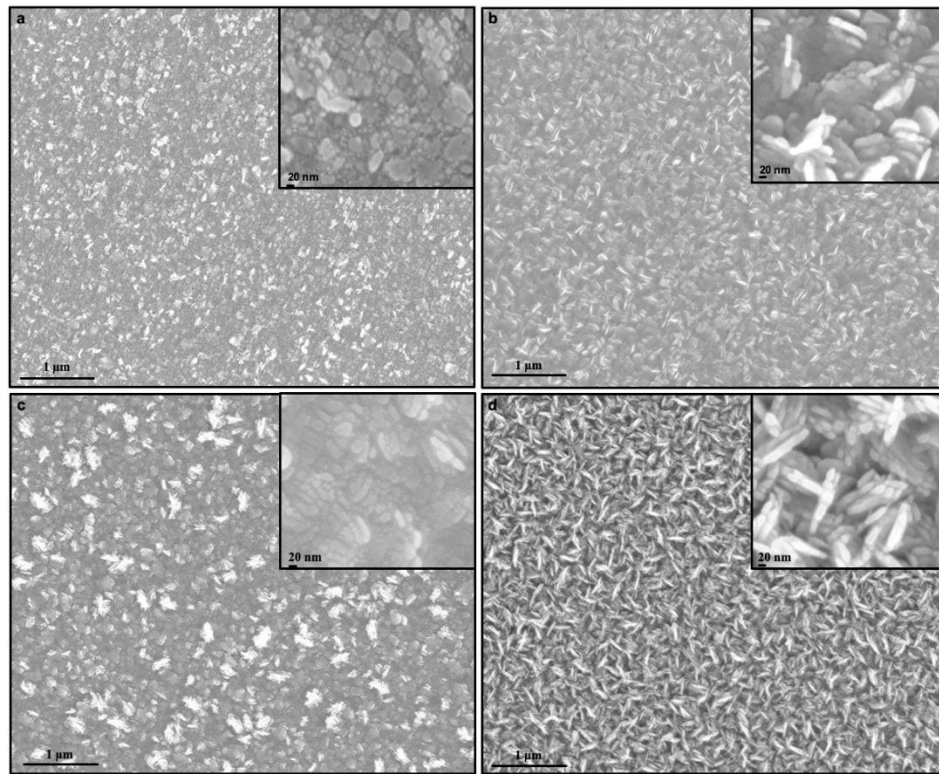


Figure 3.19 FE-SEM images of SnS thin films deposited at a substrate temperature of a) 297 K, b) 323 K, c) 373 K, and d) 423 K.

3.3.5 Optical studies

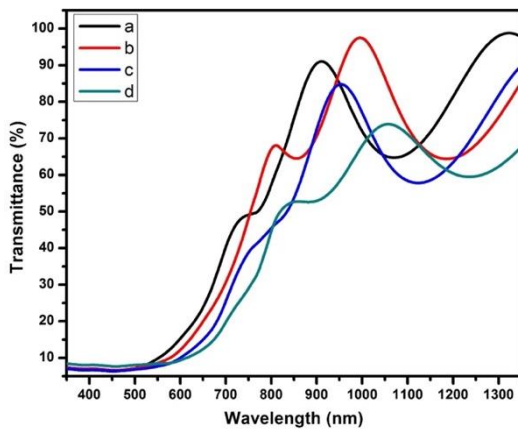


Figure 3.20 Transmittance spectra of SnS thin films deposited at a) 297 K, b) 323 K, c) 373 K, and d) 423 K.

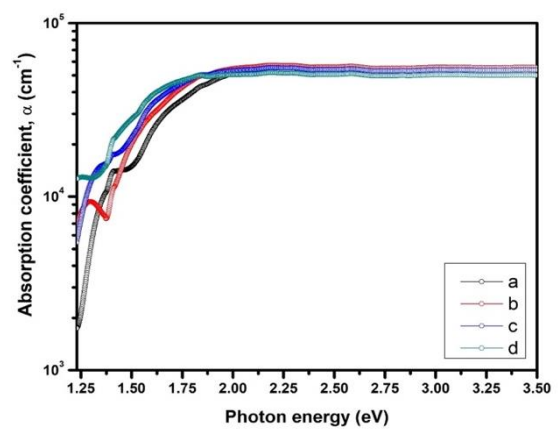


Figure 3.21 Plot of α Vs $h\nu$ of SnS thin films deposited at a) 297 K, b) 323 K, c) 373 K, and d) 423 K.

The optical transmittance determined at room temperature in the range of 350 - 1350 nm for the SnS thin films prepared under different substrate temperatures is shown in figure 3.20. It can be seen that the transparency of the grown films is maximum for the films grown at 323 K substrate temperature.

It can be seen that all the films are having a very good absorption coefficient of $\sim 10^5 \text{ cm}^{-1}$. This suggests that the grown SnS films can be used as a potential candidate for the absorber layer in photovoltaic applications (Andrade-Arvizu et al. 2015; Koteeswara Reddy et al. 2015; Zhao et al. 2016).

The plot of $(\alpha h\nu)^2$ vs photon energy ($h\nu$) was utilized to calculate the optical bandgaps of the SnS thin films. The extrapolation of the linear portion of the plot to the intercept with the energy axis at $(\alpha h\nu)^2 = 0$ provides the optical bandgap of the material, as displayed in figure 3.21. In the current study, $n = 2$ does not show a linear fit whereas $n = 1/2$ shows a linear fit of Tauc's plot. This confirms the presence of direct bandgap transition for the thermally grown SnS thin films. SnS films have been reported having bandgap in a wide range from 0.9 eV to 1.8 eV (Sns et al. 2013). This can be correlated with the variation in the composition of the film and the formation of an additional Sn_2S_3 phase. This is in accordance with Raman and EDAX analysis.

3.3.6 Opto-electrical properties

To study the electrical properties of SnS films, silver (Ag) contacts were deposited onto the films with an active area of 0.1 cm^2 using the thermal evaporation method. At equilibrium state, a depletion region is produced between the SnS–Ag interface consisting of -ve charge on the SnS area and +ve charge towards the Ag area. When the light of particular energy is illuminated on the semiconductor-metal interface, electron-hole pairs are produced. The photo-generated holes then move to the SnS side and electrons to the positively charged Ag side. This separation of electron-holes leads to the formation of photovoltage.

The current-voltage characteristics curves of the SnS films displayed in figure 3.23 shows that silver forms an ohmic contact. It was observed that all the films show p-type conductivity (Chalapathi et al. 2016) from the hot probe technique.

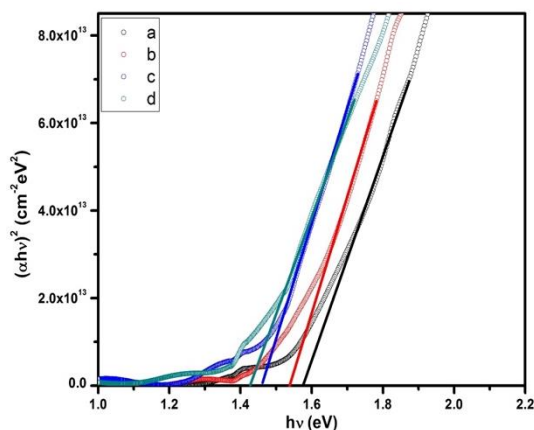


Figure 3.22 Tauc's plot of SnS thin films deposited at a) 297 K, b) 323 K, c) 373 K, and d) 423 K.

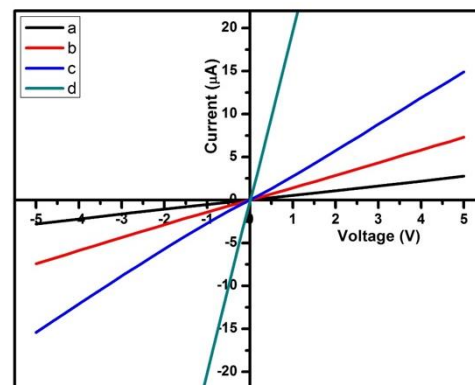


Figure 3.23 Current Vs Voltage plot of SnS thin films deposited at a) 297 K, b) 323 K, c) 373 K, and d) 323 K.

The change of $\ln(R)$ as a role of $1/T$ of the thermally deposited SnS thin films is shown in figure 3.24. The plot displays a single linear region for all the films. The increase in the resistance values with the decrease in temperature verifies the semiconducting nature of the SnS thin films.

Figure 3.26 illustrates the photoconductivity Vs time response of the SnS thin films prepared at a substrate temperature of 297 K to 373 K. It was recorded under an illumination power of 10 mW/cm^2 in the following sequences: 10 secs under illumination and 30 secs in dark. The plot shows four cycles of highly reproducible ON/OFF photocurrent demonstrating the stability of the films and thereby, showing that these films can be successfully employed for photosensor application. The measured photosensitivity and photo responsivity values are tabulated in table 3.8. The films deposited at a substrate temperature of 323 K displays the highest photosensitivity. The recovery time ' τ_d ' is "the time interval for the response to decay from 90 to 10 % of its peak value" and the response time ' τ_r ' is "the time interval required for the response to rise from 10 to 90 % of its maximum value" (Zeng et al. 2013a). The response and recovery time of SnS thin films deposited at 323 K for one ON/OFF cycle is shown in figure 3.25. The measured photocurrent response time and recovery time of the SnS thin films (substrate temperature $\leq 373 \text{ K}$) is tabulated in table 3.8.

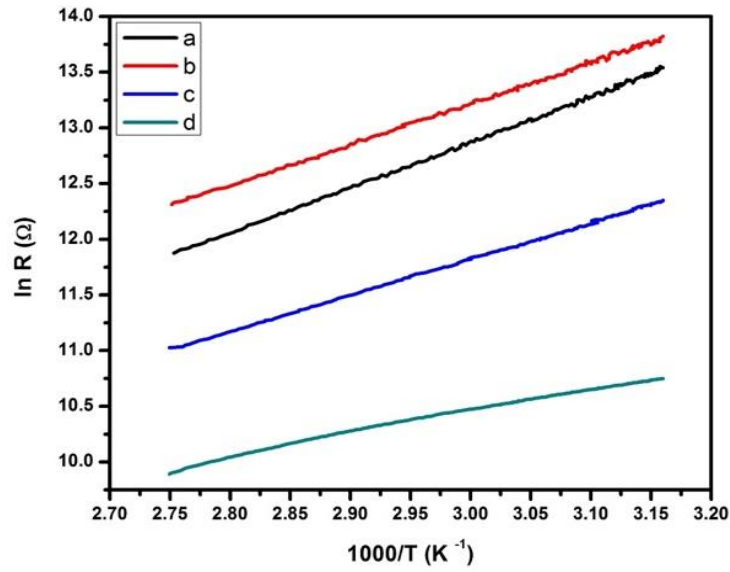


Figure 3.24 Variation of $\ln R$ with $1000/T$ of SnS thin films deposited at a) 297 K, b) 323 K, c) 373 K, and d) 423 K.

Table 3.8 Photo-response parameters of SnS thin films deposited at a substrate temperature of a) 297 K, b) 323 K, and c) 373 K.

Sam ple	$\sigma_L (\Omega \text{ m})^{-1}$	$\sigma_D (\Omega \text{ m})^{-1}$	Sensitivity	Responsivity (A W^{-1})	Response Time, τ_r (Sec)	Recovery Time, τ_d (Sec)
a	1.99×10^{-8}	1.22×10^{-8}	0.63	1.56	2.49	2.79
b	0.57×10^{-8}	0.05×10^{-8}	10.93	0.99	2.48	2.86
c	5.73×10^{-8}	4.78×10^{-8}	0.19	1.98	4.03	6.87

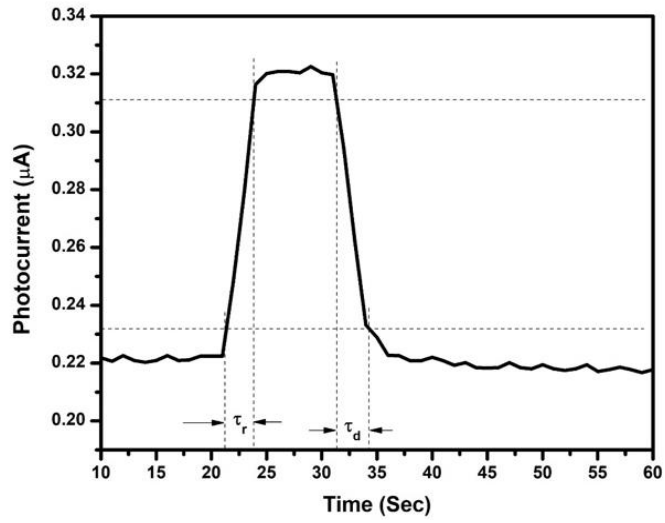


Figure 3.25 Response and recovery time of SnS thin films deposited at a substrate temperature of 323 K.

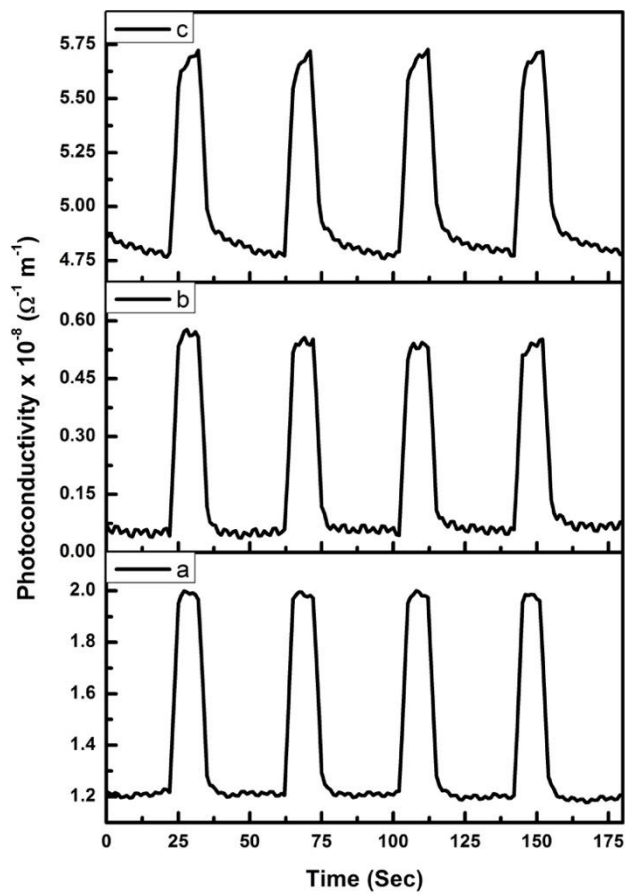


Figure 3.26 Photoconductivity Vs Time response of SnS thin films deposited at a substrate temperature of a) 297 K, b) 323 K, and c) 373 K.

CHAPTER – 4

CHAPTER 4

INVESTIGATIONS ON TERNARY SULFIDE THIN FILMS

Overview:

This chapter explains the method for obtaining the ternary compound thin films using the thermal evaporation method. The films were then subjected to various characterizations such as structural, morphological, compositional, optical and electrical properties. Herein, the results obtained depict the tunable properties of the films which depend on the composition of the films. Among the grown ternary compounds, $\text{Cu}_x(\text{ZnS})_{1-x}$ thin films displayed exceptional p-type transparent conductivity whereas, the $\text{Zn}_x\text{Cd}_{1-x}\text{S}$ and $\text{Zn}_x\text{Sn}_{1-x}\text{S}$ thin films showed outstanding photosensitivity.

4.1 $\text{Cu}_x(\text{ZnS})_{1-x}$ thin films

In recent years, transparent conducting materials (TCMs) are becoming important in opto-electronic applications such as light emitting diodes, photovoltaics, organic electronics, etc. There are many n-type wide band gap materials such as ZnS, ZnO, SnO₂, etc. which are widely used for transparent electronics. There are relatively fewer reports on the successful fabrication of p-type transparent conducting films. In the present study, p-type transparent $\text{Cu}_x(\text{ZnS})_{1-x}$ thin films are deposited on pre-cleaned glass substrates by thermal evaporation technique. The Cu concentration in $\text{Cu}_x(\text{ZnS})_{1-x}$ thin films has been varied and its effect on thin film properties has been studied in detail.

4.1.1 Experimental details

For the preparation of $\text{Cu}_x(\text{ZnS})_{1-x}$ ($x = 0, 0.01, 0.02, 0.03, 0.05, 0.10,$ and 0.25) thin films, a mixture of Cu (purity 99.999 %, Alfa Aesar) and ZnS (purity 99.995 %, Sigma Aldrich) was deposited on clean glass substrates by the thermal evaporation technique at a pressure of $\sim 2 \times 10^{-6}$ Torr. The substrate temperature was maintained at 373 K and post-deposition annealing was carried out at the same temperature for 1 hr. The thickness of the deposited films was determined by the gravimetric method and was

maintained at ~500 nm for different compositions. The structural characterization of the films was carried out by an X-ray diffractometer (Rigaku MiniFlex 600) using CuK α radiation with a wavelength of 1.5418 Å. The surface morphology and elemental composition of the grown thin films were analyzed using a scanning electron microscope (Carl Zeiss FE-SEM) with a linked electron dispersion X-ray (EDX) detector which was operating at an accelerating voltage of 5 kV. The optical absorbance and transmittance spectra of the prepared thin films were measured at room temperature in the spectral range 300 – 800 nm using spectrophotometer (SpectraPro 2300i). The electrical characteristics of the thin films were studied using a sourcemeter (Keithley sourcemeter 2400) and a multimeter (Keithley multimeter 2002) with indium (In) as an ohmic contact.

4.1.2 Structural studies

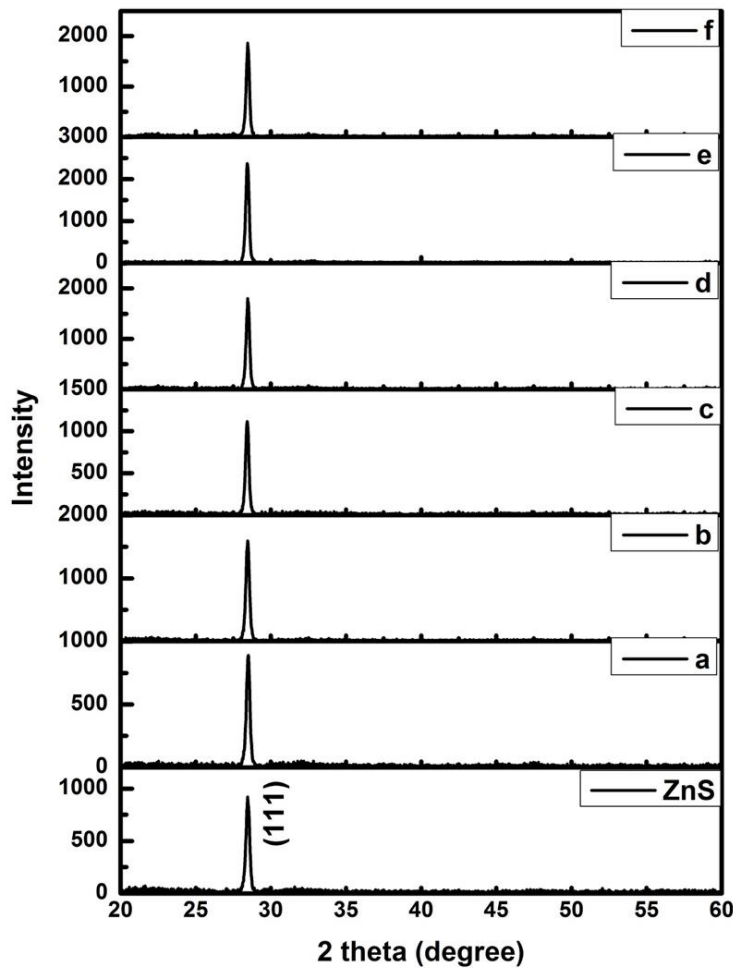


Figure 4.1 XRD patterns of $\text{Cu}_x(\text{ZnS})_{1-x}$ thin films: a) $x = 0.01$, b) $x = 0.02$, c) $x = 0.03$, d) $x = 0.05$, e) $x = 0.10$, and f) $x = 0.25$.

X-ray diffraction (XRD) studies were carried out on the deposited thin films and the diffraction patterns were analyzed to gather information about its various structural features. The X-ray diffraction (XRD) patterns of $\text{Cu}_x(\text{ZnS})_{1-x}$ ($x = 0, 0.01, 0.02, 0.03, 0.05, 0.10$ and 0.25) thin films is shown in figure 4.1. According to the XRD pattern, the reflection (111) at 28.46° corresponds to the cubic structure (zinc blende) of the undoped ZnS thin film (JCPDS card no. 01-077-2100). No significant shift in the (111) peak position was observed even at higher Cu concentration. This might be due to the reason that the ionic radii of copper in the +1 valence state and zinc in the +2 valence state with IV coordination are both 74 pm (Diamond et al. 2012; Shannon 1976). Moreover, no additional peak(s) corresponding to any phase of Cu or Zn was observed, as previously reported (Diamond et al. 2012). The obtained ‘d’ values were found to be in a good agreement with the standard JCPDS data, shown in table 4.1.

Table 4.1 X-ray diffraction data of $\text{Cu}_x(\text{ZnS})_{1-x}$ thin films.

Sample	2 θ	Inter planar spacing, d (Å)	Crystallite size, D (nm)	Lattice parameter, a (Å)
$\text{Cu}_{0.00}(\text{ZnS})_{1.00}$	28.46°	3.133	26.52	5.427
$\text{Cu}_{0.01}(\text{ZnS})_{0.99}$	28.47°	3.132	27.63	5.426
$\text{Cu}_{0.02}(\text{ZnS})_{0.98}$	28.44°	3.136	27.63	5.432
$\text{Cu}_{0.03}(\text{ZnS})_{0.97}$	28.42°	3.138	30.05	5.436
$\text{Cu}_{0.05}(\text{ZnS})_{0.95}$	28.46°	3.133	29.54	5.427
$\text{Cu}_{0.10}(\text{ZnS})_{0.90}$	28.43°	3.137	31.60	5.433
$\text{Cu}_{0.25}(\text{ZnS})_{0.75}$	28.44°	3.136	32.82	5.432

4.1.3 Morphological studies

The SEM images of the $\text{Cu}_x(\text{ZnS})_{1-x}$ films are shown in figure 4.2. A uniform, homogeneous and pin-hole free surface throughout the deposited area can be observed for the films deposited at various Cu concentration. EDAX spectra confirm the presence of Cu, Zn, and S in the deposited thin films as shown in figure 4.3a. Figure 4.3b – 4.3d shows the elemental mapping images of Cu, Zn, and S on the grown film. It can be

observed that all the elements (Cu, Zn, and S) are homogeneously distributed throughout the film. The atomic compositions of various films are tabulated in table 4.2.

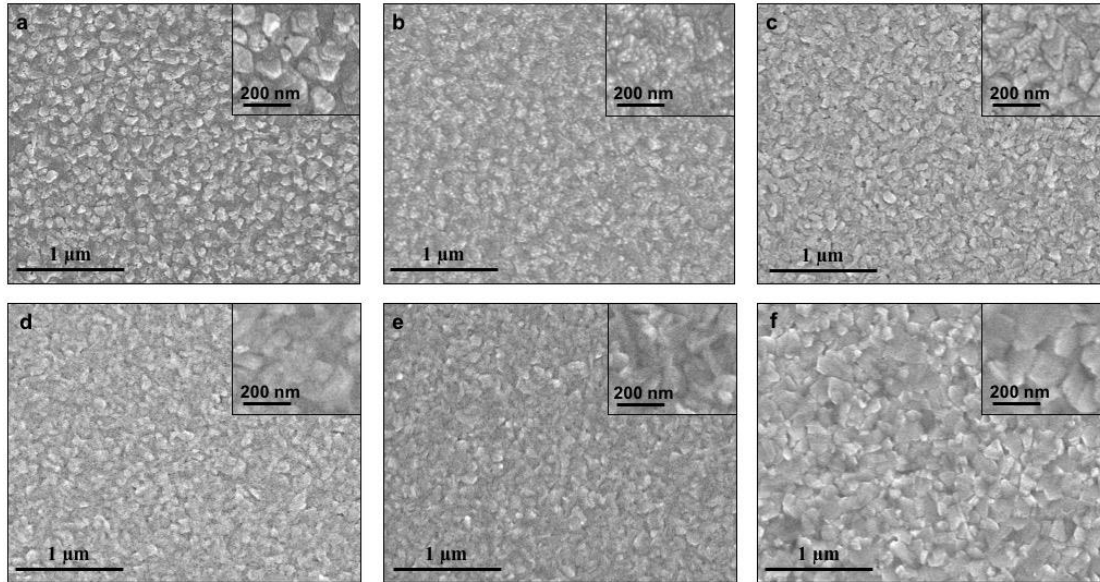


Figure 4.2 FE-SEM images of $\text{Cu}_x(\text{ZnS})_{1-x}$ thin films of various Cu concentration: a) $x = 0.01$, b) $x = 0.02$, c) $x = 0.03$, d) $x = 0.05$, e) $x = 0.10$, and f) $x = 0.25$.

Table 4.2 Compositional analysis of $\text{Cu}_x(\text{ZnS})_{1-x}$ ($x = 0, 0.01, 0.02, 0.03, 0.05, 0.10$, and 0.25) thin films.

Sample	Cu (at%)	Zn (at%)	S (at%)
$\text{Cu}_{0.00}(\text{ZnS})_{1.00}$	0	52.44	47.56
$\text{Cu}_{0.01}(\text{ZnS})_{0.99}$	1.54	49.14	49.31
$\text{Cu}_{0.02}(\text{ZnS})_{0.98}$	1.97	49.37	48.66
$\text{Cu}_{0.03}(\text{ZnS})_{0.97}$	3.08	47.60	49.33
$\text{Cu}_{0.05}(\text{ZnS})_{0.95}$	6.19	46.83	46.98
$\text{Cu}_{0.10}(\text{ZnS})_{0.90}$	10.64	42.88	46.48
$\text{Cu}_{0.25}(\text{ZnS})_{0.75}$	24.48	32.51	43.01

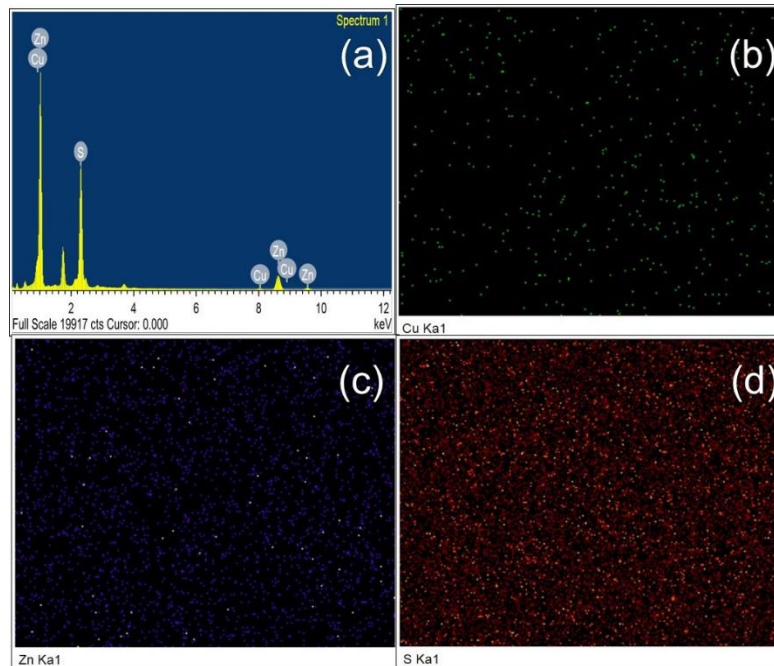


Figure 4.3 EDAX analysis of $\text{Cu}_{0.03}(\text{ZnS})_{0.70}$ thin films (a) EDAX Spectra; Elemental mapping of (b) Cu, (c) Zn, and (d) S.

4.1.4 Optical properties

The optical absorbance and transmission spectra of the films were obtained from the UV-Vis-NIR spectroscopy in the range 300 - 800 nm. The transparency of the films was found to reduce monotonically with increasing Cu concentration as shown in figure 4.4 which may be due to the decrease in the optical band gap at higher Cu concentration. It was also observed that the average optical transparency of undoped ZnS was approximately 85% whereas the films at $x = 0.01, 0.02, 0.03, 0.05, 0.10,$ and 0.25 have average transparencies of 80%, 75%, 73%, 60%, 55%, and 50% respectively. The presence of fringes in the transmittance spectra suggests that the films are having a uniform thickness (Benyahia et al. 2015a).

The optical band gaps of the thin films were calculated from the plot of $(\alpha h\nu)^2$ vs photon energy 'hv' by assuming a direct allowed transition type. The extrapolation of the straight line portion of the curve to the energy axis at $(\alpha h\nu)^2 = 0$ gives the band gap of the material, as shown in figure 4.5. The band gap of the $\text{Cu}_x(\text{ZnS})_{1-x}$ thin films was found to be decreasing with increasing Cu concentration due to the incorporation of Cu

in the ZnS matrix. The band gap of the ZnS thin film was found to be 3.48 eV which closely matches with the previously reported values (Benyahia et al. 2015a).

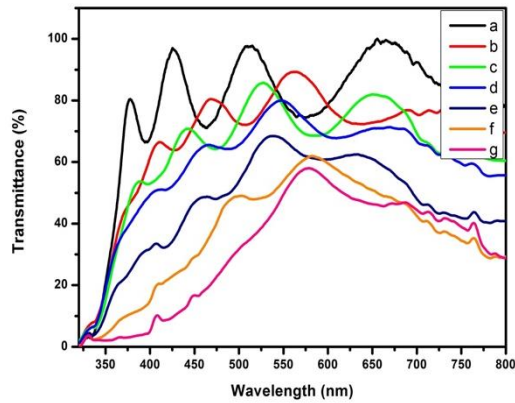


Figure 4.4 Transmittance vs wavelength plot of $\text{Cu}_x(\text{ZnS})_{1-x}$ thin films: x = a) 0, b) 0.01, c) 0.02, d) 0.03, e) 0.05, f) 0.10, and g) 0.25.

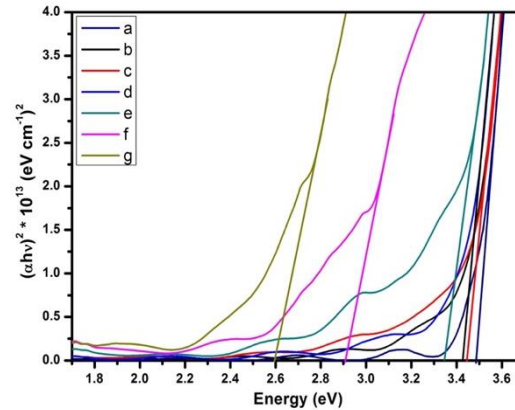


Figure 4.5 Tauc's plot of $\text{Cu}_x(\text{ZnS})_{1-x}$ thin films: x = a) 0, b) 0.01, c) 0.02, d) 0.03, e) 0.05, f) 0.10, and g) 0.25.

4.1.5 Electrical properties

To study the electrical characteristics of the $\text{Cu}_x(\text{ZnS})_{1-x}$ thin films, indium metal contact was deposited on the surface of the films using the thermal evaporation technique. The I-V plots shown in figure 4.6 confirm that indium behaves as an ohmic contact for the $\text{Cu}_x(\text{ZnS})_{1-x}$ thin films. The resistance of the films was calculated from the slope of the I-V plot. Hot-probe study was carried out to determine the majority charge carrier in the films and it was found that all the films have p-type conductivity (Ichimura and Maeda 2015). Further, silver (Ag) was deposited on undoped ZnS thin films having the same active area as In contact and it was found that the resistance of the undoped ZnS was too high and could not be measured with the Keithley 2002 multimeter.

From table 4.3, it can be observed that the $\text{Cu}_x(\text{ZnS})_{1-x}$ thin films are highly conducting in nature and the conductivity of the films increases as the Cu concentration increases. It is noteworthy that the conductivity of the films reported here for lower Cu concentration is much higher than the reported values (Diamond et al. 2012; Woods-Robinson et al. 2016).

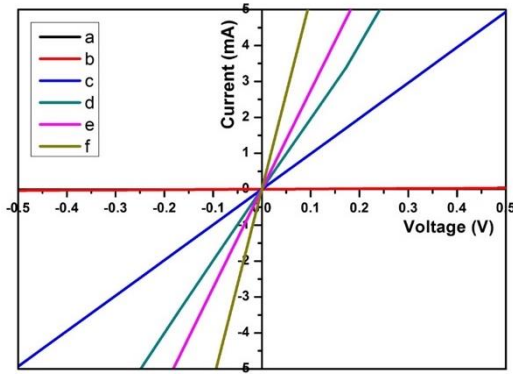


Figure 4.6 IV characteristics of $\text{Cu}_x(\text{ZnS})_{1-x}$ thin films: x = a) 0, b) 0.01, c) 0.02, d) 0.03, e) 0.05, f) 0.10, and g) 0.25.

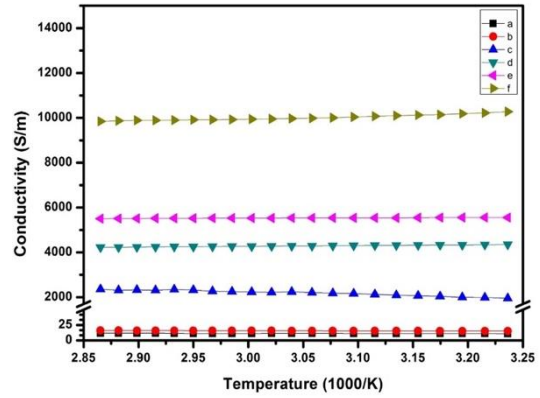


Figure 4.7 Conductivity vs $1000/T$ plot of $\text{Cu}_x(\text{ZnS})_{1-x}$ thin films: x = a) 0, b) 0.01, c) 0.02, d) 0.03, e) 0.05, f) 0.10, and g) 0.25.

Table 4.3 Summary of electrical and optical properties of $\text{Cu}_x(\text{ZnS})_{1-x}$ thin films.

Sample	Conductivity (S/m) $\times 10^3$	Transmittance %	Bandgap (eV)
$\text{Cu}_{0.00}(\text{ZnS})_{1.00}$	--	85	3.48
$\text{Cu}_{0.01}(\text{ZnS})_{0.99}$	00.011	80	3.43
$\text{Cu}_{0.02}(\text{ZnS})_{0.98}$	00.015	75	3.43
$\text{Cu}_{0.03}(\text{ZnS})_{0.97}$	01.912	73	3.40
$\text{Cu}_{0.05}(\text{ZnS})_{0.95}$	04.327	60	3.34
$\text{Cu}_{0.10}(\text{ZnS})_{0.90}$	05.554	55	2.92
$\text{Cu}_{0.25}(\text{ZnS})_{0.75}$	11.642	50	2.60

Figure 4.7 shows the variation of conductivity with temperature in the range 308K to 348K. It is observed that the conductivity is almost independent of temperature which confirms degenerate hole conduction within the valence band (Xu et al. 2016). This type of band conduction has been reported on some other p-type metallic conductors, such as $\text{Bi}_2\text{Sr}_2\text{Co}_2\text{O}_y$ (Wei et al. 2014).

4.2 Zn_xCd_{1-x}S thin films

In the present study, an effort has been made to deposit high quality Zn_xCd_{1-x}S (x=0, 0.15, 0.30, 0.45, 0.70, 0.85, 1) thin films using a thermal evaporation system. By altering the composition of the Zn_xCd_{1-x}S thin films, the structural, morphological, compositional, and optical properties of the films have been investigated in detailed. Lastly, the photoresponse behavior of the thermally grown Zn_xCd_{1-x}S films was studied as a function of its composition 'x'.

4.2.1 Experimental details

The Zn_xCd_{1-x}S films were grown using a typical thermal evaporation process operated at a vacuum of 2×10^{-6} Torr. Chemically treated glass substrates were used which was kept at a vertical distance of 12 cm from the source. The films were deposited at a substrate temperature of 373K and the thickness of the films was maintained at ~500 nm. Upon deposition, the films were subjected to vacuum annealing at 373K for a duration of 2 hrs. High purity CdS (99.999%) and ZnS (99.995%) powder obtained from Alfa Aesar and Sigma Aldrich were mixed proportionally for various compositions and was used as the source material. Rigaku MiniFlex600 diffractometer system equipped with CuK α radiation ($\lambda = 1.5418 \text{ \AA}$) was utilized to conclude the structural characteristics of the Zn_xCd_{1-x}S films. The elemental composition of the films was studied using an electron dispersion X-ray (EDAX) detector (Oxford Instruments Analytical Ltd.). The gravimetric analysis employing a sensitive electronic microbalance (Sartorius BT 124 S) was used to calculate the thickness of the films. The absorption spectra of the films were recorded at room temperature in the range of 325 – 750 nm using a UV-Vis spectrometer (SpectraPro 2300i). A typical xenon arc lamp (Oriel Instruments, Newport, Model: 66902), an optical power meter (Nova P/N 7Z01500, Ophir), a sourcemeter (Keithley 2400) and an electrometer (Keysight B2985A) were used for determining the photodetector parameters.

4.2.2 Structural studies

X-ray diffraction analysis was carried out to obtain information about the various crystallographic aspects of the Zn_xCd_{1-x}S films. Figure 4.8 displays the XRD spectra of the Zn_{0.45}Cd_{0.55}S thin film deposited at a substrate temperature of 373K prior to the annealing treatment. The two distinct peaks at $2\theta = 26.46^\circ$ and 28.52° in figure 4.8, indicate the improper formation of ternary Zn_xCd_{1-x}S alloy.

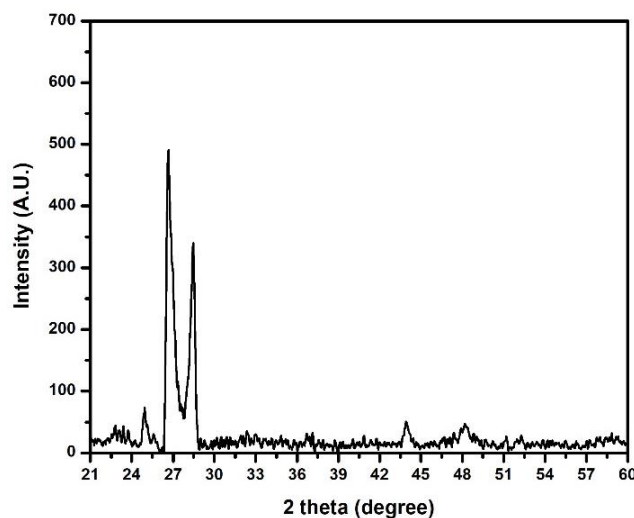


Figure 4.8 XRD spectra of $\text{Zn}_{0.45}\text{Cd}_{0.55}\text{S}$ thin film without annealing treatment.

Therefore, all the films with different compositions were subjected to an annealing treatment at 373K in a vacuum for a duration of 2 hrs. The XRD spectra of the annealed films shown in figure 4.9 revealed the formation of single-phase $\text{Zn}_x\text{Cd}_{1-x}\text{S}$ without any secondary phases (*JCPDS Card No. 00-049-1302*). The sharp peak (figure 4.9a) labeled as (002) at $2\theta = 26.46^\circ$ corresponds to hexagonal CdS thin films (Barman et al. 2018) whereas the peak at $2\theta = 28.52^\circ$ (figure 4.9g) confirms the polycrystalline nature of cubic ZnS films (Barman et al. 2019a). The obtained XRD patterns suggest that the $\text{Zn}_x\text{Cd}_{1-x}\text{S}$ films change from a hexagonal crystal structure to a cubic crystal structure when the zinc concentration is > 0.45 in the films. From figure 4.10, it can be observed that the predominant peak slightly shifts towards higher Bragg angles upon rising Zn concentration in the films.

From table 4.4, it can be noticed that the crystallite size of the (002) predominant peak reduces as Zn content in the $\text{Zn}_x\text{Cd}_{1-x}\text{S}$ thin films increases up to 0.45 in the hexagonal phase which may be due to the stress produced prior to phase change from hexagonal to cubic crystal structure. The lattice parameter, as well as the interplanar spacing of the hexagonal and cubic crystal system, decreases with increasing Zn concentration in the films. This is attributed to higher ionic radii of Cd^{2+} (0.95 Å) compared to that of Zn^{2+} (0.74 Å) in the crystal lattice. The decrease in the lattice parameter and interplanar distance thereby concludes the successful substitution of Cd^{2+} by Zn^{2+} and hence verifies the development of the $\text{Zn}_x\text{Cd}_{1-x}\text{S}$ films.

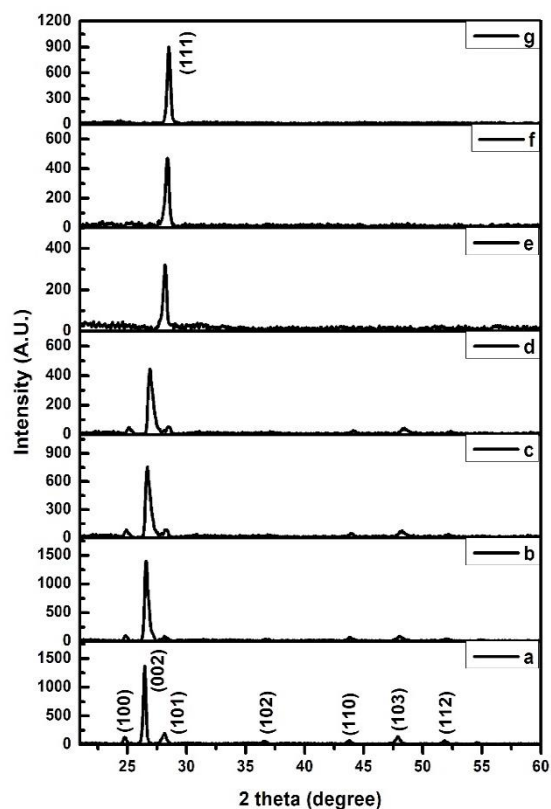


Figure 4.9 XRD diffractograms of $Zn_xCd_{1-x}S$ thin films with $x =$ a) 0, b) 0.15, c) 0.30, d) 0.45, e) 0.70, f) 0.85, and g) 1.

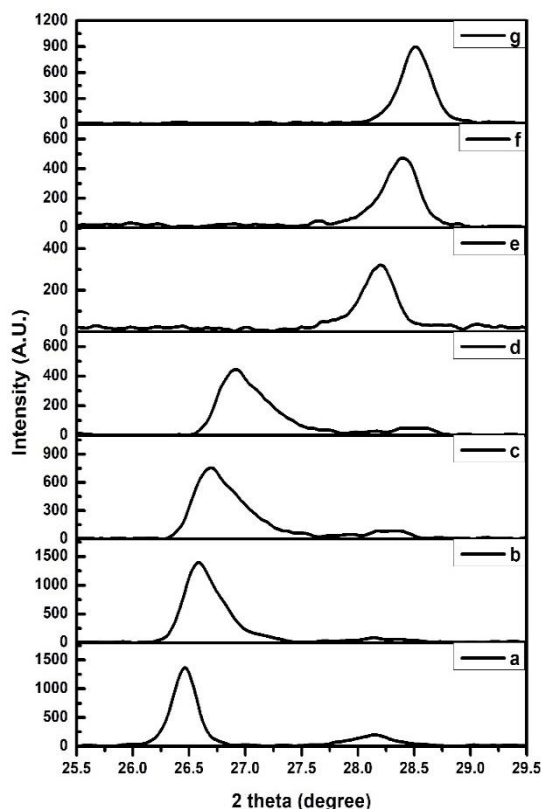


Figure 4.10 Shift in the (002) and (111) peak position of $Zn_xCd_{1-x}S$ thin films with $x =$ a) 0, b) 0.15, c) 0.30, d) 0.45, e) 0.70, f) 0.85, and g) 1.

Table 4.4 XRD diffraction parameters of $Zn_xCd_{1-x}S$ thin films.

Composition	2θ (degree)	Plane	Crystallite Size, D (nm)	Interplanar spacing, d (Å)	a (Å)	c (Å)
CdS	24.77	1 0 0	22.96	3.592	4.147	--
	26.46	0 0 2	31.22	3.366	--	6.732
$Zn_{0.15}Cd_{0.85}S$	24.79	1 0 0	19.55	3.589	4.144	--
	26.58	0 0 2	25.74	3.351	--	6.702
$Zn_{0.30}Cd_{0.70}S$	24.89	1 0 0	17.09	3.574	4.128	--
	26.70	0 0 2	20.72	3.336	--	6.672
$Zn_{0.45}Cd_{0.55}S$	25.16	1 0 0	14.46	3.523	4.076	--
	26.92	0 0 2	20.24	3.304	--	6.619
$Zn_{0.70}Cd_{0.30}S$	28.24	1 1 1	11.12	3.158	5.469	--
$Zn_{0.85}Cd_{0.15}S$	28.42	1 1 1	21.96	3.138	5.435	--
ZnS	28.52	1 1 1	25.27	3.127	5.417	--

4.2.3 Surface morphological & compositional studies

The FE-SEM images of the thermally deposited $Zn_xCd_{1-x}S$ thin films are displayed in figure 4.11. The SEM images indicate the presence of homogeneously distributed large grains throughout the surface of the films without the presence of any pinholes or cracks. Figure 4.11(h) illustrates the cross-sectional micrograph of $Zn_{0.15}Cd_{0.85}S$ thin film. The thickness of the film computed from this figure was found to be in good agreement with the one calculated from the gravimetric analysis. The average grain size estimated from SEM images is tabulated in table 4.5. The various elemental compositions of $Zn_xCd_{1-x}S$ films were verified using EDAX analysis. The EDAX spectra of $Zn_{0.15}Cd_{0.85}S$ thin film is shown in figure 4.12a whereas the elemental mapping shown in figure 4.12b-d revealed that Zn, Cd, and S are equally dispersed through the surface of the sample. The composition of the films listed in table 4.5 was found to be a good agreement with the expected values.

Table 4.5 EDAX analysis & optical band gap of $Zn_xCd_{1-x}S$ thin films a) CdS, b) $Zn_{0.15}Cd_{0.85}S$, c) $Zn_{0.30}Cd_{0.70}S$, d) $Zn_{0.45}Cd_{0.55}S$, e) $Zn_{0.70}Cd_{0.30}S$, f) $Zn_{0.85}Cd_{0.15}S$ and g) ZnS.

Sample	Zn (at%)	Cd (at%)	S (at%)	Avg. Grain Size (nm)	Band Gap, E_g (eV)
a	0	51.59	48.41	113	2.42
b	7.87	44.77	47.36	137	2.46
c	16.95	35.66	47.39	144	2.50
d	23.17	28.22	48.61	140	2.65
e	35.61	17.90	46.49	116	2.89
f	48.11	7.61	44.28	127	3.08
g	54.70	0	45.30	68	3.49

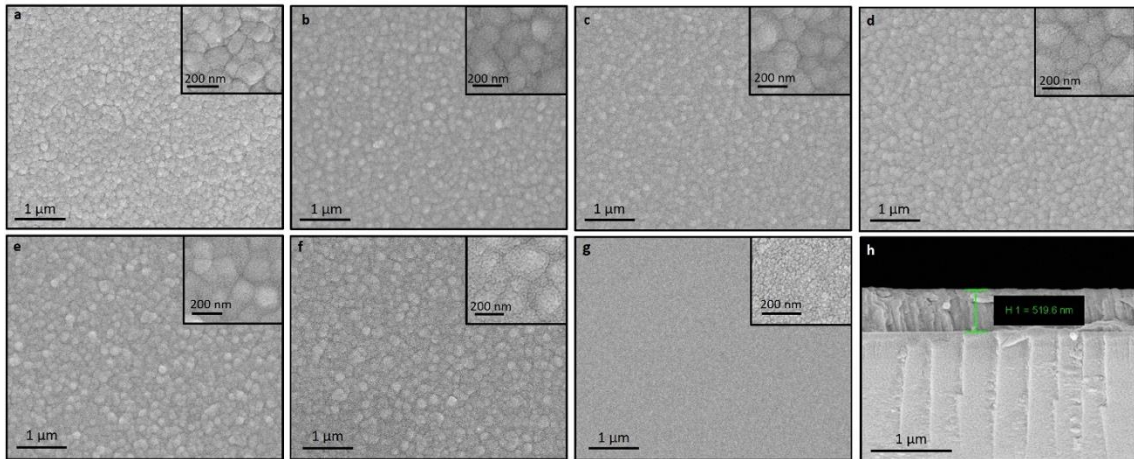


Figure 4.11 FE-SEM images of $Zn_xCd_{1-x}S$ thin films a) CdS, b) $Zn_{0.15}Cd_{0.85}S$, c) $Zn_{0.30}Cd_{0.70}S$, d) $Zn_{0.45}Cd_{0.55}S$, e) $Zn_{0.70}Cd_{0.30}S$, f) $Zn_{0.85}Cd_{0.15}S$, g) ZnS, and h) cross-sectional view of $Zn_{0.15}Cd_{0.85}S$ films.

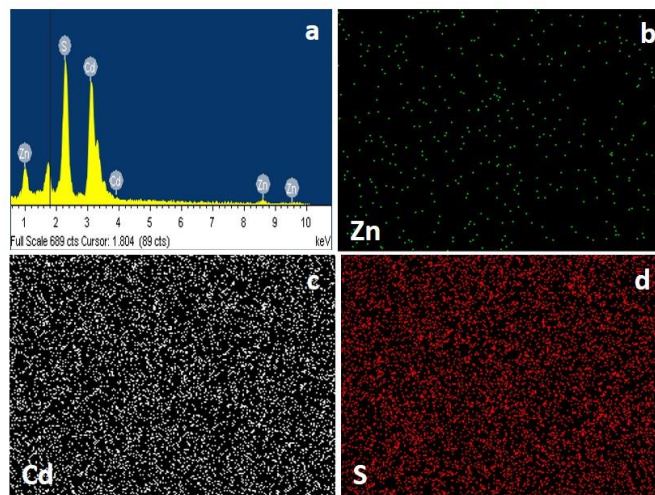


Figure 4.12 (a) EDAX Spectra of $Zn_{0.15}Cd_{0.85}S$ films; Elemental mapping of (b) Cd, (c) Zn, and (d) S.

4.2.4 Opto-electrical studies

The $Zn_xCd_{1-x}S$ thin films were subjected to a UV–Vis spectrometer at room temperature to study its optical properties. The transmittance spectra obtained for the $Zn_xCd_{1-x}S$ films are presented in figure 4.13. It can be seen that all the films are having a transmittance of above 70% and the transmittance of the films rises as the Zn content in the film increases. The presence of an interference pattern in the transmittance spectra at a higher wavelength region indicates the uniform thickness of the films. It

can also be observed that as the Zn concentration in the films increases, the absorption edge moves to lower wavelength values, as reported in other investigations (Azizi et al. 2016). This further confirms the formation of the $Zn_xCd_{1-x}S$ ternary compound as suggested by the XRD analysis.

Figure 4.14 shows the Tauc's plot of the $Zn_xCd_{1-x}S$ thin films. The band gap was estimated from the absorption spectra of the films. The band gap energy values calculated varies from 2.42 – 3.49 eV as the composition 'x' increases from 0.0 to 1.0. Therefore, it can be mentioned that a successful band gap engineering has been achieved for the thermally evaporated $Zn_xCd_{1-x}S$ thin films. The optical band gap for the corresponding binary elements i.e., ZnS and CdS was found to be 3.49 eV and 2.42 eV respectively, as obtained in our previous studies (chapter 3). The obtained band gap values of the films are presented in table 4.5.

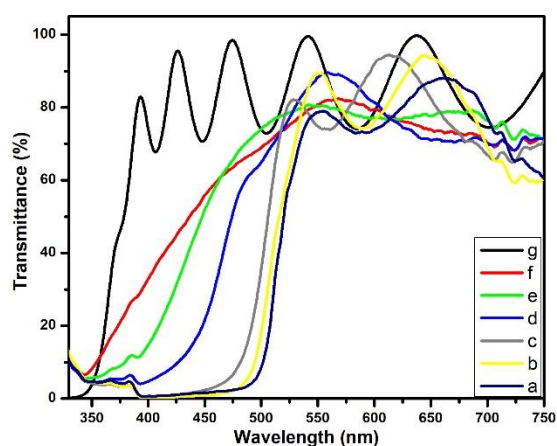


Figure 4.13 Transmittance spectra of $Zn_xCd_{1-x}S$ thin films with $x = a) 0, b) 0.15, c) 0.30, d) 0.45, e) 0.70, f) 0.85, and g) 1$.

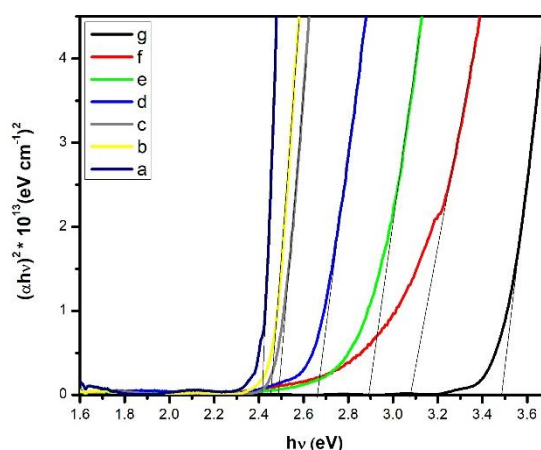


Figure 4.14 Tauc's plot of $Zn_xCd_{1-x}S$ thin films with $x = a) 0, b) 0.15, c) 0.30, d) 0.45, e) 0.70, f) 0.85, and g) 1$.

The variation of ' α ' with 'photon energy' is shown in figure 4.15. It is worth noticing that the absorption coefficient of the $Zn_xCd_{1-x}S$ films is highest when the Zn content is 0.15. The films with higher Zn concentration (> 0.45) were found to be having very less absorption co-efficient and therefore, were not presented in the absorption spectra (figure 4.15). As a result, further opto-electrical properties of the films were also not investigated due to its inferior absorption co-efficient.

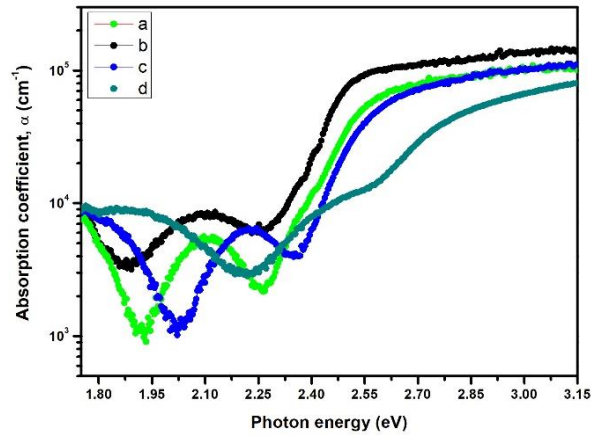


Figure 4.15 Absorption coefficient spectra of the $Zn_xCd_{1-x}S$ films $x =$ a) 0, b) 0.15, c) 0.30, and d) 0.45.

Figure 4.16 shows the variation of band gap over the range of composition ‘x’. By fitting the obtained band gap values with the below quadratic relation, the degree of the non-linear variation of the films can be calculated (Borse et al. 2007):

$$E_g(x) = a + bx + cx^2 \quad (4.1)$$

where ‘c’ is called “bowing parameter”, which is characteristic of a particular alloy system, and ‘x’ is the composition of the film. Equation 4.1 can be simplified to the following relation by polynomial fitting the present data to a quadratic equation:

$$E_g(x) = 2.428 + 0.197x + 0.932x^2 \quad (4.2)$$

Similar values of the bowing parameter were also reported on other $Cd_xZn_{1-x}S$ and $Cd_xZn_{1-x}Se$ based alloy systems (Azizi et al. 2016; Borse et al. 2007; Sutrave et al. 2000).

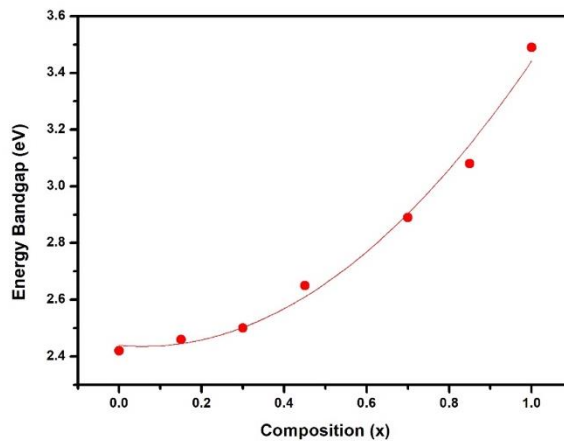


Figure 4.16 Energy band gap (E_g) vs Composition (x) of $Zn_xCd_{1-x}S$ thin films.

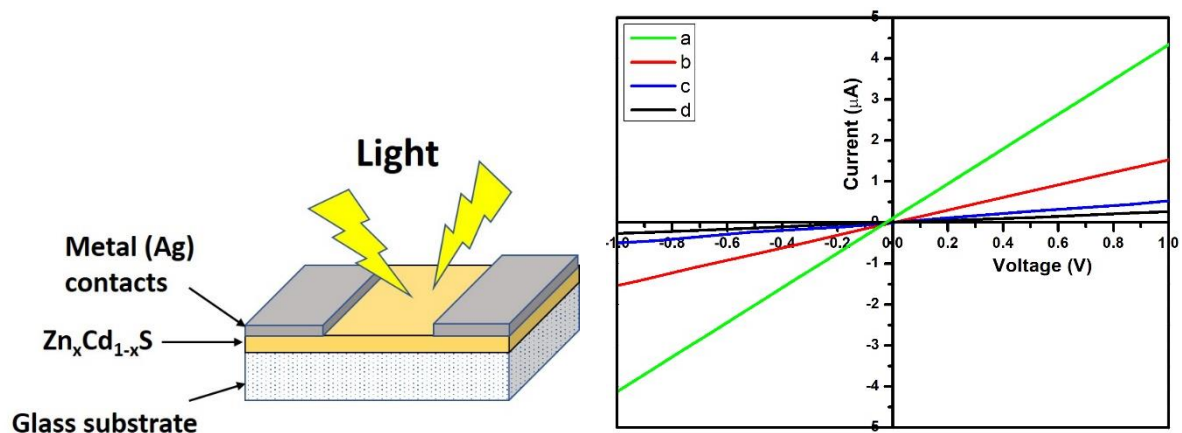


Figure 4.17 Schematic representation of the $Zn_xCd_{1-x}S$ photodetector device.

Figure 4.18 Current Vs Voltage plots of the $Zn_xCd_{1-x}S$ films $x = a) 0, b) 0.15, c) 0.30,$ and $d) 0.45$.

In order to investigate the photo-response characteristics of the $Zn_xCd_{1-x}S$ films, silver (Ag) metal planar contacts (1cm x 1 cm) were thermally deposited on the films, as shown in figure 4.17. Figure 4.18 shows the IV plots of the $Zn_xCd_{1-x}S$ films and it can be witnessed that Ag forms an ohmic contact with the films. The resistance of the films was found to be increasing with increasing Zn concentration as ZnS is a highly resistive semiconductor.

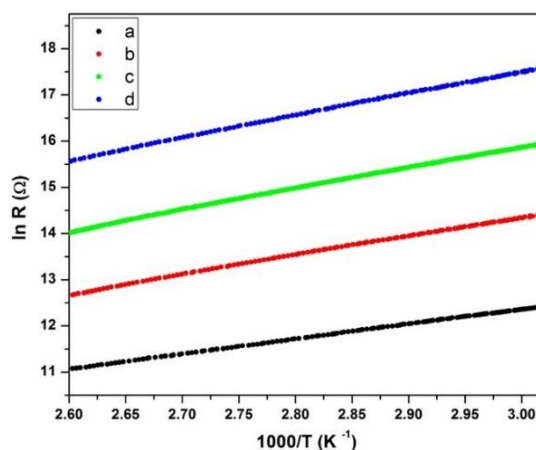


Figure 4.19 $\ln R$ Vs $1000/T$ plot of $Zn_xCd_{1-x}S$ thin films $x = a) 0, b) 0.15, c) 0.30,$ and $d) 0.45$.

The films were found to have n-type conductivity as determined by the hot-probe method. The variation of $\ln(R)$ versus the inverse of temperature was studied to

determine the activation energy associated with the films, as shown in figure 4.19. The decrease in the resistance with increasing temperature confirms the semiconducting behavior of the deposited $Zn_xCd_{1-x}S$ films. From the slope of the plots, the activation energy ‘ E_a ’ associated with the films was calculated and was charted in table 4.6. It can be observed that as the Zn concentration increases, the activation energy of the films increases. This is in good agreement with the current-voltage studies.

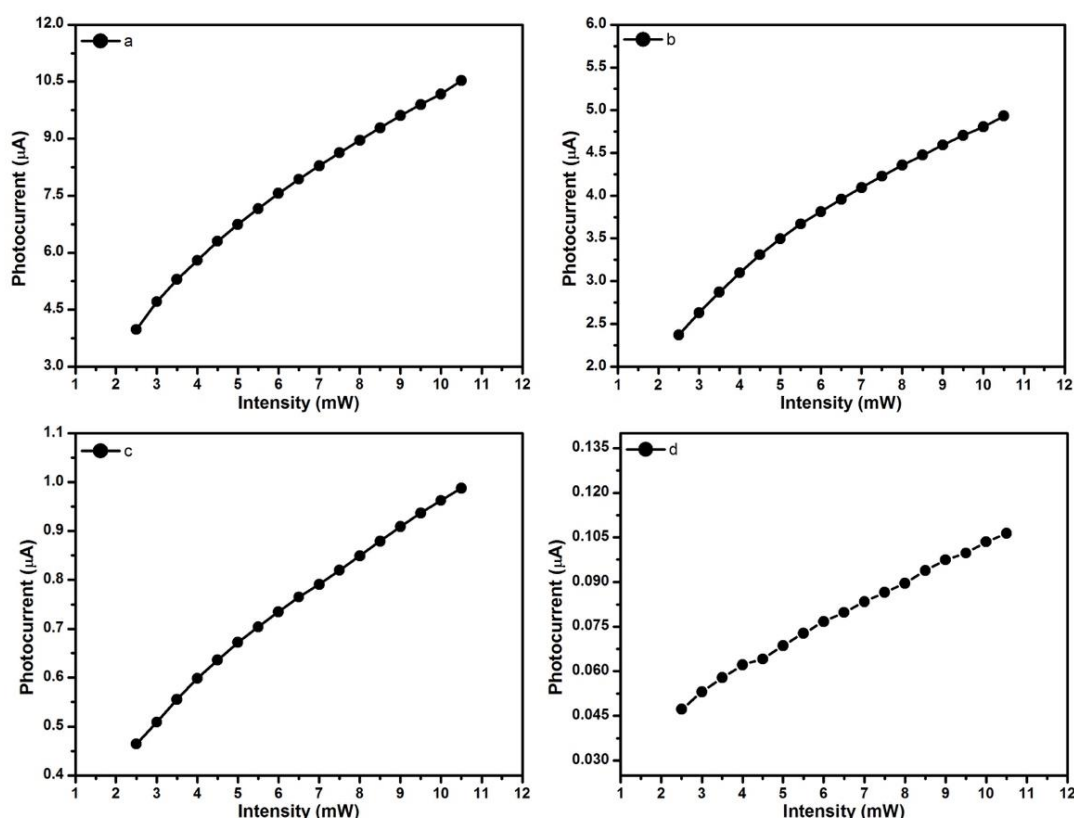


Figure 4.20 Photocurrent Vs Intensity plot of the $Zn_xCd_{1-x}S$ films $x =$ a) 0, b) 0.15, c) 0.30, and d) 0.45.

To evaluate the photodetector properties of the $Zn_xCd_{1-x}S$ films, the illumination intensity was varied and the intensity of the light was monitored using an optical power meter. A biasing voltage of 5V was sourced using an electrometer and the generated photocurrent values were then tabulated as a function of the intensity of the incident light, as displayed in figure 4.20. It can be seen that all the films are photosensitive and the photocurrent intensity increases as the illumination intensity increases. It is worth to notice that a minute variation in the light intensity results in the alteration of the resultant photocurrent. As a result, the $Zn_xCd_{1-x}S$ films can be employed as a very

sensitive photodetector which can be used to detect a tiny variation in the illumination intensity. The generation of the photocurrent decreases with increasing Zn concentration and becomes practically negligible for the films with Zn concentration > 0.45 . Therefore, the films with Zn > 0.45 concentration were not included in the present study.

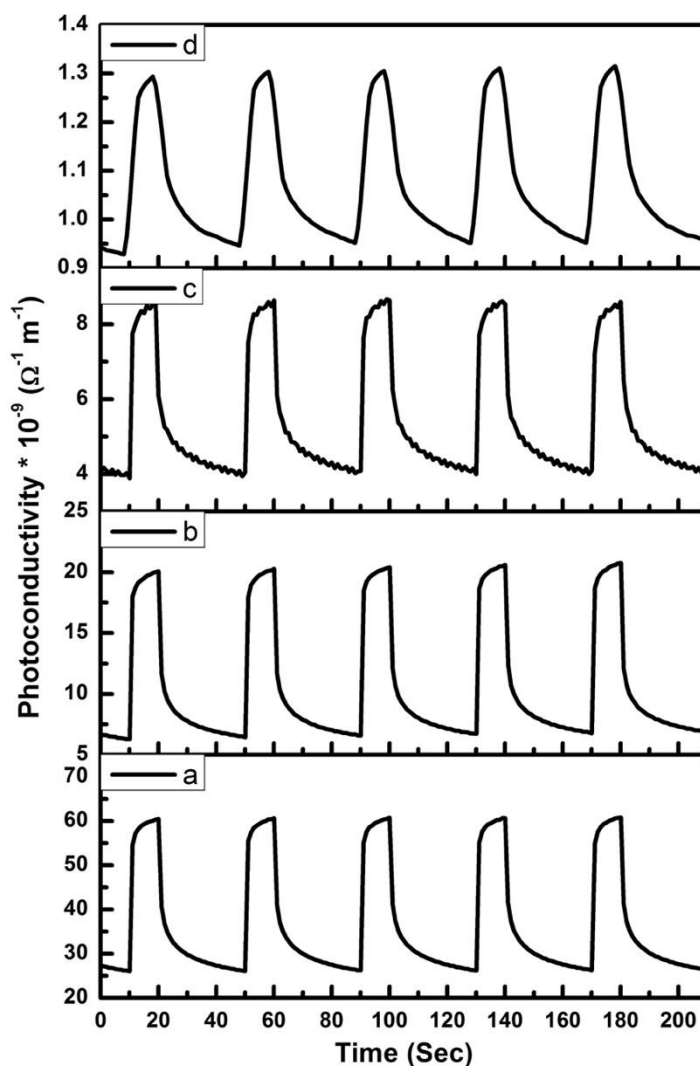


Figure 4.21 Photoconductivity response of the $Zn_xCd_{1-x}S$ thin films under light ON/OFF cycles a) $x = 1$, b) $x = 0.15$, c) $x = 0.30$, and d) $x = 0.45$.

To gain further insight into the stability and repeatability of the photodetector property of the $Zn_xCd_{1-x}S$ films, the illumination intensity was fixed at 5 mW and a biasing voltage of 5V was applied to the films. Figure 4.21 demonstrates the photoconductivity Vs time plot of $Zn_xCd_{1-x}S$ films measured under the following conditions: 10 sec under

illumination and 30 sec without illumination. A computer-controlled shutter was used to precisely control the duration of the ON/OFF cycles. The plot displays five cycles of highly reproducible ON/OFF photoconductivity values and thereby, indicating the repeatability of the photo-detecting nature of the deposited films. All the measurements related to the opto-electrical properties of the films were carried out at room temperature in an air atmosphere with a typical relative humidity of ~80 %. The obtained results suggest that $Zn_xCd_{1-x}S$ films can be successfully employed as a reliable and stable photodetector.

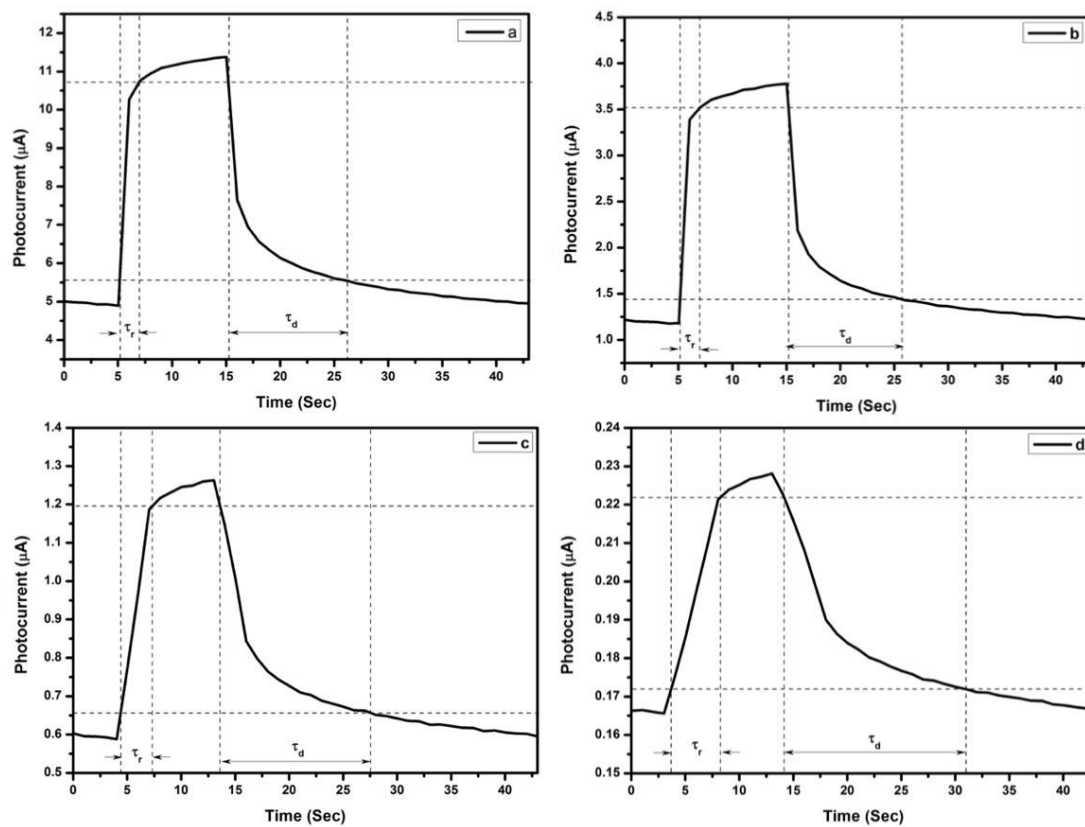


Figure 4.22 Photocurrent Vs time plot of $Zn_xCd_{1-x}S$ thin films $x =$ a) 0, b) 0.15, c) 0.30, and d) 0.45.

The measured photosensitivity value was found to be highest for the $Zn_{0.15}Cd_{0.85}S$ thin films. This could be attributed to the enhanced absorption coefficient of the $Zn_{0.15}Cd_{0.85}S$ films when compared to the other compositions. The response and recovery time associated with the films measured for an ON/OFF pulse is shown in figure 4.22 and is charted in table 4.6. The response time was found to be least for the

CdS films whereas the recovery time was found the minimum for the Zn_{0.15}Cd_{0.85}S films.

Table 4.6 Opto-electrical parameters of Zn_xCd_{1-x}S films x = a) 0, b) 0.15, c) 0.30, and d) 0.45.

Sample	Activation Energy, Ea (meV)	$\sigma_L (\Omega m)^{-1} (x 10^{-9})$	$\sigma_D (\Omega m)^{-1} (x 10^{-9})$	Photo Sensitivity	Response Time, τ_r (Sec)	Recovery Time, τ_d (Sec)
a	641.03	60.56	25.42	1.38	1.76	10.96
b	820.62	20.35	6.32	2.22	1.81	10.52
c	902.02	8.66	3.95	1.19	2.91	13.95
d	949.65	1.31	0.94	0.38	4.56	16.85

4.3 Zn_xSn_{1-x}S thin films

In the present work, Zn_xSn_{1-x}S thin films are deposited on glass substrates using the thermal evaporation method and the influence of composition 'x' on the various properties of Zn_xSn_{1-x}S films is reported along with the application of the films ($x \leq 0.40$) as a photodetector.

4.3.1 Experimental details

From our previous study, it was found that the SnS thin films deposited at 323K exhibits the best photosensitivity and does not contain any other phases corresponding to Sn₂S₃ and SnS₂. Therefore, in the present study, the various compositions of Zn_xSn_{1-x}S thin films were deposited on well-cleaned glass substrates using a thermal evaporation technique at a substrate temperature of 323K under a vacuum of $\sim 2 \times 10^{-6}$ Torr. The substrate was fixed at a distance of 13 cm from the evaporation source and a mixture of ZnS (purity 99.995%, Sigma Aldrich) and SnS (purity 99.5%, Alfa Aesar) powder with appropriate quantities were used as the source element. The deposited films were then subjected to annealing in a vacuum at 373 K for a duration of 1 hr. The film thickness was maintained at ~ 500 nm for the various compositions using gravimetric analysis.

4.3.2 X-ray analysis

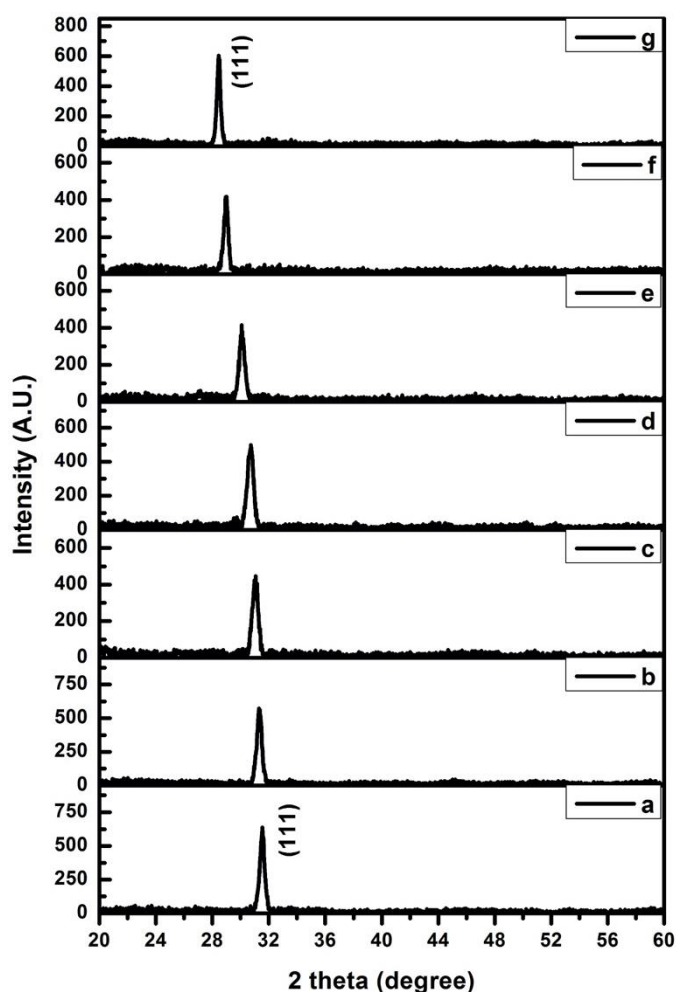


Figure 4.23 XRD diffractograms of $Zn_xSn_{1-x}S$ thin films where $x =$ a) 0, b) 0.10, c) 0.20, d) 0.40, e) 0.70, f) 0.90, and g) 1.

The XRD pattern of the polycrystalline $Zn_xSn_{1-x}S$ ($x = 0, 0.10, 0.20, 0.40, 0.70, 0.90, 1$) thin films is displayed in figure 4.23. The peak (111) at $2\theta = 28.46^\circ$ resembles cubic ZnS thin films (*JCPDS card no. 01-077-2100*) whereas the peak at $2\theta = 31.62^\circ$ can be assigned to orthorhombic SnS (*JCPDS no. 01-075-2115*) with (111) plane. Similar diffractograms were observed for thermally evaporated undoped ZnS and SnS thin films in our previous study (Barman et al. 2019a; b). The occurrence of a single predominant peak as shown in figure 4.23 verifies the homogeneity in the phase formation. It can be seen that the position of the (111) peak shifts monotonically towards higher 2θ angles as the Sn concentration increases which is due to the successful substitution of Zn^{2+} by Sn^{2+} ions. Furthermore, any supplementary peak(s)

corresponding to other phases of SnS and ZnS was not detected. The structural parameters of the thermally grown $Zn_xSn_{1-x}S$ thin films corresponding to (111) plane are tabulated in table 4.7. An increase in the interplanar spacing, as well as crystallite size, with increase in Zn composition can be seen from table 4.7.

Table 4.7 Structural constraints of $Zn_xSn_{1-x}S$ thin films.

Sample	Composition	2 θ (degree)	Interplanar Spacing, d_{hkl} (nm)	Crystallite size, D (nm)
a	SnS	31.62	0.283	18.52
b	$Zn_{0.10}Sn_{0.90}S$	31.32	0.285	18.61
c	$Zn_{0.20}Sn_{0.80}S$	31.06	0.288	19.15
d	$Zn_{0.40}Sn_{0.60}S$	30.71	0.291	19.26
e	$Zn_{0.70}Sn_{0.30}S$	30.08	0.297	19.54
f	$Zn_{0.90}Sn_{0.10}S$	28.97	0.308	19.94
g	ZnS	28.46	0.312	20.30

4.3.3 Morphological analysis

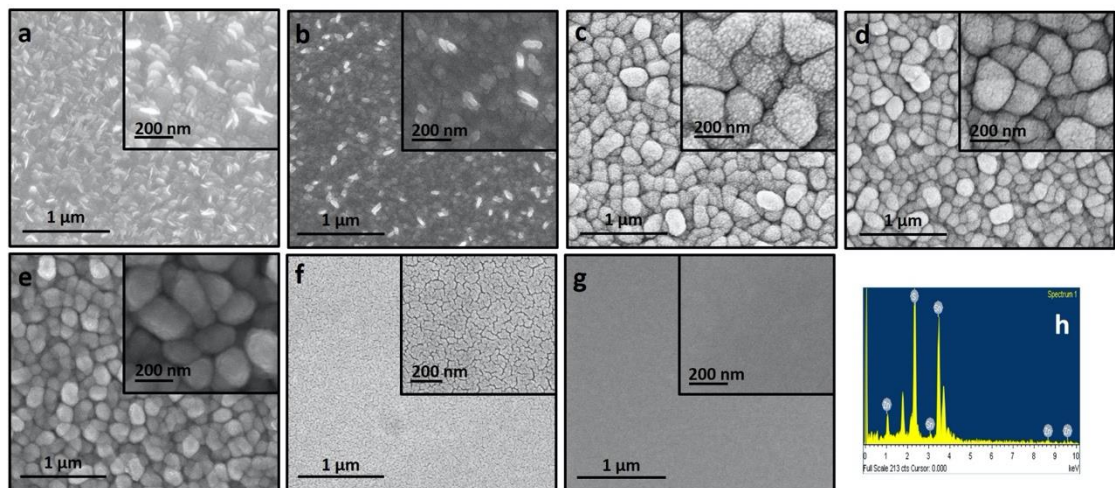


Figure 4.24 FE-SEM images of $Zn_xSn_{1-x}S$ thin films: x = a) 0, b) 0.10, c) 0.20, d) 0.40, e) 0.70, f) 0.90, g) 1, and h) EDAX spectra of $Zn_{0.10}Sn_{0.90}S$ thin film.

Figure 4.24 shows the FE-SEM micrographs of $Zn_xSn_{1-x}S$ films with various values of the composition 'x'. The lower magnification micrographs depict the uniformity of the

films without the presence of any pin-holes and crack, whereas, in the higher magnification images (figure 4.24 insets) provides visualization of the fine structures of the film. The morphology of the films alters from a tightly packed flake-type structure (figure 4.24a) to granular structure as the Zn concentration increases. These findings suggest that Zn incorporation in the $Zn_xSn_{1-x}S$ thin films alters the surface morphological properties of the films. EDAX analysis was performed in order to quantize the composition of the deposited films. The presence of zinc (Zn), tin (Sn) and sulfur (S) in the $Zn_{0.10}Sn_{0.90}S$ thin films can be seen in the EDAX spectra (figure 4.24h).

Table 4.8 Compositional, optical, and electrical parameters of $Zn_xSn_{1-x}S$ thin films.

Sample	Zn (at%)	Sn (at%)	S (at%)	Energy band gap, E_g (eV)	Activation Energy, E_a (eV)
SnS	--	49.72	50.28	1.54	0.72
$Zn_{0.10}Sn_{0.90}S$	05.04	44.92	50.04	1.78	0.69
$Zn_{0.20}Sn_{0.80}S$	09.17	41.32	49.51	1.84	0.74
$Zn_{0.40}Sn_{0.60}S$	20.08	31.57	48.35	2.13	0.98
$Zn_{0.70}Sn_{0.30}S$	34.81	16.72	48.47	2.91	--
$Zn_{0.90}Sn_{0.10}S$	45.28	05.07	49.65	3.01	--
ZnS	50.96	--	49.04	3.49	--

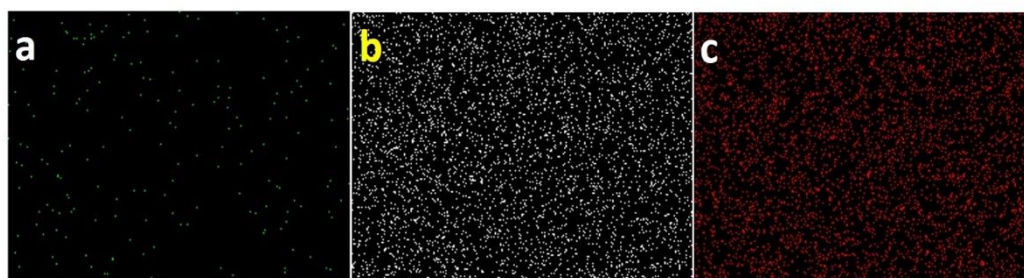


Figure 4.25 Elemental mapping of $Zn_{0.10}Sn_{0.90}S$ thin film (a) Zn, (b) Sn, and (c) S.

Figure 4.25a-c displays the elemental mapping of Zn, Sn, and S obtained for the $Zn_{0.10}Sn_{0.90}S$ thin film. It can be noticed that Zn, Sn, and S are uniformly scattered throughout the surface of the $Zn_{0.10}Sn_{0.90}S$ film. The various atomic percentages of Zn, Sn, and S obtained for the $Zn_xSn_{1-x}S$ thin films are charted in table 4.8.

4.3.4 Opto-electrical studies

The optical transmittance spectra of the $Zn_xSn_{1-x}S$ thin films are depicted in figure 4.26. The maximum transparency was found for the undoped ZnS thin films. The occurrence of interference patterns in the transmittance spectra at the higher wavelength region indicates that the films are uniformly deposited (Benyahia et al. 2015b).

The plots of $(\alpha h\nu)^2$ vs photon energy for the $Zn_xSn_{1-x}S$ thin films is presented in figure 4.27a-g. The linear fitting of the plot indicates a direct allowed transition type. The band gap values were determined from the intercepts of the $(\alpha h\nu)^2$ values with the energy axis and were tabulated in table 4.8. The obtained band gap values of SnS and ZnS films matched well with the previous works (Barman et al. 2019c; b). From table 4.8, it can be observed that as the Sn concentration increases, the band gap of the $Zn_xSn_{1-x}S$ films decreases (figure 4.27h). This further confirms the successful replacement of Zn^{2+} by Sn^{2+} ions which is in good agreement with the XRD results.

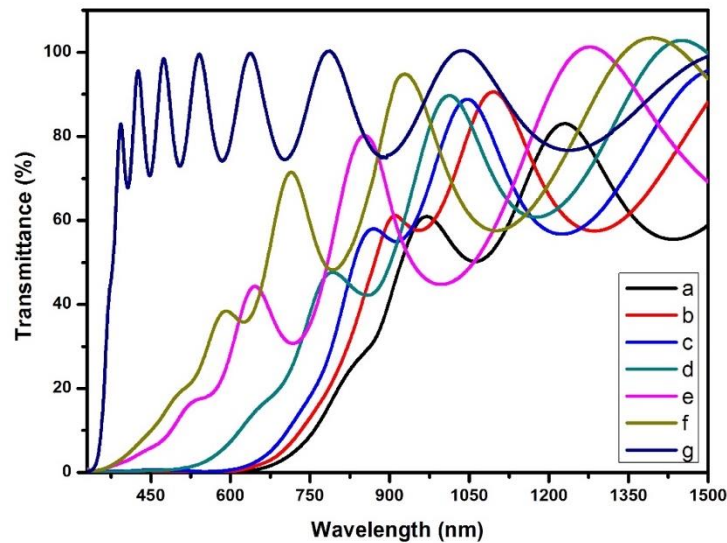


Figure 4.26 Transmittance spectra of $Zn_xSn_{1-x}S$ thin films a) $x = 0$, b) $x = 0.10$, c) $x = 0.20$, d) $x = 0.40$, e) $x = 0.70$, f) $x = 0.90$, and g) $x = 1$.

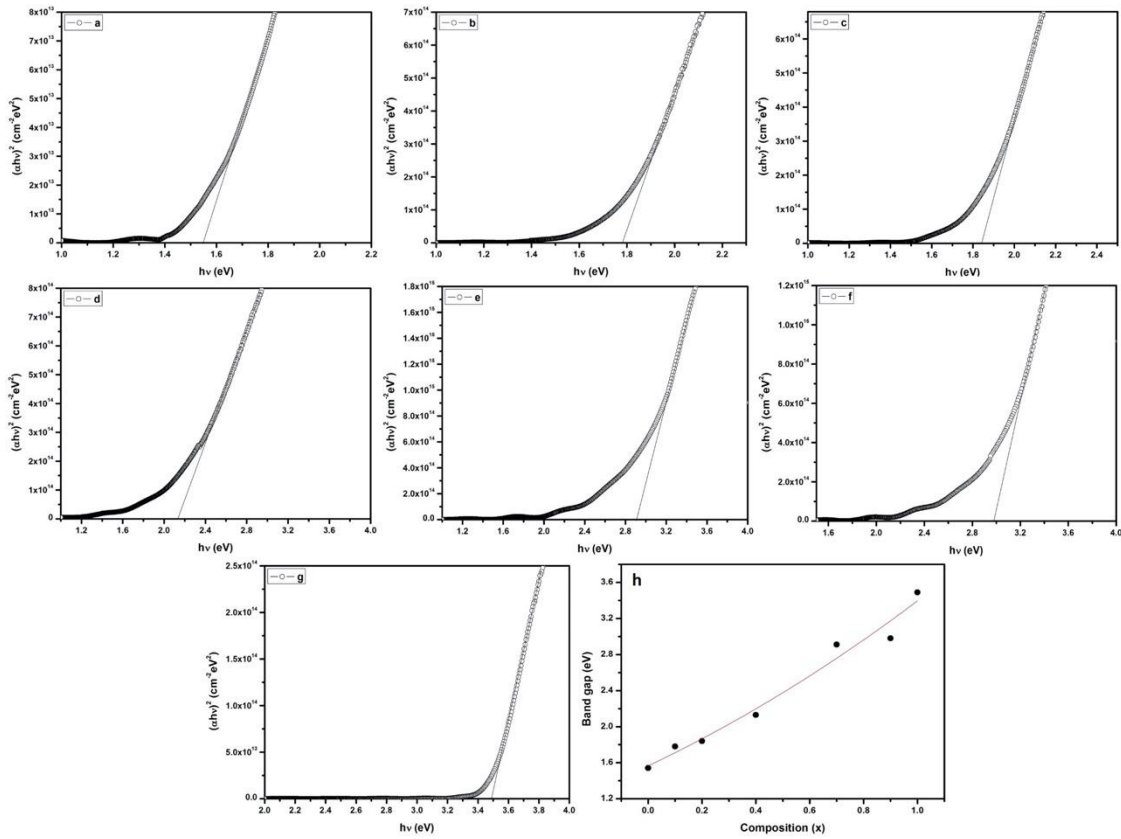


Figure 4.27 Tauc's plot of $\text{Zn}_x\text{Sn}_{1-x}\text{S}$ thin films a) $x = 0$, b) $x = 0.10$, c) $x = 0.20$, d) $x = 0.40$, e) $x = 0.70$, f) $x = 0.90$, g) $x = 1$, and h) Variation of band gap with composition 'x'.

The variation in the E_g values can be described by equation 4.1. By polynomial fitting the obtained band gap data (figure 4.27h), the above equation becomes:

$$E_g(x) = 1.56 + 1.41x + 0.41x^2 \quad (4.3)$$

The deviation of ' α ' with 'photon energy' for films with Zn content ≤ 0.40 is displayed in figure 4.28. It can be observed that the incorporation of Zn into the SnS films results in the enhancement of the absorption coefficient. This proposes that these films can be utilized as an absorber layer in solar cells. It is also worth noting that the $\text{Zn}_{0.10}\text{Sn}_{0.90}\text{S}$ thin film is having the maximum absorption coefficient. The superior absorption coefficient of the films results in the enhancement of the photosensitivity of the films as discussed in the following part of the work. The films with ' x ' > 0.40 were found to have a very low value of absorption coefficient and thus were not included in the photosensitivity studies.

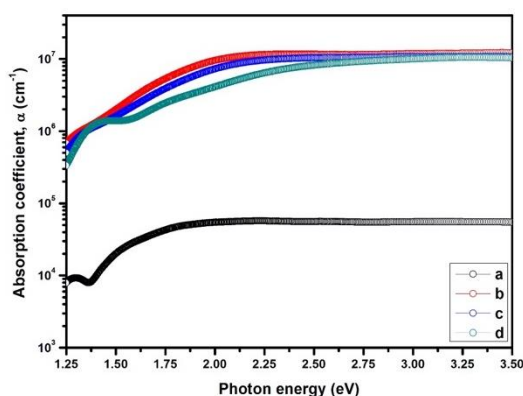


Figure 4.28 Plot of α Vs $h\nu$ of $Zn_xSn_{1-x}S$ thin films a) $x = 0$, b) $x = 0.10$, c) $x = 0.20$, and d) $x = 0.40$.

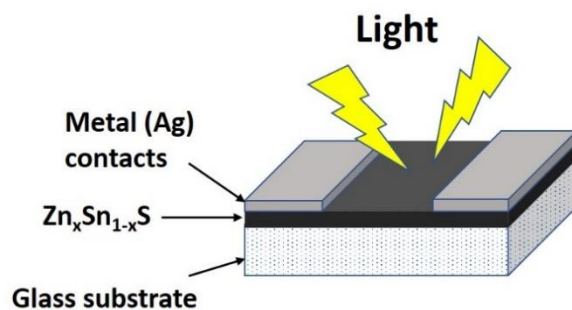


Figure 4.29 Schematic representation of Ag/ $Zn_xSn_{1-x}S$ /glass photodetector.

Silver (Ag) contacts (1 cm x 1 cm; 1 mm gap) were deposited onto the films using a thermal evaporation system to determine the electrical properties of the $Zn_xSn_{1-x}S$ thin films, as displayed in figure 4.29. The IV plots shown in figure 4.30 confirms the ohmic behavior of $Zn_xSn_{1-x}S$ thin films with Ag metal contacts. The films with Zn concentration ' x ' > 0.40 were found to be having very high resistance and therefore, were not included in electrical studies. The hot-probe technique was employed to determine the majority charge carrier type and it was found that the $Zn_xSn_{1-x}S$ films ($x \leq 0.40$) exhibited p-type conductivity.

The plot of $\ln(R)$ Vs $1000/T$ of the $Zn_xSn_{1-x}S$ films is shown in figure 4.31. It can be observed that $\ln(R)$ varies linearly with the temperature. The indirect relation of the resistance with temperature confirms the semiconducting behavior of the $Zn_xSn_{1-x}S$ films.

The photoconductivity Vs time plot of the $Zn_xSn_{1-x}S$ films is depicted in figure 4.32. A biasing voltage of 5V was applied to the films and photo-response characteristics were carried out in the following sequences at a light intensity of 10 mW/cm^2 : 10 secs under illumination and 30 secs in the dark. The light shutter was controlled using a programmable computer-controlled shutter. Figure 4.32 demonstrates four highly reproducible ON/OFF photoconductivity cycles and thereby demonstrating the stability of $Zn_xSn_{1-x}S$ thin films as a photodetector.

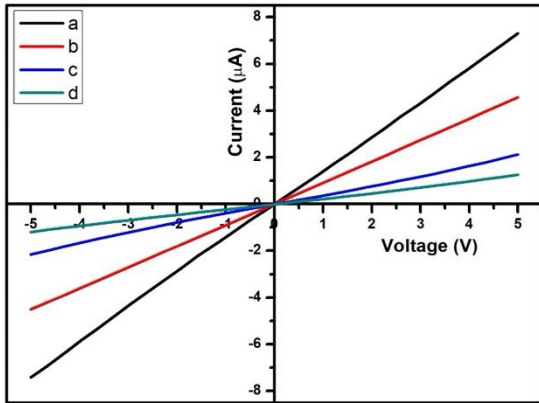


Figure 4.30 IV plot of $Zn_xSn_{1-x}S$ films
 a) $x = 0$, b) $x = 0.10$, c) $x = 0.20$, and d)
 $x = 0.40$.

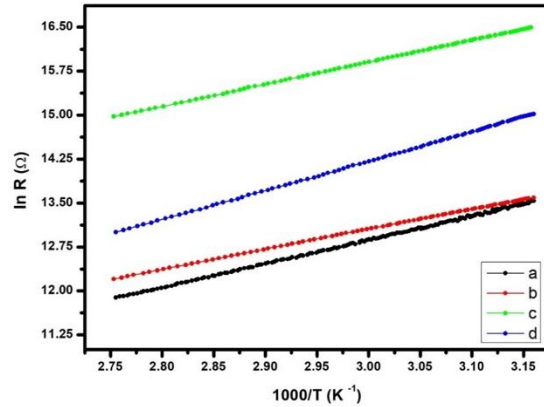


Figure 4.31 $\ln R$ Vs $1000/T$ plot of
 $Zn_xSn_{1-x}S$ thin films a) $x = 0$, b) $x =$
 0.10 , c) $x = 0.20$, and d) $x = 0.40$.

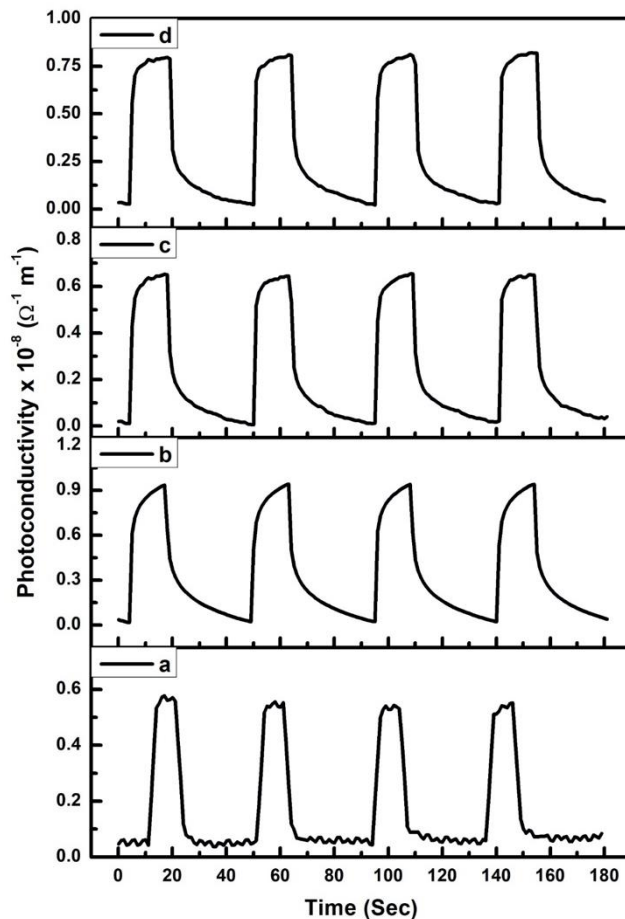


Figure 4.32 Photoconductivity Vs Time response of $Zn_xSn_{1-x}S$ thin films a) $x = 0$, b)
 $x = 0.10$, c) $x = 0.20$, and d) $x = 0.40$.

Table 4.9 Photo-response parameters of $Zn_xSn_{1-x}S$ thin films a) $x = 0$, b) $x = 0.10$, c) $x = 0.20$, and d) $x = 0.40$.

Sample	$\sigma_L (\Omega m)^{-1}$	$\sigma_D (\Omega m)^{-1}$	Respo nsivity ($A W^{-1}$)	Photo Sensitivity	Response Time, τ_r (Sec)	Recovery Time, τ_d (Sec)
a	0.573×10^{-8}	0.048×10^{-8}	0.99	10.93	2.48	2.86
b	0.932×10^{-8}	0.021×10^{-8}	9.61	43.38	5.55	15.93
c	0.646×10^{-8}	0.016×10^{-8}	5.09	39.37	2.29	10.01
d	0.793×10^{-8}	0.027×10^{-8}	5.43	28.37	2.29	11.52

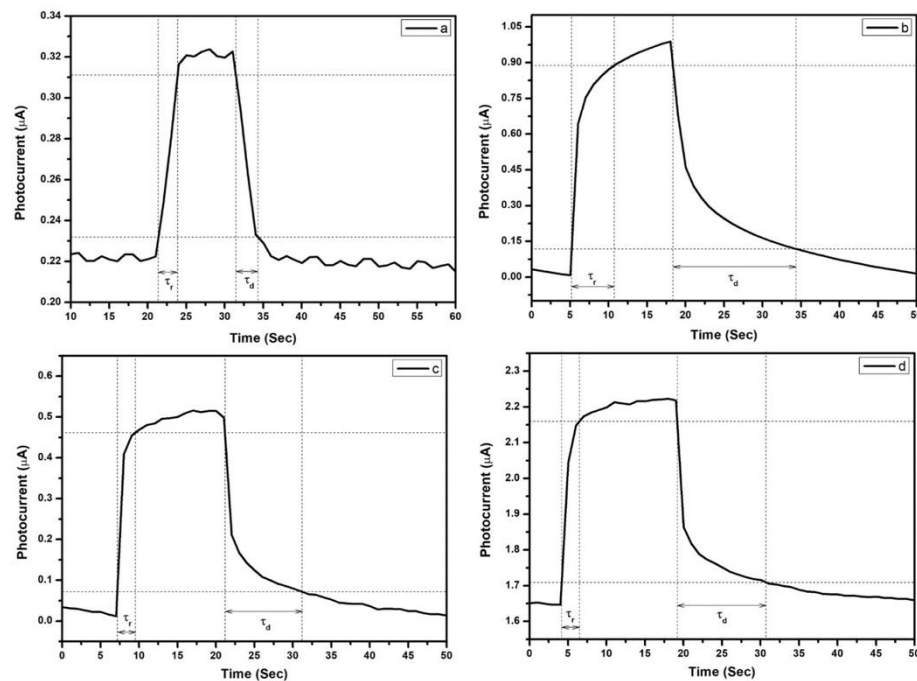


Figure 4.33 Response time and recovery time of $Zn_xSn_{1-x}S$ thin films a) $x = 0$, b) $x = 0.10$, c) $x = 0.20$, and d) $x = 0.40$.

The recovery and response time of $Zn_xSn_{1-x}S$ thin films for one ON/OFF cycle is shown in figure 4.33. The obtained photoresponsivity and photosensitivity values along with the photocurrent response and recovery time are charted in table 4.9. A maximum photosensitivity value of 43.38 was obtained for $Zn_{0.10}Sn_{0.90}S$ thin films. It can be noticed that the recovery and response time of SnS thin film is lowest. This might be due to the absence of trap/impurity levels introduced due to the incorporation of foreign Zn atoms in $Zn_xSn_{1-x}S$ thin films.

CHAPTER – 5

CHAPTER 5

SUMMARY AND CONCLUSIONS

Overview:

This chapter deals with the summary of the research work carried out and the conclusions drawn from the results of investigations. The scope for future work is also discussed.

5.1 Summary of the present work

The work presented in this thesis is broadly classified into five chapters with several sections within the individual chapter. The first chapter covers a brief introduction to thin film technology, compound semiconductors, photodetectors, literature survey, scope and objectives of the work. The second chapter contains experimental and characterization techniques employed in the present work. The third chapter describes a detailed study on the optimization of growth conditions for the binary compounds namely ZnS, CdS, and SnS thin films along with their various properties. The fourth chapter describes the preparation, results, and discussion of $\text{Cu}_x(\text{ZnS})_{1-x}$, $\text{Zn}_x\text{Cd}_{1-x}\text{S}$, and $\text{Zn}_x\text{Sn}_{1-x}\text{S}$ thin films. Finally, the fifth chapter summarizes the conclusions drawn from the results of investigations.

5.2 Conclusions

5.2.1 Binary metal sulfides

Highly stable binary sulfides viz., ZnS, CdS, SnS thin films were successfully deposited on pre-cleaned glass substrate using thermal evaporation technique. Both ZnS and CdS thin films were found to be stoichiometric when the films were grown at a substrate temperature of 373K, whereas the SnS films were found to be stoichiometric when deposited at a substrate temperature of 323K. The ZnS films were found to be highly transparent with band gap of 3.51 eV. The CdS films were hexagonal in nature with the predominant orientation along (002) plane. Highest transparency was achieved for stoichiometric CdS thin films makes them suitable for window layer application. The

band gap of the CdS films was found to be ~ 2.42 eV and the photosensitivity was found to be highest at 1.27 for stoichiometric CdS thin films. The SnS films were polycrystalline in nature with the preferred orientation along (111) having an orthorhombic structure. The films grown at 323 K substrate temperature were single-phase SnS and had the most attractive characteristics. The optical bandgap energy as well as the activation energy decreases from 1.576 eV to 1.429 eV and 0.806 eV to 0.397 eV, respectively, as the substrate temperature increases from 297 K to 423 K. Photosensitivity was found to be highest at 10.93 for stoichiometric SnS film composition deposited at 323 K.

5.2.2 Ternary metal sulfides

The ternary sulfides namely $\text{Cu}_x(\text{ZnS})_{1-x}$, $\text{Zn}_x\text{Cd}_{1-x}\text{S}$, and $\text{Zn}_x\text{Sn}_{1-x}\text{S}$ thin films were deposited successfully onto well-cleaned glass substrates using thermal evaporation technique. The optical band gap of the $\text{Cu}_x(\text{ZnS})_{1-x}$ films decreases from 3.48 eV to 2.60 eV whereas the electrical conductivity increases when Cu concentration in the film is varied from 0 to 0.25. The excellent electrical conductivity combined with good transparency of the $\text{Cu}_x(\text{ZnS})_{1-x}$ thin films especially at low Cu concentration ($x \leq 0.03$) makes them suitable for application as a transparent conducting material. Further, the films with higher copper concentration ($x > 0.03$) can be used as a buffer/window layer in solar cells.

The $\text{Zn}_x\text{Cd}_{1-x}\text{S}$ thin films were found to have a hexagonal crystal structure with a preferential orientation along (002) plane and as the Zn concentration increases beyond 0.45, the crystal system changes to a cubic structure along (111) plane. The optical energy band gap was found to be increasing non-linearly with increasing Zn concentration. A successful band gap tailoring was achieved by a suitable variation in the composition of the films. All the films ($x = 0, 0.15, 0.30, \text{ and } 0.45$) displayed an increase in the photoconductivity values with increasing illumination intensity and thereby suggesting that the films can be utilized as a sensitive photodetector. The films showed 5 cycles of highly reproducible photoconductivity plots and thus demonstrating the stability and repeatability of the photodetector. Among the various compositions, the $\text{Zn}_{0.15}\text{Cd}_{0.85}\text{S}$ films exhibited the best photosensitivity of 2.22. The obtained results imply that $\text{Zn}_x\text{Cd}_{1-x}\text{S}$ films are an excellent candidate for photodetectors.

The $Zn_xSn_{1-x}S$ ($0 \leq x \leq 1$) thin films were found to be polycrystalline in nature with a favored orientation along (111) plane. The presence of a shift in (111) peak position from 28.46° to 31.62° validates the formation of a solid solution. The energy band gap decreases from 3.49 eV to 1.54 eV as the Sn concentration in the films increases. The tunable band gap suggests that these films are suitable for a wide range of opto-electrical applications, particularly in solar cells. Further, the films ($x \leq 0.40$) were analyzed for photodetector applications. The $Zn_xSn_{1-x}S$ film with $x = 0.10$ exhibited the highest photosensitivity of 43.38 which is ~ 4 times higher than that of SnS films indicating its applications as an outstanding candidate for photodetectors.

5.3 Scope for future work

The present work involves the computation of the photodetector parameters at a broad spectrum (200 – 1000 nm wavelength region). Therefore, further photosensitivity studies on the behavior of the films can be carried out at an individual wavelength. Also, the present study involves various compositions of ternary alloys which displayed excellent opto-electrical properties. In addition, the $Zn_xSn_{1-x}S$ ($x \leq 0.40$) comprises an outstanding absorption co-efficient of $\sim 10^7 \text{ cm}^{-1}$. Hence, there is a scope to implement these materials in solar cells. Further, the materials can also be deposited on a flexible substrate in order to fabricate a highly sensitive flexible photodetector. Employing low-cost chemical methods to grow such ternary alloys with different compositions for various large area devices may be an area worth pursuing.

References

- Aguilar-Hernández, J., Sastre-Hernández, J., Ximello-Queibras, N., Mendoza-Pérez, R., Vigil-Galán, O., Contreras-Puente, G., and Cárdenas-García, M. (2006). "Photoluminescence studies on CdS-CBD films grown by using different S/Cd ratios." *Thin Solid Films*, 511–512, 143–146.
- Alam, F., and Dutta, V. (2015). "Tin sulfide (SnS) nanostructured films deposited by continuous spray pyrolysis (CoSP) technique for dye-sensitized solar cells applications." *Appl. Surf. Sci.*, 358, 491–497.
- Andrade-Arvizu, J. A., Courel-Piedrahita, M., and Vigil-Galán, O. (2015). "SnS-based thin film solar cells: perspectives over the last 25 years." *J. Mater. Sci. Mater. Electron.*, 26(7), 4541–4556.
- Aramoto, T., Kumazawa, S., Higuchi, H., Arita, T., Shibutani, S., Nishio, T., Nakajima, J., Tsuji, M., Hanafusa, A., Hibino, T., Omura, K., Ohyama, H., and Murozono, M. (1997). "16.0% efficient thin-film CdS/CdTe solar cells." *Japanese J. Appl. Physics, Part 1 Regul. Pap. Short Notes Rev. Pap.*, 36(10), 6304–6305.
- Arepalli, V. K., Shin, Y., and Kim, J. (2019). "Photovoltaic behavior of the room temperature grown RF-Sputtered SnS thin films." *Opt. Mater. (Amst.)*, 88(December 2018), 594–600.
- Arulanantham, A. M. S., Valanarasu, S., Jeyadheepan, K., Ganesh, V., and Shkir, M. (2018). "Development of SnS (FTO/CdS/SnS) thin films by nebulizer spray pyrolysis (NSP) for solar cell applications." *J. Mol. Struct.*, 1152, 137–144.
- Asogwa, P. U. (2010). "Variation of optical properties with post deposition annealing in chemically deposited CdZnS thin films." *Chalcogenide Lett.*, 7(8), 501–508.
- Azizi, S., Rezagholipour Dizaji, H., and Ehsani, M. H. (2016). "Structural and optical properties of Cd_{1-x}Zn_xS (x = 0, 0.4, 0.8 and 1) thin films prepared using the precursor obtained from microwave irradiation processes." *Optik (Stuttg.)*, 127(18), 7104–7114.
- Bacha, K. Ben, Bitri, N., and Bouzouita, H. (2016). "Effect of annealing parameters on structural and morphological properties of sprayed ZnS thin films." *Optik (Stuttg.)*, 127(5), 3100–3104.

- Banai, R. E., Horn, M. W., and Brownson, J. R. S. (2016). "A review of tin (II) monosulfide and its potential as a photovoltaic absorber." *Sol. Energy Mater. Sol. Cells*, 150, 112–129.
- Banerjee, A. N., and Chattopadhyay, K. K. (2005). "Recent developments in the emerging field of crystalline p-type transparent conducting oxide thin films." *Prog. Cryst. Growth Charact. Mater.*, 50(1–3), 52–105.
- Barman, B., Bangera, K. V., and Shivakumar, G. K. (2018). "Effect of substrate temperature on the suitability of thermally deposited cadmium sulfide thin films as window layer in photovoltaic cells." *Superlattices Microstruct.*, 123(September), 374–381.
- Barman, B., Bangera, K. V., and Shivakumar, G. K. (2019a). "Preparation of thermally deposited $\text{Cu}_x(\text{ZnS})_{1-x}$ thin films for opto-electronic devices." *J. Alloys Compd.*, 772, 532–536.
- Barman, B., Bangera, K. V., and Shivakumar, G. K. (2019b). "Superlattices and Microstructures Evaluation of semiconducting p-type tin sulfide thin films for photodetector applications." *Superlattices Microstruct.*, 133(June), 106215.
- Barman, B., Bangera, K. V., and Shivakumar, G. K. (2019c). "Preparation of thermally deposited $\text{Cu}_x(\text{ZnS})_{1-x}$ thin films for opto-electronic devices." *J. Alloys Compd.*, 772, 532–536.
- Basak, A., Hati, A., Mondal, A., Singh, U. P., and Taheruddin, S. K. (2018). "Effect of substrate on the structural, optical and electrical properties of SnS thin films grown by thermal evaporation method." *Thin Solid Films*, 645(October 2017), 97–101.
- Bashkurov, S. A., Gremenok, V. F., Ivanov, V. A., Lazenka, V. V., and Bente, K. (2012). "Tin sulfide thin films and Mo/p-SnS/n-CdS/ZnO heterojunctions for photovoltaic applications." *Thin Solid Films*, 520(17), 5807–5810.
- Benyahia, K., Benhaya, A., and Aida, M. S. (2015a). "ZnS thin films deposition by thermal evaporation for photovoltaic applications." *J. Semicond.*, 36(10), 3–6.
- Benyahia, K., Benhaya, A., and Aida, M. S. (2015b). "ZnS thin films deposition by thermal evaporation for photovoltaic applications." *J. Semicond.*, 36(10), 103001.
- Bhattacharya, R. N., and Ramanathan, K. (2004). "Cu(In,Ga)Se₂ thin film solar cells with buffer layer alternative to CdS." *Sol. Energy*, 77(6), 679–683.
- Borse, S. V., Chavhan, S. D., and Sharma, R. (2007). "Growth, structural and optical

properties of Cd_{1-x}Zn_xS alloy thin films grown by solution growth technique (SGT).” *J. Alloys Compd.*, 436(1–2), 407–414.

Broser, I., Fricke, C., Lummer, B., Heitz, R., Perls, H., and Hoffmann, A. (1992). “Optical nonlinearity and fast switching due to birefringence and mode coupling in CdS crystals.” *J. Cryst. Growth*, 117(1–4), 788–792.

Byungha Shin, Oki Gunawan, Yu Zhu, Nestor A. Bojarczuk, S. J. C. and S. G. (2011). “Thin film solar cell with 8.4% power conversion efficiency using an earth-abundant Cu₂ZnSnS₄ absorber.” *Prog. Photovolt Res. Appl.*, 21(January 2013), 72–76.

Caballero, R., Condé, V., and León, M. (2016). “SnS thin films grown by sulfurization of evaporated Sn layers: Effect of sulfurization temperature and pressure.” *Thin Solid Films*, 612, 202–207.

Carcia, P. F., McLean, R. S., Reilly, M. H., and Nunes, G. (2003). “Transparent ZnO thin-film transistor fabricated by rf magnetron sputtering.” *Appl. Phys. Lett.*, 82(7), 1117–1119.

Carreón-Moncada, I., González, L. A., Pech-Canul, M. I., and Ramírez-Bon, R. (2013). “Cd_{1-x}Zn_xS thin films with low Zn content obtained by an ammonia-free chemical bath deposition process.” *Thin Solid Films*, 548, 270–274.

Chaki, S. H., Chaudhary, M. D., and Deshpande, M. P. (2016). “SnS thin films deposited by chemical bath deposition, dip coating and SILAR techniques.” *J. Semicond.*, 37(5), 053001.

Chalapathi, U., Poornaprakash, B., and Park, S. H. (2016). “Chemically deposited cubic SnS thin films for solar cell applications.” *Sol. Energy*, 139, 238–248.

Das, S., and Jayaraman, V. (2014). “SnO₂: A comprehensive review on structures and gas sensors.” *Prog. Mater. Sci.*, 66, 112–255.

Davies, D. A., Silver, J., Vecht, A., Marsh, P. J., and Rose, J. A. (2001). “A Novel Method for the Synthesis of ZnS for Use in the Preparation of Phosphors for CRT Devices.” *J. Electrochem. Soc.*, 148(10), H143.

Diamond, A. M., Corbellini, L., Balasubramaniam, K. R., Chen, S., Wang, S., Matthews, T. S., Wang, L.-W., Ramesh, R., and Ager, J. W. (2012). “Copper-alloyed ZnS as a p-type transparent conducting material.” *Phys. status solidi*, 209(11), 2101–2107.

- Enríquez, J. (2003). "Influence of the thickness on structural, optical and electrical properties of chemical bath deposited CdS thin films." *Sol. Energy Mater. Sol. Cells*, 76(3), 313–322.
- Farid, H., Abdel Rafea, M., El-Wahidy, E. F., and El-Shazly, O. (2014). "Preparation and characterization of ZnS nanocrystalline thin films by low cost dip technique." *J. Mater. Sci. Mater. Electron.*, 25(5), 2017–2023.
- Gaewdang, N., and Gaewdang, T. (2005). "Investigations on chemically deposited Cd_{1-x}Zn_xS thin films with low Zn content." *Mater. Lett.*, 59(28), 3577–3584.
- Garcia-Angelmo, A. R., Romano-Trujillo, R., Campos-Álvarez, J., Gomez-Daza, O., Nair, M. T. S., and Nair, P. K. (2015). "Thin film solar cell of SnS absorber with cubic crystalline structure." *Phys. Status Solidi Appl. Mater. Sci.*, 212(10), 2332–2340.
- Gedi, S., Minna Reddy, V. R., Pejjai, B., Jeon, C. W., Park, C., and Kt, R. R. (2016). "A facile inexpensive route for SnS thin film solar cells with SnS 2 buffer." *Appl. Surf. Sci.*, 372, 116–124.
- Gedi, S., Minnam Reddy, V. R., Park, C., Chan-Wook, J., and Ramakrishna, R. R. (2015). "Comprehensive optical studies on SnS layers synthesized by chemical bath deposition." *Opt. Mater. (Amst.)*, 42, 468–475.
- Gunasekaran, M., and Ichimura, M. (2007). "Photovoltaic cells based on pulsed electrochemically deposited SnS and photochemically deposited CdS and Cd_{1-x}Zn_xS." *Sol. Energy Mater. Sol. Cells*, 91(9), 774–778.
- Hariskos, D., Powalla, M., Chevaldonnet, N., Lincot, D., Schindler, A., and Dimmler, B. (2001). "Chemical bath deposition of CdS buffer layer: Prospects of increasing materials yield and reducing waste." *Thin Solid Films*, 387(1–2), 179–181.
- Hennayaka, H. M. M. N., and Lee, H. S. (2013). "Structural and optical properties of ZnS thin film grown by pulsed electrodeposition." *Thin Solid Films*, 548, 86–90.
- Hu, X., Zhang, X., Liang, L., Bao, J., Li, S., Yang, W., and Xie, Y. (2014). "High-Performance Flexible Broadband Photodetector Based on Organolead Halide Perovskite." *Adv. Funct. Mater.*, 24(46), 7373–7380.
- Huang, C. M., Chen, L. C., Pan, G. T., Yang, T. C. K., Chang, W. S., and Cheng, K. W. (2009). "Effect of Ni on the growth and photoelectrochemical properties of ZnS thin films." *Mater. Chem. Phys.*, 117(1), 156–162.

- Ichimura, M., and Maeda, Y. (2015). "Solid-State Electronics Heterojunctions based on photochemically deposited $\text{Cu}_x\text{Zn}_y\text{S}$ and electrochemically deposited ZnO ." *Solid State Electron.*, 107, 8–10.
- Iida, S., Yatabe, T., Kinto, H., and Shinohara, M. (1990). "Growth and characterization of p-type VPE ZnS layers." *J. Cryst. Growth*, 101(1–4), 141–146.
- Islam, M. M., Ishizuka, S., Yamada, A., Sakurai, K., Niki, S., Sakurai, T., and Akimoto, K. (2009). "CIGS solar cell with MBE-grown ZnS buffer layer." *Sol. Energy Mater. Sol. Cells*, 93(6–7), 970–972.
- Iwashita, T., and Ando, S. (2012). "Preparation and characterization of ZnS thin films by the chemical bath deposition method." *Thin Solid Films*, 520(24), 7076–7082.
- Jaber, A. Y., Alamri, S. N., Aida, M. S., Benghanem, M., and Abdelaziz, A. A. (2012). "Influence of substrate temperature on thermally evaporated CdS thin films properties." *J. Alloys Compd.*, 529, 63–68.
- Jia-ming Liu. (2005). *Photonic Devices*. UK: Cambridge University Press.
- Jiang, F., Shen, H., and Jiao, J. (2014). "Effect of the thickness on the optoelectronic properties of SnS films and photovoltaic performance of SnS/i-a-Si/n-a-Si solar cells." *Appl. Phys. A*, 117(4), 2167–2173.
- Jie, J. S., Zhang, W. J., Jiang, Y., Meng, X. M., Li, Y. Q., and Lee, S. T. (2006). "Photoconductive Characteristics of Single-Crystal CdS Nanoribbons." *Nano Lett.*, 6(9), 1887–1892.
- Kaneko, H., Minegishi, T., Nakabayashi, M., Shibata, N., Kuang, Y., Yamada, T., and Domen, K. (2016). "A Novel Photocathode Material for Sunlight-Driven Overall Water Splitting: Solid Solution of ZnSe and $\text{Cu}(\text{In,Ga})\text{Se}_2$." *Adv. Funct. Mater.*, 26(25), 4570–4577.
- Karunagaran, B., Uthirakumar, P., Chung, S. J., Velumani, S., and Suh, E.-K. (2007). "TiO₂ thin film gas sensor for monitoring ammonia." *Mater. Charact.*, 58(8–9), 680–684.
- Kawano, Y., Chantana, J., and Minemoto, T. (2015). "Impact of growth temperature on the properties of SnS film prepared by thermal evaporation and its photovoltaic performance." *Curr. Appl. Phys.*, 15(8), 897–901.
- Kawazoe, H., Yasukawa, M., Hyodo, H., Kurita, M., Yanagi, H., and Hosono, H. (1997). "P-type electrical conduction in transparent thin films of CuAlO_2 ." *Nature*,

389(6654), 939–942.

Kazmerski, L. L., White, F. R., and Morgan, G. K. (1976). “Thin-film CuInSe₂/CdS heterojunction solar cells.” *Appl. Phys. Lett.*, 29(4), 268–270.

Kedawat, G., Srivastava, S., Sharma, S., Vijay, Y. K., Predeep, P., Thakur, M., and Varma, M. K. R. (2011). “Structural and Optical Properties of RF—Sputtered ZnS Thin Films.” *AIP Conf. Proc.*, 83–85.

Kim, H., Han, J. Y., Kang, D. S., Kim, S. W., Jang, D. S., Suh, M., Kirakosyan, A., and Jeon, D. Y. (2011). “Characteristics of CuInS₂/ZnS quantum dots and its application on LED.” *J. Cryst. Growth*, 326(1), 90–93.

Kim, J., Park, C., Pawar, S. M., Inamdar, A. I., Jo, Y., Han, J., Hong, J., Park, Y. S., Kim, D. Y., Jung, W., Kim, H., and Im, H. (2014). “Optimization of sputtered ZnS buffer for Cu₂ZnSnS₄ thin film solar cells.” *Thin Solid Films*, 566, 88–92.

Koteeswara Reddy, N., Devika, M., and Gopal, E. S. R. (2015). “Review on Tin (II) Sulfide (SnS) Material: Synthesis, Properties, and Applications.” *Crit. Rev. Solid State Mater. Sci.*, 40(6), 359–398.

Kruse, P. W. (1995). “A comparison of the limits to the performance of thermal and photon detector imaging arrays.” *Infrared Phys. Technol.*, 36(5), 869–882.

Kumar, T. P., Saravanakumar, S., and Sankaranarayanan, K. (2011). “Effect of annealing on the surface and band gap alignment of CdZnS thin films.” *Appl. Surf. Sci.*, 257(6), 1923–1927.

Kumar, V., Sharma, D. K., Agrawal, S., Sharma, K. K., Dwivedi, D. K., and Bansal, M. K. (2016). “Tailoring of optical band gap by varying Zn content in Cd_{1-x}Zn_xS thin films prepared by spray pyrolysis method.” *AIP Conf. Proc.*, 020624.

Kunioka, A., and Sakai, Y. (1965). “Optical and electrical properties of selenium-cadmium sulfide photovoltaic cells.” *Solid State Electron.*, 8, 961–965.

Lander, J. J. (1960). “Reactions of Lithium as a donor and an acceptor in ZnO.” *J. Phys. Chem. Solids*, 15(3–4), 324–334.

Larson, C., Peele, B., Li, S., Robinson, S., Totaro, M., Beccai, L., Mazzolai, B., and Shepherd, R. (2016). “Highly stretchable electroluminescent skin for optical signaling and tactile sensing.” *Science* (80-.), 351(6277), 1071–1074.

Lee, J. H., Song, W. C., Yi, J. S., Yang, K. J., Han, W. D., and Hwang, J. (2003a). “Growth and properties of the Cd_{1-x}Zn_xS thin films for solar cell applications.” *Thin*

Solid Films, 431–432(03), 349–353.

Lee, J. H., Song, W. C., Yi, J. S., and Yoo, Y. S. (2003b). “Characteristics of the CdZnS thin film doped by thermal diffusion of vacuum evaporated indium films.” *Sol. Energy Mater. Sol. Cells*, 75(1–2), 227–234.

Li, M., Jiang, J., and Guo, L. (2010). “Synthesis, characterization, and photoelectrochemical study of Cd_{1-x}Zn_xS solid solution thin films deposited by spray pyrolysis for water splitting.” *Int. J. Hydrogen Energy*, 35(13), 7036–7042.

Liu, F., Lai, Y., Liu, J., Wang, B., Kuang, S., Zhang, Z., Li, J., and Liu, Y. (2010). “Characterization of chemical bath deposited CdS thin films at different deposition temperature.” *J. Alloys Compd.*, 493(1–2), 305–308.

Loferski, J. J. (1956). “Theoretical Considerations Governing the Choice of the Optimum Semiconductor for Photovoltaic Solar Energy Conversion.” *J. Appl. Phys.*, 27(7), 777–784.

Look, D. C., Reynolds, D. C., Litton, C. W., Jones, R. L., Eason, D. B., and Cantwell, G. (2002). “Characterization of homoepitaxial p-type ZnO grown by molecular beam epitaxy.” *Appl. Phys. Lett.*, 81(10), 1830–1832.

Lu, Z., Jin, R., Liu, Y., Guo, L., Liu, X., Liu, J., Cheng, K., and Du, Z. (2017). “Optimization of chemical bath deposited cadmium sulfide buffer layer for high-efficient CIGS thin film solar cells.” *Mater. Lett.*, 204, 53–56.

Mahdi, M. A., and Al-Ani, S. K. J. (2012). “Optical characterization of chemical bath deposition Cd_{1-x}Zn_xS thin films.” *Int. J. Nanoelectron. Mater.*, 5, 11–24.

Mahdi, M. S., Ibrahim, K., Hmood, A., Ahmed, N. M., Azzez, S. A., and Mustafa, F. I. (2016). “A highly sensitive flexible SnS thin film photodetector in the ultraviolet to near infrared prepared by chemical bath deposition.” *RSC Adv.*, 6(116), 114980–114988.

Mahmood, W., and Shah, N. A. (2014). “CdZnS thin films sublimated by closed space using mechanical mixing: A new approach.” *Opt. Mater. (Amst.)*, 36(8), 1449–1453.

Major, J. D., Treharne, R. E., Phillips, L. J., and Durose, K. (2014). “A low-cost non-toxic post-growth activation step for CdTe solar cells.” *Nature*, 511(7509), 334–337.

Minegishi, K., Koiwai, Y., Kikuchi, Y., Yano, K., Kasuga, M., and Shimizu, A. (1997). “Growth of p-type Zinc Oxide Films by Chemical Vapor Deposition.” *Jpn. J.*

Appl. Phys., 36(Part 2, No. 11A), L1453–L1455.

Ming, Z. X., Ding, C., Li, B., Zhang, J. Q., Li, W., Wu, L. L., Feng, L. H., and Wu, J. D. (2013). “Properties Study of ZnS Thin Films Fabricated at Different Substrate Temperatures by Pulsed Laser Deposition.” *Adv. Mater. Res.*, 821–822, 835–840.

Minnam Reddy, V. R., Gedi, S., Park, C., R.w, M., and Ramakrishna, R. R. (2015). “Development of sulphurized SnS thin film solar cells.” *Curr. Appl. Phys.*, 15(5), 588–598.

Moon, B. S., Lee, J. H., and Jung, H. (2006). “Comparative studies of the properties of CdS films deposited on different substrates by R.F. sputtering.” *Thin Solid Films*, 511–512, 299–303.

Nair, P. K., Garcia-Angelmo, A. R., and Nair, M. T. S. (2016). “Cubic and orthorhombic SnS thin-film absorbers for tin sulfide solar cells.” *Phys. Status Solidi Appl. Mater. Sci.*, 213(1), 170–177.

Nakada, T., and Mizutani, M. (2002). “18% efficiency Cd-free Cu(In, Ga)Se₂ thin-film solar cells fabricated using chemical bath deposition (CBD)-ZnS buffer layers.” *Japanese J. Appl. Physics, Part 2 Lett.*, 41(2 B), 7–10.

Nakada, T., Mizutani, M., Hagiwara, Y., and Kunioka, A. (2001). “High-efficiency Cu(In,Ga)Se₂ thin-film solar cells with a CBD-ZnS buffer layer.” *Sol. Energy Mater. Sol. Cells*, 67(1–4), 255–260.

Nazzal, A. Y., Qu, L., Peng, X., and Xiao, M. (2003). “Photoactivated CdSe Nanocrystals as Nanosensors for Gases.” *Nano Lett.*, 3(6), 819–822.

Niki, S., Contreras, M., Repins, I., Powalla, M., Kushiya, K., Ishizuka, S., and Matsubara, K. (2010). “CIGS absorbers and processes.” *Prog. Photovoltaics Res. Appl.*, 18(6), 453–466.

Noguchi, H., Setiyadi, A., Tanamura, H., Nagatomo, T., and Omoto, O. (1994). “Characterization of vacuum-evaporated tin sulfide film for solar cell materials.” *Sol. Energy Mater. Sol. Cells*, 35(C), 325–331.

Ortíz-Ramos, D. E., González, L. A., and Ramirez-Bon, R. (2014). “p-Type transparent Cu doped ZnS thin films by the chemical bath deposition method.” *Mater. Lett.*, 124, 267–270.

Park, R. M., Troffer, M. B., Rouleau, C. M., DePuydt, J. M., and Haase, M. A. (1990). “p-type ZnSe by nitrogen atom beam doping during molecular beam epitaxial

growth.” *Appl. Phys. Lett.*, 57(20), 2127–2129.

Patidar, D., Saxena, N. S., and Sharma, T. P. (2008). “Structural, optical and electrical properties of CdZnS thin films.” *J. Mod. Opt.*, 55(1), 79–88.

Popescu, V. (1999). “Optical properties of cadmium sulfide thin films, chemically deposited from baths containing surfactants.” *Thin Solid Films*, 349(1–2), 67–70.

Qiu, K., Qiu, D., Cai, L., Li, S., Wu, W., Liang, Z., and Shen, H. (2017). “Preparation of ZnS thin films and ZnS/p-Si heterojunction solar cells.” *Mater. Lett.*, 198, 23–26.

Rajathi, S., Sankarasubramanian, N., Ramanathan, K., and Senthamizhselvi, M. (2012). “Structural and optoelectronic properties of pyrolytically sprayed CdZnS thin films.” *Chalcogenide Lett.*, 9(12), 495–500.

Ramakrishna Reddy, K. T., Koteswara Reddy, N., and Miles, R. W. (2006). “Photovoltaic properties of SnS based solar cells.” *Sol. Energy Mater. Sol. Cells*, 90(18–19), 3041–3046.

Ramanathan, K., Contreras, M. A., Perkins, C. L., Asher, S., Hasoon, F. S., Keane, J., Young, D., Romero, M., Metzger, W., Noufi, R., Ward, J., and Duda, A. (2003). “Properties of 19.2% efficiency ZnO/CdS/CuInGaSe₂ thin-film solar cells.” *Prog. Photovoltaics Res. Appl.*, 11(4), 225–230.

Ramanathan, K., Teeter, G., Keane, J. C., and Noufi, R. (2005). “Properties of high-efficiency CuInGaSe₂ thin film solar cells.” *Thin Solid Films*, 480–481, 499–502.

Ramanujam, J., and Singh, U. P. (2017). “Copper indium gallium selenide based solar cells – a review.” *Energy Environ. Sci.*, 10(6), 1306–1319.

Raviprakash, Y., Bangera, K. V., and Shivakumar, G. K. (2011). “Investigations on electrical properties of the Cd_xZn_{1-x}S thin films prepared by spray pyrolysis technique.” *AIP Conf. Proc.*, 959–960.

Razeghi, M., and Rogalski, A. (1996). “Semiconductor ultraviolet detectors.” *J. Appl. Phys.*, 79(10), 7433–7473.

Robles, V., Trigo, J. F., Guillén, C., and Herrero, J. (2015a). “SnS absorber thin films by co-evaporation: Optimization of the growth rate and influence of the annealing.” *Thin Solid Films*, 582, 249–252.

Robles, V., Trigo, J. F., Guillén, C., and Herrero, J. (2015b). “Growth of SnS thin films by co-evaporation and sulfurization for use as absorber layers in solar cells.” *Mater. Chem. Phys.*, 167, 165–170.

- Romeo, N., Bosio, A., Canevari, V., and Podestà, A. (2004). "Recent progress on CdTe/CdS thin film solar cells." *Sol. Energy*, 77(6), 795–801.
- Romeo, N., Bosio, A., Tedeschi, R., Romeo, A., and Canevari, V. (1999). "A highly efficient and stable CdTe / CdS thin film solar cell." *Sol. Energy Mater.*, 58, 209–218.
- Sahay, P. P., Nath, R. K., and Tewari, S. (2007). "Optical properties of thermally evaporated CdS thin films." *Cryst. Res. Technol.*, 42(3), 275–280.
- Sall, T., Soucase, B. M., Mollar, M., and Sans, J. A. (2017). "SnS Thin Films Prepared by Chemical Spray Pyrolysis at Different Substrate Temperatures for Photovoltaic Applications." *J. Electron. Mater.*, 46(3), 1714–1719.
- Sánchez-Juárez, A., Tiburcio-Silver, A., and Ortiz, A. (2005). "Fabrication of SnS₂/SnS heterojunction thin film diodes by plasma-enhanced chemical vapor deposition." *Thin Solid Films*, 480–481, 452–456.
- Saritha, A. C., Shijeesh, M. R., Vikas, L. S., Prabhu, R. R., and Jayaraj, M. K. (2016). "Growth and characterization of p-ZnO:Cu thin film and its homojunction application." *J. Phys. D. Appl. Phys.*, 49(29), 295105.
- Sasikala, G., Thilakan, P., and Subramanian, C. (2000). "Modification in the chemical bath deposition apparatus, growth and characterization of CdS semiconducting thin films for photovoltaic applications." *Sol. Energy Mater. Sol. Cells*, 62(3), 275–293.
- Shannon, R. D. (1976). "Revised effective ionic radii and systematic studies of interatomic distances in halides and chalcogenides." *Acta Crystallogr. Sect. A*, 32(5), 751–767.
- Sharon, M., and Basavaswaran, K. (1988). "Photoelectrochemical behaviour of tin monosulphide." *Sol. Cells*, 25(2), 97–107.
- Sinsermsuksakul, P., Hartman, K., Bok Kim, S., Heo, J., Sun, L., Hejin Park, H., Chakraborty, R., Buonassisi, T., and Gordon, R. G. (2013). "Enhancing the efficiency of SnS solar cells via band-offset engineering with a zinc oxysulfide buffer layer." *Appl. Phys. Lett.*, 102(5), 053901.
- Sinsermsuksakul, P., Sun, L., Lee, S. W., Park, H. H., Kim, S. B., Yang, C., and Gordon, R. G. (2014). "Overcoming Efficiency Limitations of SnS-Based Solar Cells." *Adv. Energy Mater.*, 4(15), 1–7.
- Sns, C., Sn, S., Burton, L. A., Colombara, D., Abellon, R. D., Grozema, F. C., Peter, L. M., Savenije, T. J., Dennler, G., and Walsh, A. (2013). "Synthesis,

Characterization, and Electronic Structure of Single-Crystal SnS, Sn₂S₃, and SnS₂.” *Chem. Mater.*, 24(25), 4908–4916.

Späth, B., Fritsche, J., Säuberlich, F., Klein, A., and Jaegermann, W. (2005). “Studies of sputtered ZnTe films as interlayer for the CdTe thin film solar cell.” *Thin Solid Films*, 480–481, 204–207.

Sutrave, D. S., Shahane, G. S., Patil, V. B., and Deshmukh, L. P. (2000). “Micro-crystallographic and optical studies on Cd_{1-x}Zn_xSe thin films.” *Mater. Chem. Phys.*, 65(3), 298–305.

Takokoro, T., Ohta, S., Ishiguro, T., Ichinose, Y., Kobayashi, S., and Yamamoto, N. (1993). “Growth and characterization of CdS epilayers on (100) GaAs by atomic layer epitaxy.” *J. Cryst. Growth*, 130, 29–36.

Tao, Y., Wu, X., Wang, W., and Wang, J. (2015). “Flexible photodetector from ultraviolet to near infrared based on a SnS₂ nanosheet microsphere film.” *J. Mater. Chem. C*, 3(6), 1347–1353.

Tauc, J., and Menth, A. (1972). “States in the gap.” *J. Non. Cryst. Solids*, 8–10(C), 569–585.

Tomakin, M., Altunbaş, M., Bacakşz, E., and Polat, I. (2011). “Preparation and characterization of new window material CdS thin films at low substrate temperature (<300 K) with vacuum deposition.” *Mater. Sci. Semicond. Process.*, 14(2), 120–127.

Wangperawong, A., Hsu, P. C., Yee, Y., Herron, S. M., Clemens, B. M., Cui, Y., and Bent, S. F. (2014). “Bifacial solar cell with SnS absorber by vapor transport deposition.” *Appl. Phys. Lett.*, 105(17), 173904.

Wei, R., Tang, X., Hu, L., Hui, Z., Yang, J., Luo, H., Luo, X., Dai, J., Song, W., Yang, Z., Zhu, X., and Sun, Y. (2014). “Transparent conducting p-type thin films of c-axis self-oriented Bi₂Sr₂Co₂O_y with high figure of merit.” *Chem. Commun.*, 50(68), 9697–9699.

Woods-Robinson, R., Cooper, J. K., Xu, X., Schelhas, L. T., Pool, V. L., Faghaninia, A., Lo, C. S., Toney, M. F., Sharp, I. D., and Ager, J. W. (2016). “P-Type Transparent Cu-Alloyed ZnS Deposited at Room Temperature.” *Adv. Electron. Mater.*, 2(6), 1–9.

Wu, X. (2004). “High-efficiency polycrystalline CdTe thin-film solar cells.” *Sol. Energy*, 77(6), 803–814.

Wu, X., Dhere, R. G., Albin, D. S., Gessert, T. a, Dehart, C., Keane, J. C., Duda, a,

Coutts, T. J., Asher, S., Levi, D. H., Moutinho, H. R., Yan, Y., Moriarty, T., Johnston, S., Emery, K., and Sheldon, P. (2001). "High-Efficiency CTO / ZTO / CdS / CdTe Polycrystalline Thin-Film Solar Cells." *NCPV Progr. Rev. Meet.*, (October).

Xu, X., Bullock, J., Schelhas, L. T., Stutz, E. Z., Fonseca, J. J., Hettick, M., Pool, V. L., Tai, K. F., Toney, M. F., Fang, X., Javey, A., Wong, L. H., and Ager, J. W. (2016). "Chemical Bath Deposition of p-Type Transparent, Highly Conducting $(\text{CuS})_x:(\text{ZnS})_{1-x}$ Nanocomposite Thin Films and Fabrication of Si Heterojunction Solar Cells." *Nano Lett.*, 16(3), 1925–1932.

Yadav, A. A., and Masumdar, E. U. (2011). "Photoelectrochemical investigations of cadmium sulphide (CdS) thin film electrodes prepared by spray pyrolysis." *J. Alloys Compd.*, 509(17), 5394–5399.

Yin, L., Cheng, G., Feng, Y., Li, Z., Yang, C., and Xiao, X. (2015). "Limitation factors for the performance of kesterite $\text{Cu}_2\text{ZnSnS}_4$ thin film solar cells studied by defect characterization." *RSC Adv.*, 5(50), 40369–40374.

YS, T., and Perez-Alburne, E. (1982). "Efficient thin-film CdS/CdTe solar cells." *Conf. Rec. IEEE Photovolt. Spec. Conf.; (United States); Conf. 16. IEEE photovoltaics Spec. Conf. San Diego, CA, USA.*

Zeng, L. H., Wang, M. Z., Hu, H., Nie, B., Yu, Y. Q., Wu, C. Y., Wang, L., Hu, J. G., Xie, C., Liang, F. X., and Luo, L. B. (2013a). "Monolayer graphene/germanium schottky junction as high-performance self-driven infrared light photodetector." *ACS Appl. Mater. Interfaces*, 5(19), 9362–9366.

Zeng, X., Pramana, S. S., Batabyal, S. K., Mhaisalkar, S. G., Chen, X., and Jinesh, K. B. (2013b). "Low temperature synthesis of wurtzite zinc sulfide (ZnS) thin films by chemical spray pyrolysis." *Phys. Chem. Chem. Phys.*, 15(18), 6763.

Zhao, L., Di, Y., Yan, C., Liu, F., Cheng, Z., Jiang, L., Hao, X., Lai, Y., and Li, J. (2016). "In situ growth of SnS absorbing layer by reactive sputtering for thin film solar cells." *RSC Adv.*, 6(5), 4108–4115.

Zhou, J., Wu, X., Teeter, G., To, B., Yan, Y., Dhere, R. G., and Gessert, T. A. (2004). "CBD- $\text{Cd}_{1-x}\text{Zn}_x\text{S}$ thin films and their application in CdTe solar cells." *Phys. Status Solidi Basic Res.*, 241(3), 775–778.

List of Publications

1. Biswajit Barman, Kasturi V. Bangera, G.K. Shivakumar (2019), "Preparation of thermally deposited $\text{Cu}_x(\text{ZnS})_{1-x}$ thin films for opto-electronic devices." *J. Alloys Compd.* 772 (532-536). doi:10.1016/j.jallcom.2018.09.192.
2. Biswajit Barman, Kasturi V. Bangera, G.K. Shivakumar (2019), "Effect of substrate temperature on the suitability of thermally deposited cadmium sulfide thin films as window layer in photovoltaic cells." *Superlattices and Microstructures* 123 (374-381). doi: 10.1016/j.spmi.2018.09.030.
3. Biswajit Barman, Kasturi V. Bangera, G.K. Shivakumar (2019), "Evaluation of semiconducting p-type tin sulfide thin films for photodetector applications." *Superlattices and Microstructures* 133 (106215). doi: 10.1016/j.spmi.2019.106215.
4. Biswajit Barman, Kasturi V. Bangera, G.K. Shivakumar (2019), " $\text{Zn}_x\text{Cd}_{1-x}\text{S}$ thin films: A study towards its application a reliable photodetector." *Superlattices and Microstructures* (2019) doi: <https://doi.org/10.1016/j.spmi.2019.106349>.
5. Biswajit Barman, Kasturi V. Bangera, G.K. Shivakumar (2019), "A comprehensive study on the structural, morphological, compositional and optical properties of $\text{Zn}_x\text{Cd}_{1-x}\text{S}$ thin films." *Materials Research Express* (under review).
6. Biswajit Barman, Kasturi V. Bangera, G.K. Shivakumar (2019), " $\text{Zn}_x\text{Sn}_{1-x}\text{S}$ thin films: A study on its tunable opto-electrical properties for application towards a high efficient photodetector." *Applied Materials & Interfaces* (under review).
7. Biswajit Barman, Darshan C., Kasturi V. Bangera, G.K. Shivakumar (2019), "Band gap engineering of thermally deposited $\text{ZnS}_x\text{Se}_{1-x}$ thin films." *Physica B: Condensed Matter* (under review).

BISWAJIT BARMAN

PH110, 1st Floor, Physics Department,

National Institute of Technology Karnataka, Surathkal – 575025.

E-mail: biswajitbrmn016@gmail.com, Phone: +91 – 8147609830

A dedicated and capable research fellow with 4.5 years of experience in graduate level research. Published extensively in scientific journals, with expertise in the growth and analysis of thin films. A confident presenter with the ability to convey complex information to audiences of all levels.

RESEARCH EXPERIENCE

Ph.D. Student, National Institute of Technology Karnataka, 2016 – 2019

- Design, assembly, and maintenance of experimental setups (Thermal Evaporation Unit).
- Characterize and analyze the structural, morphological, compositional, optical and electrical properties of metal sulfide thin films.
- Scientific dissemination through publications in peer-reviewed journals.

Intern Fellow, CPMU, Jawaharlal Nehru Centre for Advanced Scientific Research, 2015 – 2016

- Deposition and study of gold nanowire networks on silicon substrates using crackle lithography technique.
 - Study the electrical and morphological properties of the gold nanowire networks.
-

ACADEMIC PROFILE

Ph.D., Physics Department, National Institute of Technology Karnataka, (Thesis Submitted, 2019)

Dissertation Title: *Preparation and characterization of mixed metal sulfide thin films for photosensor applications.*

Dissertation Advisor: Prof. Kasturi V. Bangera, Physics Department, National Institute of Technology Karnataka, Surathkal.

M.Tech., Nanotechnology, The National Institute of Engineering, 2016

Thesis Title: *Silicon photodiode using gold network.*

Thesis Advisors: Prof. G.U. Kulkarni, Director, Centre for Nano and Soft Matter Sciences, Bengaluru.

Prof. L. Krishnamurthy, H.O.D., Mechanical Engineering Department, National Institute of Engineering, Mysuru.

B.Tech., Electronics & Communication Engg., Adichunchanagiri Institute of Technology, 2013

PUBLICATIONS

1. **B Barman**, KV Bangera, GK Shivakumar, "Effect of substrate temperature on the suitability of thermally deposited cadmium sulfide thin films as window layer in photovoltaic cell", *Superlattices and Microstructures* 123, 374-381. (Impact Factor = 2.385) doi: <https://doi.org/10.1016/j.spmi.2018.09.030>
2. **B Barman**, KV Bangera, GK Shivakumar, "Preparation of thermally deposited $\text{Cu}_x(\text{ZnS})_{1-x}$ thin films for opto-electronic devices", *Journal of Alloys and Compounds* 772, 532-536. (Impact Factor = 4.175) doi: <https://doi.org/10.1016/j.jallcom.2018.09.192>
3. **B Barman**, KV Bangera, GK Shivakumar, "Evaluation of semiconducting p-type tin sulfide thin films for photodetector applications", *Superlattices and Microstructures* 133, 106215. (Impact Factor = 2.385) doi: <https://doi.org/10.1016/j.spmi.2019.106215>
4. **B Barman**, KV Bangera, GK Shivakumar, " $\text{Zn}_x\text{Cd}_{1-x}\text{S}$ thin films: A study towards its application a reliable photodetector", *Superlattices and Microstructures* (2019), 106349. (Impact Factor = 2.385) doi: <https://doi.org/10.1016/j.spmi.2019.106349>
5. **B Barman**, KV Bangera, GK Shivakumar, "A comprehensive study on the structural, morphological, compositional and optical properties of $\text{Zn}_x\text{Cd}_{1-x}\text{S}$ thin films", *Materials Research Express*. (under review).
6. **B Barman**, Kasturi V. Bangera, G.K. Shivakumar (2019), " $\text{Zn}_x\text{Sn}_{1-x}\text{S}$ thin films: A study on its tunable opto-electrical properties for application towards a high efficient photodetector." *Applied Materials & Interfaces* (under review).
7. **B Barman**, Darshan C., Kasturi V. Bangera, G.K. Shivakumar (2019), "Band gap engineering of thermally deposited $\text{ZnS}_x\text{Se}_{1-x}$ thin films." *Physica B: Condensed Matter* (under review).

CONFERENCES

1. Presented a poster entitled "**Self-Powered Sensor**" at "Second Indo-Canadian Symposium on Nano-Science and Technology (ICSNST-2016), Mysuru" on February 18-19, 2016.
2. Oral presentation entitled "**Fabrication and growth of PbS quantum dots thin film photovoltaics**" at the International Conference on "Solar Asia-2015" at Savitribai Phule Pune University, Pune India on July 30, 2015 to August 1, 2015.

3. Presented a poster entitled “**Deposition of Nanostructured multilayered coatings of CZTS thin films by Vacuum Thermal Evaporation**” at International conference on “Recent Advances in Nano science and Technology (RAINSAT-2015)” at Sathyabama University” on July 8-9, 2015.

ACADEMIC ACTIVITIES/ACHIEVEMENTS

1. Selected for “**South – East Asian Network for Disaster and Environmental Engineering (SEAN-DEE), 2015**” Lab program at “**Universität Kassel, Germany**” which is sponsored by the German Academic Exchange Service (**DAAD**).
2. **Gold Medalist** in M.Tech Nanotechnology.
3. Selected for **Technical Education Quality Improvement Programme (TEQIP-II) Fellowship** at The National Institute of Engineering, Mysuru during 2014 – 2016.
4. Participated in two-day workshop on “Awareness on Plagiarism – 2016”.
5. Participated in “International Symposium on Microgrid – 2015”.
6. Participated in one-day workshop on “Additive Manufacturing Technology - 2015”.

SKILLS AND EXPERTISE

1. Thin film deposition techniques
 - a. Thermal evaporation (Model No. 12A4D, HVI Ltd. & Model Name: Smart Coat 3.0, HHV Ltd., India).
 - b. Spray Pyrolysis (Model No. HO-TH-04, Holmarc, India).
 - c. DC Sputtering (VEC Solutions, India).
 - d. Spin coating (Nova Technologies, USA).
2. Instrumentation
 - a. XRD Rigaku (MiniFlex – 600, Japan)
 - b. Solar Simulator (PEC-L01, Peccell Technologies Inc.).
 - c. Four-Point Probe Station (Techno Science Instruments).
 - d. UV-Visible Spectroscopy (SpectraPro 2300i, Princeton Instruments).
 - e. Keithley 2400 Sourcemeter, Keithley 2002 Multimeter, and Keysight B2985A Multimeter.
3. Arduino Programming.

RESEARCH INTERESTS

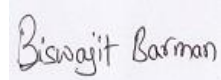
Thin Film Photovoltaics, thin film sensors, band gap engineering, transparent conductors, flexible electronics.

PERSONAL DETAILS

Name	Biswajit Barman
Date of Birth	31/03/1992 (dd/mm/yyyy)
Sex	Male
Nationality	Indian
Languages Known	English, Bengali, Hindi.
Permanent Address	#85, Babupara, Mahendraganj, South West Garo Hills, Meghalaya – 794106, India.

DECLARATION

I hereby declare that the above-furnished information is true to the best of my knowledge.



(BISWAJIT BARMAN)

Place: Surathkal

